Inclusive Nuclear Electromagnetic Response in the

Quasielastic Region at Large Momentum Transfer

Christopher Douglas Cothran
Miami, Florida

B.S., Stanford University, 1992

A Dissertation presented to the Graduate Faculty
of the University of Virginia in Candidacy for the Degree of
Doctor of Philosophy

Department of Physics

University of Virginia
August 2000

Abstract

Experiment E89-008, performed in Hall C at the Thomas Jefferson National Accelerator Facility (TJNAF), measured inclusive electron scattering cross sections from nuclear targets in the quasielastic region. This experiment was one of the first to make use of the Continuous Electron Beam Accelerator (CEBA) at TJNAF, which provided a 4.045 GeV beam of electrons at currents ranging from 10 to 80 μA. This work reports cross section measurements from the analysis of ^{12}C, ^{56}Fe, and ^{197}Au data collected with the High Momentum Spectrometer (HMS) operated at laboratory angles of 15, 23, 30, 37, 45, and 55 degrees. These measurements, which almost double the kinematic coverage of previous experiments, establish the scaling of the quasielastic function $F(y, |\mathbf{q}|)$ on the low energy loss wing of the quasielastic peak out to $y \approx -0.4$ GeV/c. The structure function F_2^A exhibits approximate scaling in the Nachtmann variable ξ. Scaling of F_2^A in the Bjorken variable x is observed when the quasielastic contribution, calculated within a reasonable model, is subtracted; comparison with parton recombination model predictions at $x > 1$ is inconclusive.

Acknowledgements

Modern nuclear or particle physics experiments require the dedication and cooperation of a large number of people, and this experiment is no exception. While I cannot list everyone, I would like to thank my advisors, Donal Day and Jim McCarthy, and the other graduate students and technical staff, particularly Paul Hood and Mark Hoegral, at TJNAF.

Likewise, no Physics department runs well without a hard working staff. I would like to thank Suzie Garrett and Pam Joseph for all of their support, as well as Mary Williams and Cora Booker for keeping things neat and tidy.

I am grateful for the love, encouragement, and patience which my parents, Riley and Marga, my sister, Jodi, the rest of my family, and my girlfriend Shannon Jenkins, have given me throughout this long graduate school experience. I am also thankful for the companionship of great friends (you know who you are) who stuck with me despite my bad moods and periods of self-imposed isolation, and helped remind me that there is more to life than work.

Contents

List of Figures

Chapter 1

Introduction

The atomic nucleus is a composite system of strongly interacting protons and neutrons. In the simplest picture, the interactions among these nucleons produce an average potential, leading to a shell model description of the nucleus. The nucleons are also composite systems, built within the framework of Quantum Chromodynamics (QCD) from three constituent quarks confined by a gluon gauge field and accompanied by a sea of virtual quark-antiquark pairs. To date, quarks are considered fundamental, so it is one of the most important goals of modern nuclear physics to understand how QCD influences nuclear structure, and to what extent the traditional models built from nucleon-nucleon potentials or the effective nucleon-meson field theories are adequate.

Scattering experiments are ideal for illuminating nuclear structure; consequently, they have been the staple experimental tool since early in the twentieth century. In

particular, inclusive electron scattering, in which only the scattered electron is detected, has been extremely fruitful. The electromagnetic interaction is weak enough to be uniformly sensitive to the entire nuclear volume, and couples to the nuclear charge and current densities. Specifically, it is a good approximation to say that the scattering event transfers energy ν and momentum $\mathbf{q}$ to the nucleus through the exchange of a single virtual photon, making the scattering amplitude proportional to the (space-time) Fourier transform of the nuclear electromagnetic current. One particularly useful and familiar consequence is that the momentum transfer is inversely related to the distance scale over which the interaction takes place, $R \approx 2\pi/|\mathbf{q}| \equiv \lambda$, where λ is the wavelength of the virtual photon.

The distance scale of the interaction differentiates aspects of nuclear structure. At very long range, many times the nuclear radius, the scattering cross section shows several sharp peaks in energy loss, the dominant one produced by elastic scattering from the total charge and magnetization of the nucleus and others at higher energy loss from transitions to discrete nuclear excited states. As λ decreases below the nuclear radius, the finite extent of the nucleus is evident as these peaks rapidly decrease in strength and exhibit diffraction minima. At larger values of energy loss, beyond the discrete excitations, most complex nuclei also exhibit strong resonant modes of many correlated nucleons.

All of these features continue to lose strength as λ decreases down to the size of a single nucleon, and a broad peak in energy loss, centered approximately at the

position for elastic scattering from a stationary nucleon, becomes the primary nuclear response. This is the quasielastic peak. It is mostly the result of incoherent elastic scattering from the individual nucleons which make up the nucleus. The internal motion of the nucleons, determined by the nuclear dynamics and characterized by the nuclear spectral function, is directly responsible for the shape of this peak.

The internal motion affects the response not only when the nucleons recoil elastically, but also when they are scattered into inelastic final states. Resonances of discrete nucleon excitations produce a few broadened peaks on the high energy loss side of the quasielastic peak. As λ decreases below the nucleon radius, a continuum of inelastic excitation extending to very large energy loss rises relative to both the quasielastic peak and resonances, and becomes dominant when λ is small enough to begin resolving quarks. This is known as deep inelastic scattering, and is characterized as incoherent elastic scattering from quarks within nucleons.

The layers of nuclear structure just described blend smoothly together as λ decreases from nuclear to nucleon to quark distance scales. Unfortunately, the theoretical understanding of these domains is largely disjoint. Traditional nuclear theory describes the nucleus as a collection of nucleons interacting through a two-body potential, and makes no reference to quarks. Nevertheless, nucleons are composed of quarks, so somehow QCD must ultimately define nuclear dynamics. Exactly how the transition from a quark to a nucleon description of the nucleus happens within the framework of QCD is entirely unknown. To bridge the gap, experimental results are

essential for guidance and progress.

This thesis describes the results of an experiment which measured inclusive electron scattering cross sections from nuclei in the quasielastic region at large momentum transfers, or short distances, where quasielastic scattering begins to be subsumed by the inelastic response and the distinction between the nucleon and quark description of the nucleus becomes blurred. On the low energy loss side of the quasielastic peak, the traditional nuclear physics description is applied. In this region, the cross sections are reduced to the quasielastic function $F(y, |\mathbf{q}|)$ which should be sensitive only to nuclear dynamics. Ideally, this quantity is determined by an integral over the nuclear spectral function and is expected to scale at large $|\mathbf{q}|$ as a function of the minimum initial nucleon longitudinal momentum y consistent with quasielastic reaction kinematics. The experimental values for $F(y, |\mathbf{q}|)$ are shown to scale out to $y \approx -0.4$ GeV/c. These results are further examined for the role of short range correlated nucleon pairs at low energy loss. On the high energy loss side of the quasielastic peak, the quark description of nuclear structure is more appropriate. The experimental cross sections are reduced to the structure function F_2^A; this structure function is known to scale, up to logarithmic violations, in the deep inelastic region as a function of the Bjorken variable x, which represents the fractional quark momentum. These results show that the inelastic contribution to F_2^A, obtained by subtracting a calculation of the quasielastic contribution, continues to scale beyond the top of the quasielastic peak at $x = 1$. No subtraction is necessary to observe the scaling of F_2^A in the Nachtmann

variable ξ, which represents the fractional quark lightcone momentum. All of these results are compared to a model calculation using the quasifree approximation and a model for the spectral function which includes the effects of correlated nucleon pairs.

Section 1.1 of this chapter contains a survey of the important experimental results that have contributed to the understanding of the aspects of nuclear structure described above. Much of this discussion is drawn from a number of reviews [1, 2, 3, 4, 5, 6, 7]. Section 1.2 concludes this chapter with a summary of the kinematic conditions specifying the experiment described in this work. Chapter 2 discusses electron scattering in greater detail, describes more precisely the relevant physics of nucleons and nuclei, and introduces the quasifree model. Chapters 3 and 4 highlight the details of the experiment and data reduction methods, and Chapter 5 presents the analysis of the results.

1.1   Survey

The first extensive study [8] of the inclusive quasielastic response for a wide range of nuclei was performed during the early 1970s at the High Energy Physics Laboratory (HEPL) at Stanford University using a 500 MeV electron beam, with scattered electrons detected at 60 degrees. Figure 1.1 indicates the results for ^{6}Li, ^{12}C, and ^{208}Pb. Several important observations resulted from this study. First, the peak height and width show a clear inverse relationship, so that the total strength of the quasielastic

peak is roughly proportional to the total number of nucleons in the nucleus, in agreement with the quasielastic hypothesis. Also, the width of the peak for heavy nuclei approaches a constant value, indicating the saturation of the nuclear density.

In addition, these data were famously fit to the results of the Fermi gas model calculation of Moniz [9]. The resulting values of Fermi momenta reached a limiting value of about 265 MeV for the heaviest nuclei, and the required shifts in the peak location were in rough agreement with the nucleon binding energies. Calculations based on traditional nonrelativistic nuclear models, after accounting for the final state interactions of the recoiling nucleon with the residual nuclear system, also reproduced the peak height and width, as did relativistic mean field calculations [10]. However, the contributions at large ν from additional processes clearly extending under the peak made this agreement somewhat questionable. Nevertheless, the general agreement between experiment and theory verified that incoherent scattering from individual nucleons within the nucleus was indeed the dominant reaction mechanism.

An experiment [11] at SLAC detecting electrons scattered at 8 degrees from ^{3}He with beam energies ranging from 3 to 15 GeV was the first to study the quasielastic region over a wide range of momentum transfer. Shortly thereafter, in 1980, it was shown [12] that when these results were divided by the sum of the cross sections for elastic scattering from individual nucleons moving with the minimum momentum y necessary to absorb the transfered energy ν and momentum $\mathbf{q}$, the data collapsed onto a single curve when plotted against y, as indicated in Figure 1.2. This observation
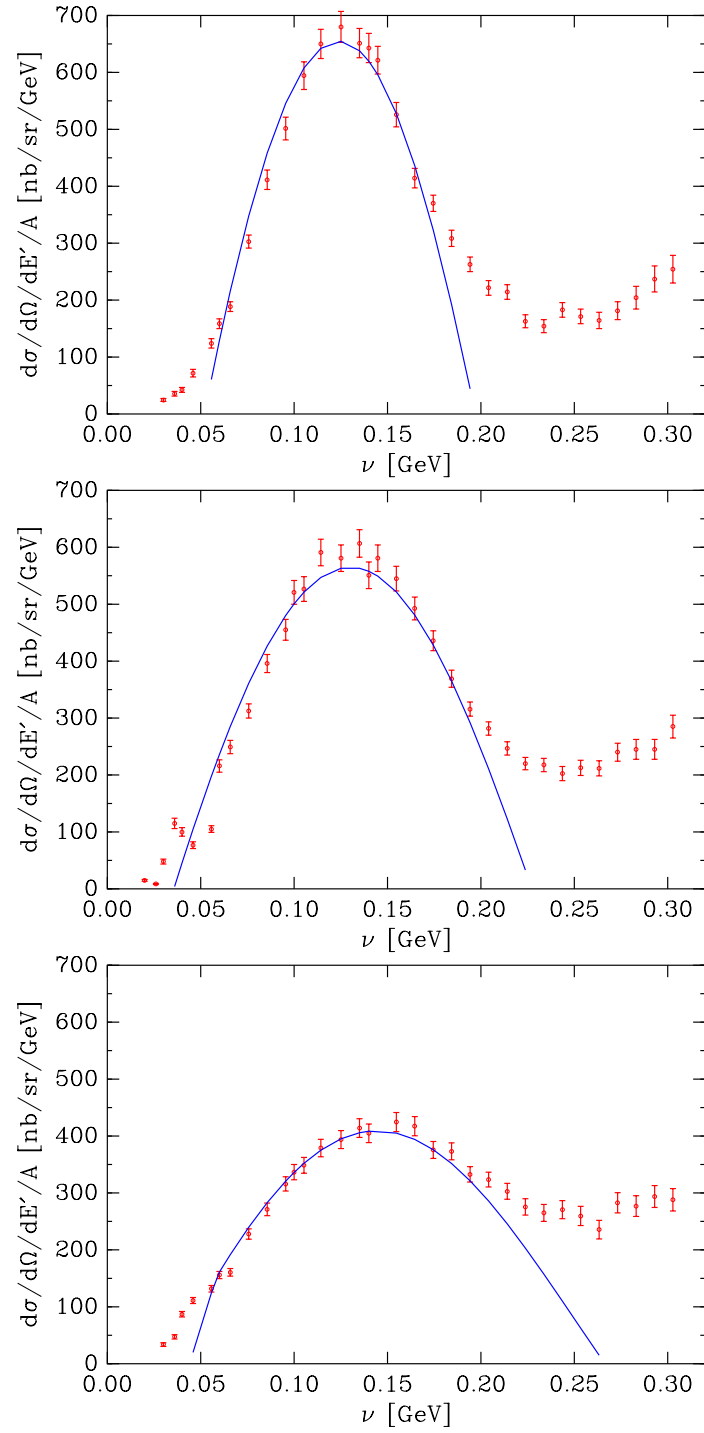
Figure 1.1: HEPL [8] cross sections per nucleon for ^{9}Li (top), ^{12}C (middle), and ^{208}Pb (bottom), and the results of the Fermi gas model fit.

of y-scaling not only validated the quasielastic reaction mechanism, but also showed that the cross section measurements could be stripped down to a quantity dependent solely upon nuclear dynamics, the quasielastic function $F(y, |\mathbf{q}|)$. Formal definitions of y and $F(y, |\mathbf{q}|)$ are given by equations (2.33) and (2.34) in Chapter 2.

Since then, y-scaling has been applied to measurements on a variety of nuclei, including but not restricted to ^{2}H [13, 14], ^{4}He [15], and the results of SLAC experiment NE3 [16] on ^{4}He, ^{12}C, ^{27}Al, ^{56}Fe, and ^{197}Au, yielding a number of interesting observations. At $y < 0$ quasielastic scattering should be dominant. Indeed, scaling holds to varying degrees in this region, far better than at $y > 0$ where the inelastic contributions are significant. The deuteron and ^{3}He scale very well; as nuclei get heavier, the quality of the scaling generally degrades. The scaling of ^{2}H can be understood as a consequence of the fact that all of the nucleon momentum distribution is contained in a single bound state at 2.2 MeV. For ^{3}He, a bound state at 5.5 MeV contains most of the distribution at low momentum, with the rest increasingly spread out over a continuum of nuclear excitation energies at higher momenta. In the simplest picture of quasielastic scattering, such a distribution in energy should cause $F(y, |\mathbf{q}|)$ to increase to a limiting value as $|\mathbf{q}|$ increases. However, the data for all nuclei show convergence from above; it is widely believed that final state interactions account for this behavior.

All nuclei show significant response at large negative values of y, much more than would be expected from the Fermi gas model or any traditional independent particle
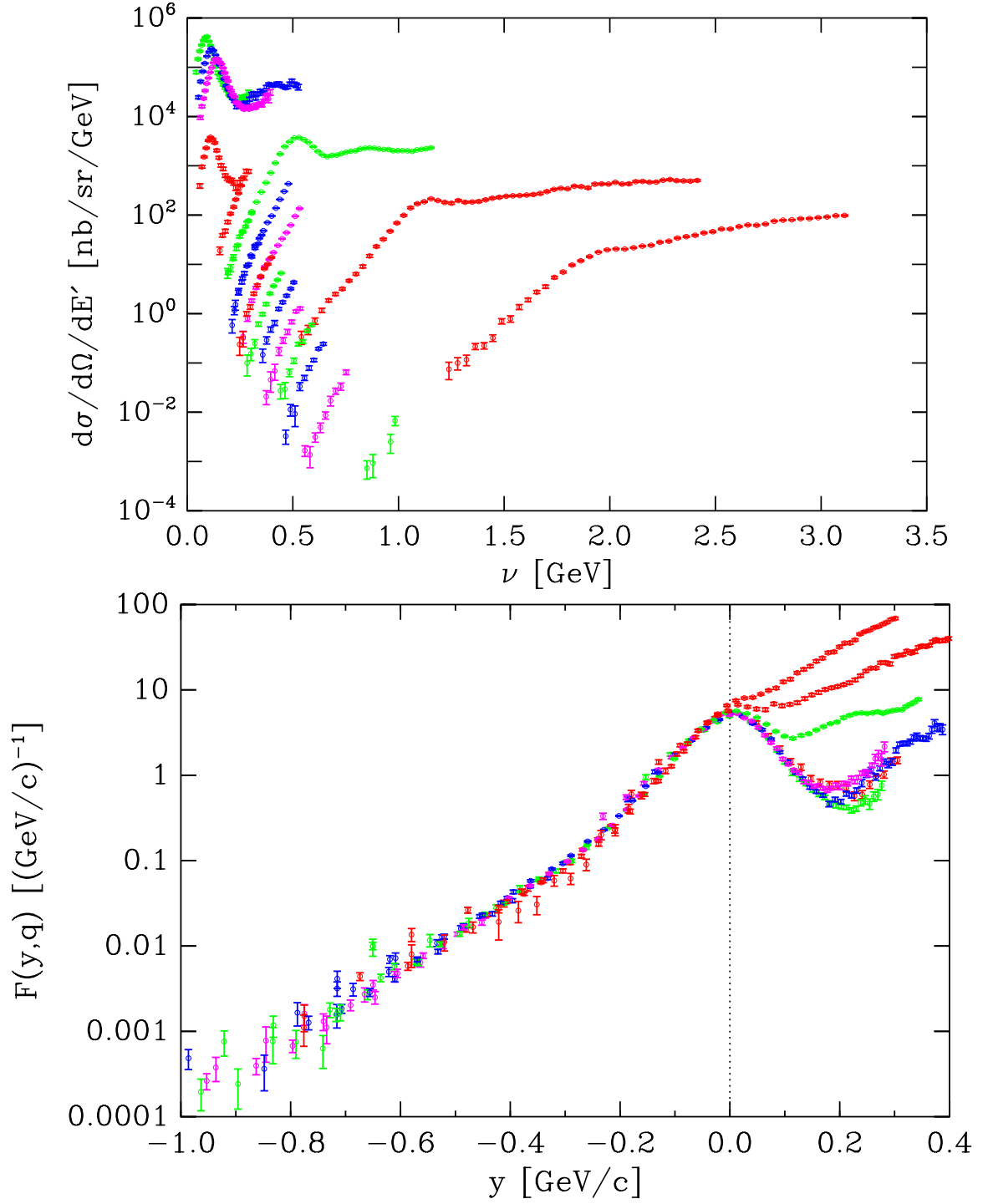
Figure 1.2: The ^{3}He inclusive cross sections (top) and the corresponding y-scaling function (bottom).

model of the nucleus. These high momentum components likely result from nucleon pairs interacting strongly at short distance. Exclusive measurements on ^{3}He [17] have shown that the strength in the excitation energy continuum does increase significantly relative to the content of the 5.5 MeV bound state, and dominates at high momentum. Moreover, the data suggest that the high momentum of the struck nucleon is balanced by just one of the remaining two nucleons in ^{3}He: the peak in the observed excitation energy continuum agrees well with the kinetic energy of a single nucleon carrying off the momentum balance. These observations qualitatively agree with the expectation that short range interaction of nucleon pairs is responsible for high momentum components in the nuclear wave function.

Scaling clearly does not hold at $y > 0$, indicating the presence of additional reaction mechanisms other than the quasielastic. At low $|\mathbf{q}|$ and in the "dip" region between the quasielastic peak and the first nucleon resonance, the likely contributions from meson exchange currents, isobar excitations, and multinucleon currents all contribute to the transverse nuclear current, and therefore to the nuclear response to transversely polarized virtual photons. A number of experiments [18, 19, 20, 21, 22] during the 1980s performed the separation of the nuclear response in the quasielastic region into longitudinal and transverse components. Although one of the most notable applications of these data has been to test the Coulomb sum rule, these results also verified the transverse nature of the additional reaction mechanisms.

The longitudinal and transverse scaling functions F_L and F_T for ^{12}C [19] at
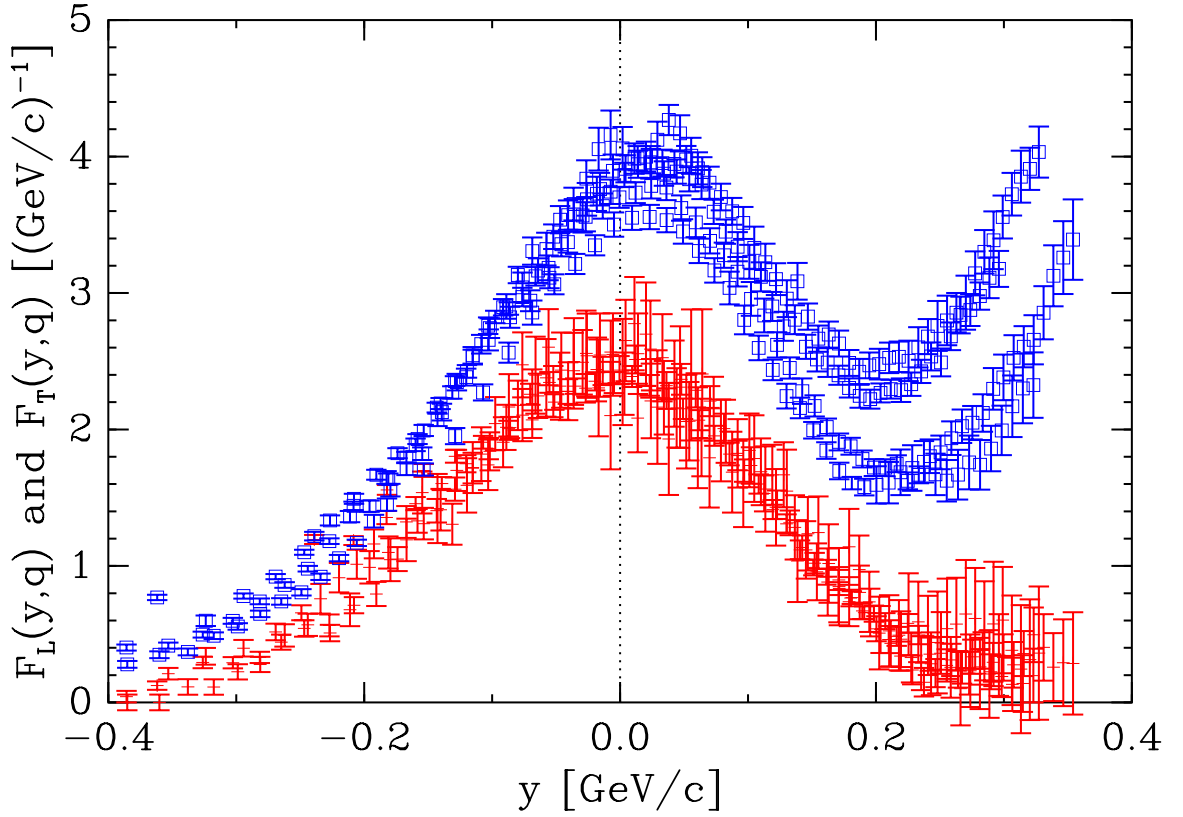
Figure 1.3: Longitudinal (red plusses) and transverse (blue squares) scaling functions for ^{12}C [19] at $|\mathbf{q}| = 350, 400, 500, 550, 600$ MeV/c.

$|\mathbf{q}| = 350, 400, 500, 550,$ and 600 MeV are shown in Figure 1.3. Although the range of $|\mathbf{q}|$ is small, scaling for F_L is good on *both* sides of the peak. It is clear that the additional reaction mechanisms are, as suspected, primarily transverse contributions to the nuclear current. Although they test a very small fraction of the inclusive response, exclusive measurements on ^{12}C [23, 24] near the top of the quasielastic peak have further identified these contributions as coming from a small but extremely broad continuum in excitation energy which sets in at the two nucleon emission threshold, and strongly suggest [3, 1] that for the bound states $F_L = F_T$, in agreement with the

quasielastic reaction mechanism.

At larger momentum transfers, y-scaling is broken so badly at $y > 0$ that it is no longer a useful tool. In this region, as previously discussed, the virtual photon begins to uncover the quark substructure of the nucleus. The results are more appropriately analyzed using the nuclear structure function F_2^A and the Bjorken variable x, which is loosely described as the fraction of the proton momentum carried by the struck quark; see section 2.2.2 for precise definitions and a thorough discussion. Whether the quark substructure in the nucleus is restricted to the individual nucleons or becomes somewhat delocalized is an open question. It is important therefore to first look at the structure of a free nucleon, then compare it against the structure seen within a nucleus.

Figure 1.4 is an example of both the resonance and deep inelastic contributions to the proton structure function F_2^p. These data show three peaks consisting of proton excited state resonances sitting in a large continuum beginning at the threshold for pion production; the elastic peak would appear at $x = 1$. The featureless part of the continuum beyond the resonances is the deep inelastic response; although not a precise boundary, this label is conventionally used to characterize all inelastic final states with invariant mass exceeding twice the proton mass. With increasing Q^2, the resonances are pushed toward $x = 1$, and the deep inelastic dominates the response.

In 1969, Bjorken [26] first predicted, then experiments at SLAC confirmed, that the deep inelastic contribution to F_2^p scales in x. This led Feynman [27] to suggest that
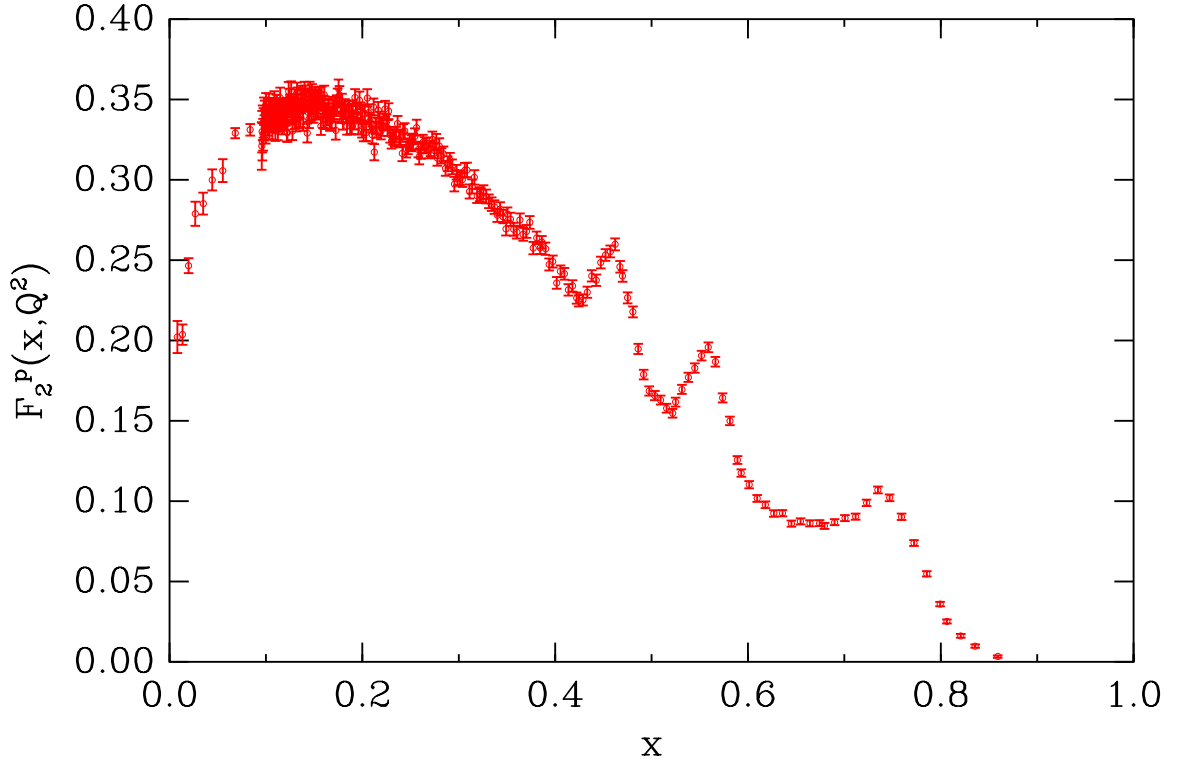
Figure 1.4: An example of the proton structure function F_2^p measured at SLAC [25] for 20 GeV incident electrons and a scattering angle of 4°.

this behavior could be explained if the nucleon contains noninteracting constituents, referred to as partons; electron scattering from the proton could then be thought of as incoherent elastic scattering from partons. The parton model was a precursor to QCD, the fully interacting theory of quarks and gluons. Within QCD, quarks interact so strongly at long range, distances comparable to the nucleon radius, that a single quark can never be isolated; this property is known as confinement. However, at very short range, the interaction becomes so weak that in first approximation they behave as if they were free; this property is known as asymptotic freedom. The influence of these two distinct behaviors is reflected in the resonance and deep inelastic responses

of the proton structure functions. The asymptotic freedom of QCD verifies the central assumption of the parton model, but rather than exact scaling of F_2^p, QCD predicts a mild, logarithmic scaling violation as quarks are resolved at smaller and smaller distances. The confirmation of this prediction over an enormous kinematic range, as indicated in Figure 1.5, represents one of the most significant successes of QCD.

It is well established that the deep inelastic response of nuclei differs from the deep inelastic response of free nucleons. The European Muon Collaboration [33] first observed this difference in 1981. When summarized in the form of the x dependence of the ratio of cross sections, this difference is known as the EMC effect. Although there are competitors, the most direct explanation for the EMC effect is that the internal nucleon structure is modified in a nucleus. One model, the Q^2 rescaling model [34], describes the bulk of the EMC effect as the result of an increase in the quark confinement scale for bound nucleons. This model suggests that at long range where QCD is strong, quarks in bound nucleons are partially deconfined as compared to those in free nucleons; when studied at short range, the quark momentum distributions are softer, with more momentum radiated into the glue and the quark-antiquark sea. Such a description is qualitatively consistent with the observed behavior of the deep inelastic nuclear response, and is in quantitative agreement with the EMC effect, as indicated in Figure 1.6 for ^{56}Fe. Within this intuitively appealing model, the modification of the short range nucleon structure clearly points back to the long range properties of QCD, perhaps providing a first glimpse at the role of QCD in nuclear dynamics.
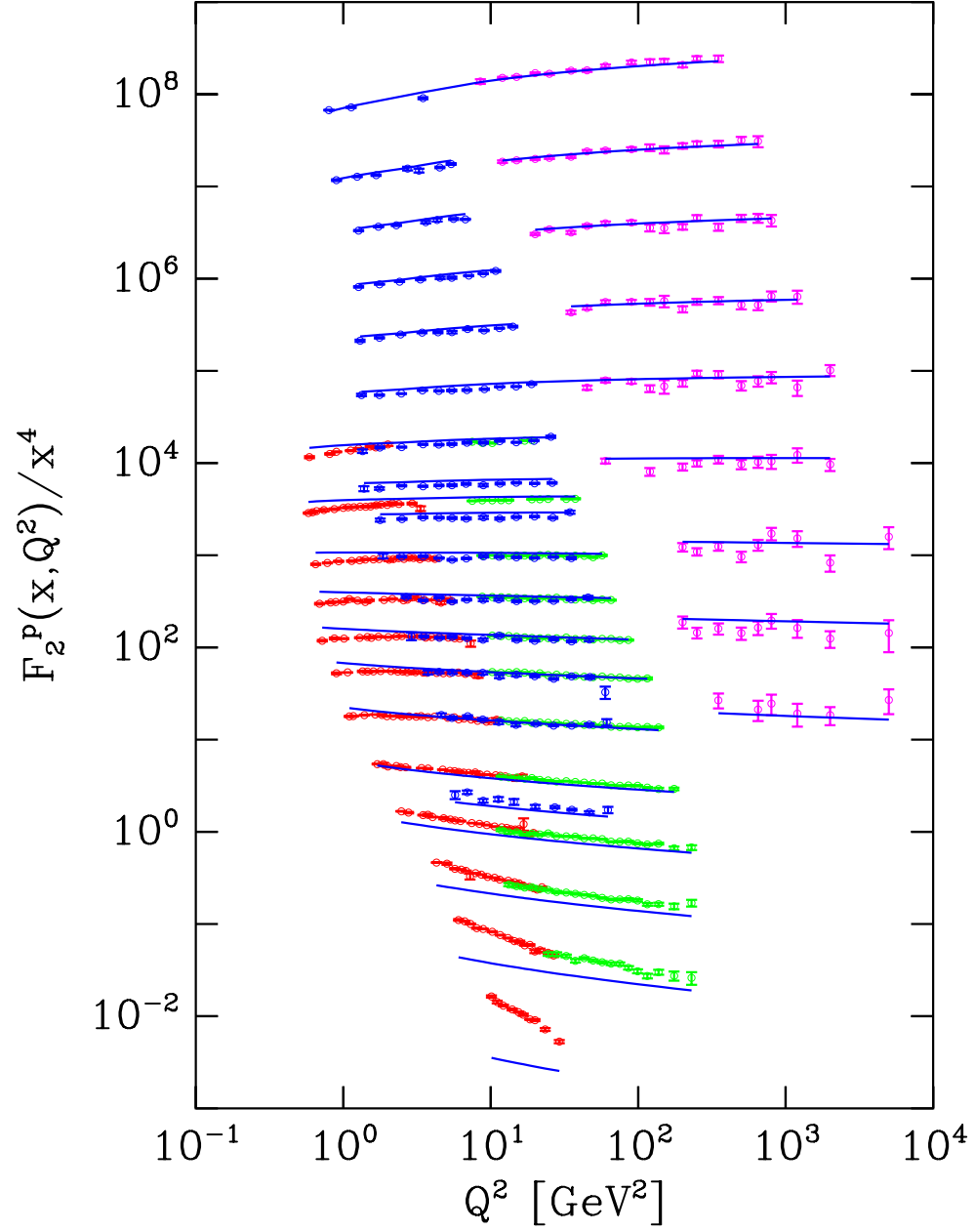
Figure 1.5: Logarithmic scaling violations of the proton structure function F_2^p. The data are from references [28] (red), [29] (green), [30] (blue), [31] (magenta), and the solid lines are the NLO predictions using the CTEQ4 [32] parton distribution functions. Each string of data corresponds to a fixed value of x extending from $x = 0.008$ at the top to $x = 0.85$ at the bottom.
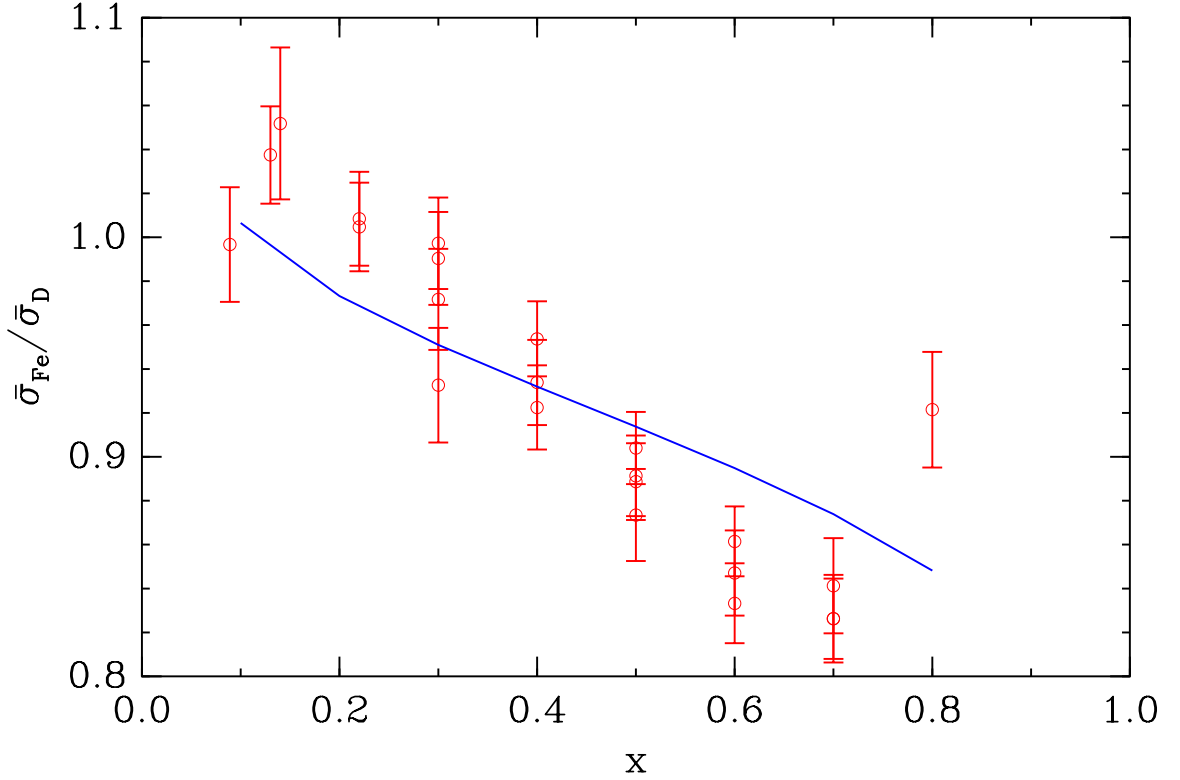
Figure 1.6: The EMC effect as measured by SLAC experiment E139 [35] for ^{56}Fe. Also shown is the calculation using the Q^2 rescaling model. The data cover a Q^2 range of 2 to 15 $(GeV/c)^2$.

1.2 Experiment

Experiment E89-008, performed in Hall C at the Thomas Jefferson National Accelerator Facility (TJNAF), measured inclusive electron scattering cross sections from nuclear targets in the quasielastic region [36]. This experiment was one of the first to make use of the Continuous Electron Beam Accelerator (CEBA) at TJNAF. CEBA provided a 4.045 GeV beam of electrons at currents ranging from 10 to 80 μA. This work reports results of the analysis of ^{12}C, ^{56}Fe, and ^{197}Au data collected with the High Momentum Spectrometer (HMS) operated at laboratory angles of 15, 23, 30,
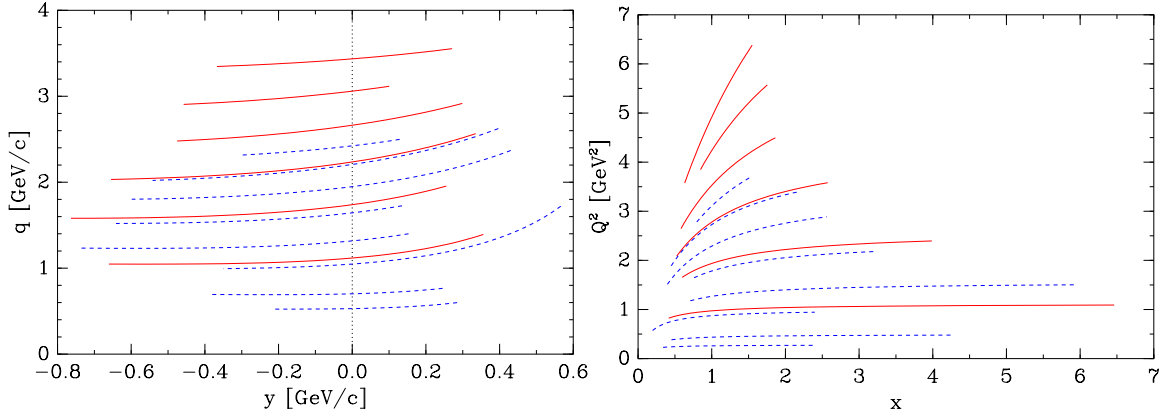
Figure 1.7: Comparison of kinematic coverage for ^{56}Fe for this experiment (solid) and for SLAC experiment NE3 [16] (dashed).

37, 45, and 55 degrees. A summary of the kinematic range for ^{56}Fe is indicated in Figure 1.7; the range for the other targets is similar. These measurements almost double the kinematic coverage of previous experiments.

There are a number of unique aspects to the reduction of this data as compared to the standard Hall C analysis methods. Detector calibration received a great deal of attention, with the goal being to obtain consistent detector response throughout the entire experiment. The analysis code, with the exception of some aspects of the drift chamber tracking, is original work with efficient algorithms inspired by the results of the calibration effort. After event selection, data were reduced to cross sections in a manner which minimized the model dependence of the result. The only analysis tools needed for the entire effort are those commonly found in the UNIX environment.

Chapter 2

Theory

This chapter highlights the theoretical foundation for the ideas presented in the last chapter, beginning with a technical discussion of inclusive electron scattering. The cross section provides a useful connection between the results of scattering experiments and theory. The differential cross section $d\sigma$ is defined by:

$$d\sigma = \frac{1}{\Phi} \, \omega_{i \to f} \, dN_f \qquad (2.1)$$

where Φ is the flux of incident particles and $\omega_{i \to f}$ is the transition rate from the initial target state i into a differential number of final states dN_f. The scattering amplitudes $\langle f|T|i \rangle$ are squared, summed and integrated over all unobserved final

states, and averaged over all unspecified initial states to compute the transition rate:

$$\omega_{i \to f} = (2\pi)^4 \delta^4(p_f - p_i) \overline{\sum} |\langle f|T|i \rangle|^2 \tag{2.2}$$

where p_i and p_f are the total momenta in the initial and final states.

For reference, Figure 2.1 sketches electron scattering from a nucleus A to some final nuclear state X. Electrodynamics dictates that both the electron current $\langle k'|j^\mu|k \rangle$ and the nuclear current $\langle X|J_\mu|A \rangle$ couple to the electromagnetic gauge field A^μ through a term $j_\mu A^\mu$ in the Lagrangian density describing the system dynamics. In leading order of perturbation theory, the single virtual photon approximation, the transition matrix element therefore takes the form:

$$\langle f|T|i \rangle = e^2 \langle k'|j^\mu|k \rangle \frac{1}{Q^2} \langle X|J_\mu|A \rangle \tag{2.3}$$

In this expression, the unit of electromagnetic charge has been explicitly removed from the currents. The middle term represents the propagation of energy $\nu \equiv E - E'$ and momentum $\mathbf{q} \equiv \mathbf{k} - \mathbf{k}'$ through the electromagnetic field, conceptualized as the exchange of a virtual photon of invariant mass $Q^2 \equiv -q_\mu q^\mu = \mathbf{q}^2 - \nu^2$. In the laboratory frame, $Q^2 = 4EE' \sin^2(\theta/2)$ where θ is the electron scattering angle.

Quantum electrodynamics exactly determines the matrix elements of the electron
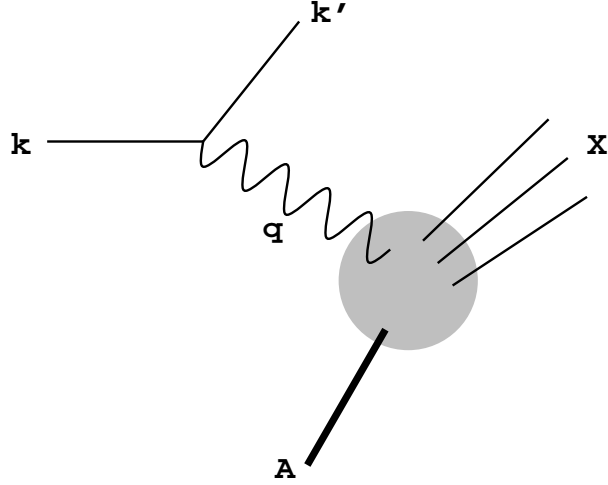
Figure 2.1: The inclusive reaction.

current:

$$\langle k'|j^{\mu}|k\rangle = \sqrt{\frac{m}{E}} \cdot \sqrt{\frac{m}{E'}} \cdot \bar{u}(k')\gamma^{\mu}u(k) \tag{2.4}$$

where the choice of normalization for the plane wave spinors u and $\bar{u}$ determines the two kinematic factors. For unpolarized electron scattering, the summation in equation (2.2) runs over initial and final electron helicities. It is a standard calculation to square equation (2.3) and perform the electron spin sums:

$$\overline{\sum}|\langle f|T|i\rangle|^2 = \frac{(4\pi\alpha)^2}{Q^4} \cdot \frac{1}{4EE'} \cdot \frac{1}{2}\text{Tr}\left[\slashed{k}'\gamma^{\mu}\slashed{k}\gamma^{\nu}\right] \cdot \overline{\sum_A}\langle A|J_{\mu}|X\rangle\langle X|J_{\nu}|A\rangle \tag{2.5}$$

Electron mass terms are neglected in the trace over Dirac indices. The definition $\alpha \equiv e^2/4\pi\hbar c \approx 1/137$ of the fine structure constant and the convention $\hbar = c \equiv 1$ have been applied. The nuclear part of this expression uses the hermiticity of the current, $\langle X|J_{\mu}|A\rangle^{\dagger} = \langle A|J_{\mu}|X\rangle$, and indicates symbolically the summation over initial

nuclear states. It is convenient to introduce:

$$
\begin{aligned}
L^{\mu\nu} &\equiv \frac{1}{2}\mathrm{Tr}\,[\slashed{k}'\gamma^\mu\slashed{k}\gamma^\nu] \\
&= 2\left(k^\mu k'^\nu + k'^\mu k^\nu - k\cdot k' g^{\mu\nu}\right) \\
&= 4K^\mu K^\nu - Q^2\left(g^{\mu\nu} + \frac{q^\mu q^\nu}{Q^2}\right)
\end{aligned}
\tag{2.6}
$$

where $L^{\mu\nu}$ is known as the lepton (electron) tensor, and $K \equiv \frac{1}{2}(k + k')$. Note that K can be written $K = k + \frac{k\cdot q}{Q^2}q$.

It is likewise convenient to define the nuclear tensor $W^A_{\mu\nu}$. For inclusive electron scattering in which none of the final nuclear states are observed:

$$
\begin{aligned}
W^A_{\mu\nu} &\equiv \frac{1}{2\pi}\overline{\sum_{A,X}}\int dN_X\,\langle A|J_\mu|X\rangle\langle X|J_\nu|A\rangle\,(2\pi)^4\delta^4(p_A + q - p_X) \tag{2.7} \\
&= \frac{1}{2\pi}\overline{\sum_{A}}\int d^4\tau\,e^{iq\cdot\tau}\langle A|J_\mu(\tau)J_\nu(0)|A\rangle \tag{2.8}
\end{aligned}
$$

where the latter form, which follows from closure over the final states X and translational invariance over the space-time interval τ, is useful for applications of the operator product expansion and of current algebra. Ultimately, however, $W^A_{\mu\nu}$ must reduce to the form of the most general tensor, consistent with current conservation and parity and time reversal invariance, that can be constructed with the two external

momenta p_A and q:

$$W_{\mu\nu}^A = \frac{W_2^A}{M_A^2} P_\mu P_\nu - W_1^A \left(g_{\mu\nu} + \frac{q_\mu q_\nu}{Q^2} \right) \tag{2.9}$$

where $P \equiv p_A + \frac{p_A \cdot q}{Q^2} q$. The similarity of the tensor structure with equation (2.6) is evident. All of the dynamics observable through unpolarized, inclusive electron scattering are summarized in the two nuclear structure functions W_1^A and W_2^A. An alternate definition of the structure functions, $F_1^A \equiv M_A W_1^A$ and $F_2^A \equiv \nu W_2^A$, is frequently used.

The inclusive electron scattering cross section can now be assembled from equations (2.1, 2.2, 2.5–2.7). Using the box normalization artifice, the incident flux is $\Phi = v_{\rm rel}/V$, where the factor of the box volume V cancels against one implicitly contained in the product $\omega_{i \to f} dN_f$. The laboratory frame relative velocity of the ultrarelativistic incident electron and the target nucleus is $v_{\rm rel} \approx c \equiv 1$. Since the nuclear final state has already been integrated over in the definition of $W_{\mu\nu}^A$, only the scattered electron phase space $d^3 k'/(2\pi)^3 = E'^2 dE' d\Omega/(2\pi)^3$ remains for the inclusive scattering cross section:

$$\frac{d\sigma}{d\Omega dE'} = \frac{\alpha^2}{Q^4} \left(\frac{E'}{E} \right) L^{\mu\nu} W_{\mu\nu}^A \tag{2.10}$$

Contracting the electron and nuclear tensors, this may be written in terms of the
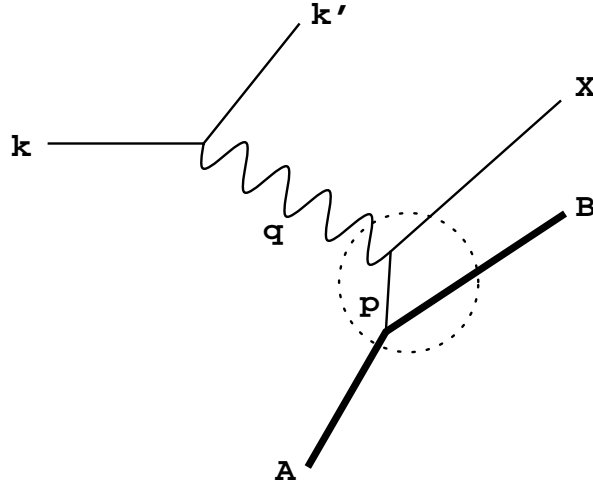
Figure 2.2: The quasifree reaction. This figure represents quasielastic scattering if X is a nucleon.

nuclear structure functions:

$$\frac{d\sigma}{d\Omega dE'} = \sigma_M \left[W_2^A + 2\tan^2\left(\theta/2\right) W_1^A \right] \tag{2.11}$$

where the Mott cross section $\sigma_M \equiv \alpha^2/Q^4 \cdot 4E'^2 \cos^2(\theta/2)$ corresponds to elastic Coulomb scattering from an infinitely massive, spinless, structureless object.

The following sections describe the physics that contributes to the nuclear tensor $W_{\mu\nu}^A$. The quasifree approximation is the simplest means for calculating this quantity, as depicted in Figure 2.2. In this approximation, the nuclear and nucleon contributions to the reaction separate. The virtual photon interacts with individual nucleons which are distributed in energy and momentum within the nucleus; the nuclear dynamics determines this distribution, known as the spectral function, independent of the interaction. The forthcoming discussion mirrors this separation. After a discus-

sion of traditional nuclear theory and the introduction of the spectral function, the individual nucleon elastic and inelastic electromagnetic structure is reviewed. Finally, the nuclear tensor $W_{\mu\nu}^A$ is constructed within the quasifree approximation, and the results are applied to introduce the y-scaling formalism.

2.1 The Nucleus

Despite the strong interactions among nucleons, the nucleus can in first approximation be described as a collection of nucleons moving independently within a central potential. Such a description is called the Independent Particle Shell Model (IPSM). The potential common to all nucleons is known as the mean field, since it is the average potential a single nucleon feels as a result of its interaction with all the other nucleons in the nucleus. Each shell model state is identified by spatial, spin, and isospin quantum numbers; to build a nucleus, these states are successively filled starting from the state of lowest energy, according to the Pauli exclusion principle. The highest occupied state within the IPSM defines the Fermi level. Square well, Woods-Saxon, and spherical harmonic oscillator potentials with parameters tuned to produce RMS charge densities which match experimental measurements are often used. For the Fermi gas model, the special case in which the potential vanishes, the Fermi level is chosen to match the observed nuclear densities.

While these models adequately reproduce the gross properties of nuclei, finer de-

tails and the answer to why the IPSM works so well requires microscopic calculation. The traditional [37, 38, 39] theoretical approach to nuclear physics uses the methods of nonrelativistic many-body quantum mechanics. Since there is no fundamental theory for the interactions among nucleons, the two-body internucleon potential appearing in the many-body Schrödinger equation is parameterized from phase shift analysis of nucleon-nucleon scattering experiments. This interaction shows a strong repulsion below ≈ 0.4 fermi, and mild attraction from meson exchange at long range. For nuclei with three or fewer nucleons, the theory admits exact solution; also, considerable simplifications due to translational invariance permit careful investigation of the properties of nuclear matter, defined as the limiting case of equal but infinite number of neutrons and protons with Coulomb repulsion ignored. Both of these cases provide insight into the far more computationally complex problem of finite nuclei with more than three nucleons.

The Pauli principle plays an important role in nuclear dynamics. Because the internucleon potential can only scatter a nucleon to unoccupied states beyond the Fermi level, the nuclear medium acts to hide the hard core so that its modification of the independent particle wavefunctions do not extend beyond the average internucleon separation. Consequently, an effective potential is often used instead of the "bare" potential; this is actually necessary from a practical point of view, since the hard core produces infinite matrix elements. The Brukner-Bethe-Goldstone method generates such an effective potential as the resummation of an infinite number of interactions

of the bare potential. Often, phenomenological effective potentials are used.

The Hartree-Fock method provides a way to compute the *best* shell model for a nucleus given the effective internucleon potential. This iterative method finds the self-consistent set of independent particle wavefunctions and mean field potential for which the energy of the Slater determinant ground state wavefunction is minimal. To get closer to the physical ground state, more complicated effects are added to this approximate ground state by perturbative methods. For this purpose, a canonical transformation to a particle-hole description is used: the highest occupied level defines the "vacuum" and a matrix element of the internucleon potential is pictured as creating particle-hole pairs. Correlations, for example, are computed as two-particle two-hole admixtures in the nuclear ground state wavefunction. The random phase approximation is one of many methods for computing correlation effects.

Using these methods, the nucleon momentum distribution and other properties of the nuclear ground state may be reliably calculated for $A \leq 3$ nuclei, for the doubly closed shell "magic" nuclei ^{4}He, ^{16}O, ^{40}Ca, ^{208}Pb, and for nuclear matter. The momentum distribution within the approximation described above is the sum of two parts, one part coming from the Hartree-Fock part of the ground state nuclear wavefunction, and the other coming from the correlations. The redistribution of momentum due to the correlations depletes the occupation of the independent particle ground state by about 20%. Three example momentum distributions [40] are illustrated in Figure 2.3. The similarity of the deuteron high momentum tail to those of the complex nuclei
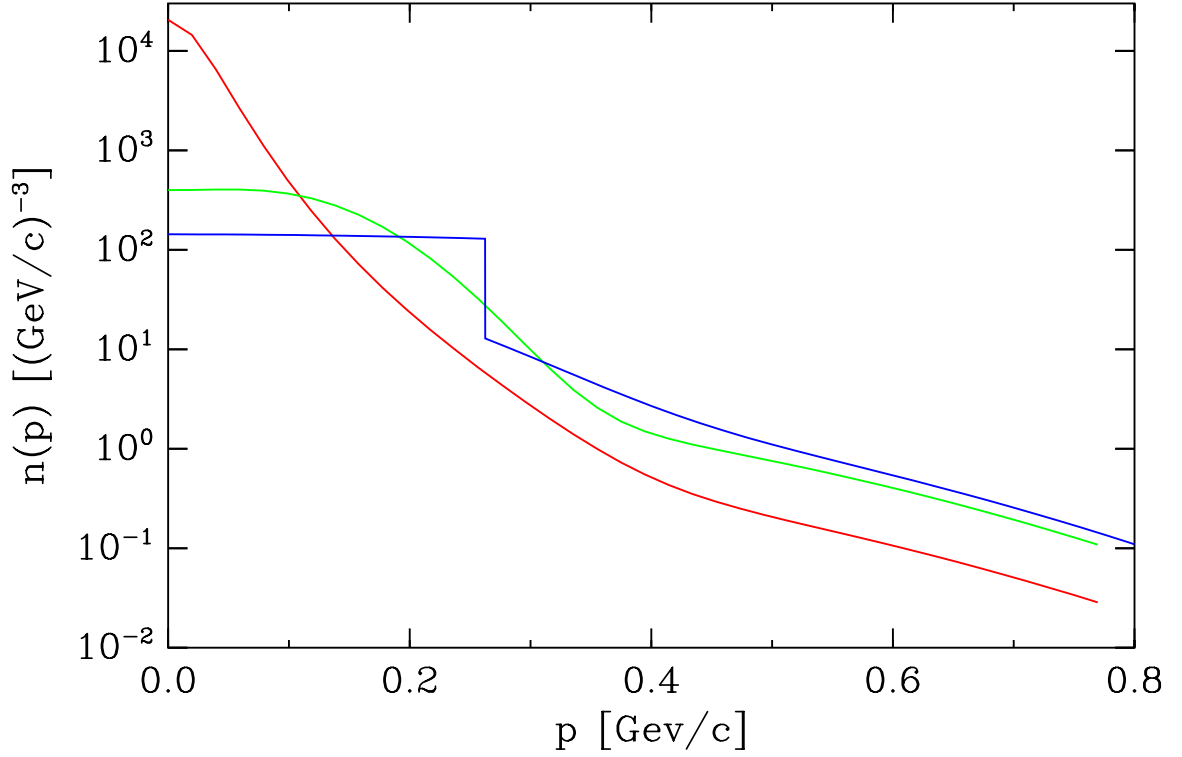
Figure 2.3: Nucleon momentum distribution for the deuteron (red), ^{12}C (green), and nuclear matter (blue).

and nuclear matter indicates the common origin of the contribution of short range correlated pairs in the calculation.

The momentum distribution per nucleon may be formally written using second quantization formalism as the expectation value of the number operator $a^\dagger_\mathbf{p} a_\mathbf{p}$:

$$n(p) = 4\pi \frac{1}{A} \overline{\sum} \langle A | a^\dagger_\mathbf{p} a_\mathbf{p} | A \rangle \tag{2.12}$$

where $p = |\mathbf{p}|$, $a^\dagger_\mathbf{p}$ and $a_\mathbf{p}$ are creation and annihilation operators of single particle states of momentum $\mathbf{p}$, and the average on the sum is over all angular momentum

projections of the nuclear ground state $|A\rangle$. The physical content of the momentum

distribution is contained within the definition of a more complicated quantity, the

spectral function. Inserting a complete set of states for the $A - 1$ nucleon system

between the creation and anihilation operators in the previous equation, while taking

care to express the energy dependence, yields:

$$
\begin{aligned}
n(p) &= \frac{1}{A} \overline{\sum} \langle A|a_{\mathbf{p}}^{\dagger} a_{\mathbf{p}}|A\rangle \\
&= \sum_B \int dE\, \delta(E - E_B) \frac{1}{A} \overline{\sum} |\langle B|a_{\mathbf{p}}|A\rangle|^2 \\
&= \int dE\, S(p, E)
\end{aligned}
\tag{2.13}
$$

The expression for the spectral function takes on a particularly simple form with the

use of the $A - 1$ nucleon Hamiltonian H:

$$
S(p, E) = \frac{1}{A} \overline{\sum} \langle A|a_{\mathbf{p}}^{\dagger} \delta(E - H)\, a_{\mathbf{p}}|A\rangle
\tag{2.14}
$$

These expressions for the momentum distribution and spectral function are normal-

ized according to:

$$
4\pi \int_0^{\infty} p^2\, dp\, n(p) = \int d^3p\, dE\, S(p, E) = 1
\tag{2.15}
$$

The spectral function is a probability distribution describing the likelihood that the

removal of a nucleon with momentum $\mathbf{p}$ from the nucleus A will leave an $A-1$ nuclear system in a state of energy E. When the $A-1$ system is bound, the spectral function contains peaks at specific values of E; however, because these states are generally not pure hole states of the nucleus A, these peaks are broadened. On the other hand, when the $A-1$ system is unbound, the spectral function contains a continuum distribution in E.

Unlike the momentum distribution, calculations of the spectral function only exist for $A \leq 3$ nuclei and nuclear matter. A model spectral function has been constructed [40] which is based upon the characteristics of the results from these calculable cases. This model places all of the bound states into a single delta function peak located at the ground state energy of the $A-1$ system. The momentum distribution under this peak is taken to be that of the harmonic oscillator shell model suitably normalized to the occupation probability. The unbound $A-1$ states are assumed to originate solely from broken correlated pairs. The energy for these states is therefore given by the sum of the kinetic energies of the remaining nucleon of the pair and the $A-2$ system, assumed to be in its ground state, as measured in the $A-1$ center of mass. The momentum balance of the broken pair is most likely carried entirely by the remaining nucleon so that the $A-2$ system is at rest. In this case:

$$E \approx E_0^{A-1} + \frac{p^2}{2M}\left(\frac{A-2}{A-1}\right) \tag{2.16}$$
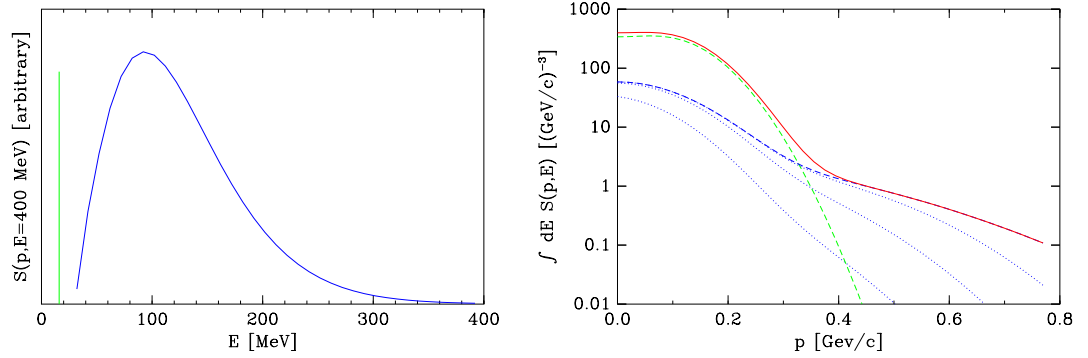
Figure 2.4: The left panel shows a slice of the model spectral function for ^{12}C at p=400 MeV. The right panel shows the missing energy integral of the spectral function: the total momentum distribution is shown in red; the dotted lines indicate the energy integral up to 50, 100, 200 MeV.

where the nuclear masses are taken to be proportional to the nucleon number, and E_0^{A-1} is the ground state energy of the $A-1$ system. The energy dependence of the spectral function is peaked near this energy; less likely configurations in which the remaining nucleon shares the momentum balance with the $A-2$ system generate the width. These features are illustrated in Figure 2.4 for ^{12}C. The right panel shows how the total momentum distribution is recovered as the spectral function is integrated over increasing intervals of E.

2.2   The Nucleon

The free nucleon is a composite object built from quarks. Quarks have a hidden symmetry, an SU(3) color charge, which determines their interactions through a local gauge field. The theory of these interactions is known as Quantum Chromodynamics

(QCD). The SU(3) gauge field and its quanta, referred to as gluons, also carry color, unlike the neutral photons of the U(1) local gauge field responsible for electrodynamics. Gluons can therefore interact with gluons, making QCD a nonlinear theory. Two of the most important consequences of this behavior are confinement and asymptotic freedom. These properties are reflected in the scale dependence of the interaction strength α_s shown in Figure 2.5. At small momentum scales, long range, α_s increases without bound, permanently confining quarks within the color neutral combinations of mesons and baryons. In contrast, at large momentum scales, short distances, α_s becomes weak, and in the asymptotic limit quarks behave as though they are free; that is, QCD exhibits asymptotic freedom. Phenomenological models, such as the bag model [41] or the flux-tube model [42], have been developed to examine the confinement limit where QCD itself is incalculable. On the other hand, asymptotic freedom permits perturbative calculations of QCD properties at large momentum scales, notably the evolution of parton distributions.

Considering inclusive scattering from a free nucleon, the squared invariant mass $W^2 = (p + q)^2 = M^2 + 2M\nu - Q^2$ of the final state provides a useful index of the nucleon structure accessible with the electromagnetic probe. When $W^2 = M^2$, elastic scattering, the reaction is sensitive to the nucleon electric and magnetic form factors. The inelastic response of the nucleon resides above the threshold for pion emission, $W^2 \geq (M + m_\pi)^2$, where it shows a continuum underlying three prominent peaks corresponding to the resonance of numerous clustered, unstable, nucleon excited
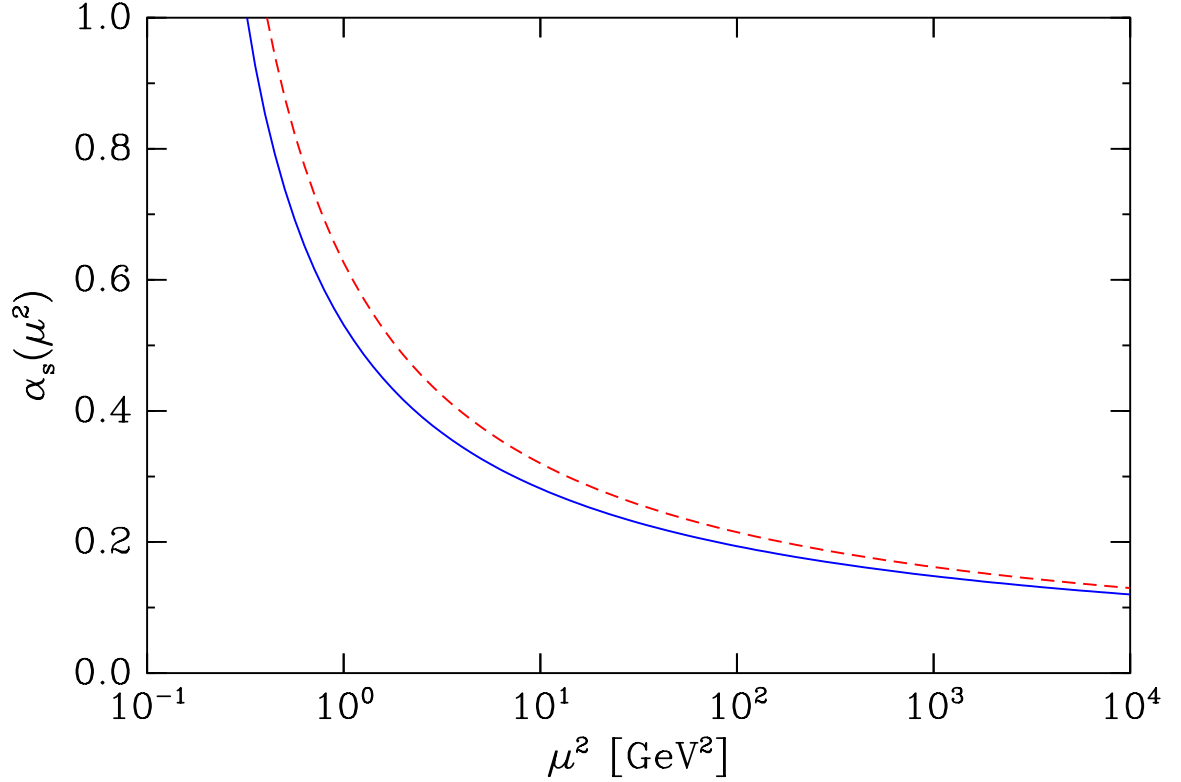
Figure 2.5: The QCD coupling constant at leading (dashed) and next to leading order (solid) for $\Lambda_{\mathrm{QCD}}^{(4)} = 300$ MeV as a function of the renormalization scale.

states. The 300 MeV absorbed to produce the first such excitation, the Δ, goes into flipping a single quark spin. This resonance region response extends to $W^2 \approx 4$ GeV^2 where it blends into the deep inelastic response. In the deep inelastic region, the quark substructure produces a smooth continuum in the nucleon structure functions which is well described at large Q^2 by the parton model and perturbative QCD. The following sections describe nucleon structure in each of these regions in greater detail.

2.2.1 Elastic

Free Nucleons

The nucleon elastic transition current operator between initial and final momentum

states p and p' is characterized by the Dirac and Pauli form factors, F_1 and F_2:

$$
\begin{aligned}
j_N^\mu &= \gamma^\mu[F_1(Q^2) + F_2(Q^2)] - (p + p')^\mu \frac{F_2(Q^2)}{2M} & (2.17) \\
&= \gamma^\mu F_1(Q^2) + i\sigma^{\mu\rho}q_\rho \frac{F_2(Q^2)}{2M} & (2.18)
\end{aligned}
$$

where the anomalous magnetic moment has been absorbed into the definition of

F_2. These two forms are equivalent to one another through the use of the Gordon

decomposition. An alternate way of encapsulating the same information is through

the electric and magnetic Sachs form factors G_E and G_M:

$$
\begin{aligned}
G_E &= F_1 - \tau F_2 \\
G_M &= F_1 + F_2
\end{aligned}
\qquad (2.19)
$$

where $\tau \equiv Q^2/4M^2$.

The Q^2 dependence of these form factors is reasonably well reproduced by the

famous "dipole" form:

$$
G_E^p \approx G_M^p/\mu_p \approx G_M^n/\mu_n \approx G_D \equiv \left[\frac{1}{1 + Q^2/Q_D^2}\right]^2 \qquad (2.20)
$$

where $Q_D^2 = 0.71$ GeV^2, and the magnetic moments are $\mu_p = 2.793$ and $\mu_n = -1.913$. Since the normalization is determined by the static limit and the neutron has no charge, $G_E^n(Q^2) \equiv 0$ within the dipole form. The Galster [43] parameterization:

$$G_E^n = \frac{-\mu_n \tau}{1 + 5.6\tau} G_D \tag{2.21}$$

is frequently used for the neutron electric form factor. It is interesting to note that at low Q^2, where the recoil is nonrelativistic, the dipole shape implies an exponential charge distribution with decay constant $1/Q_D \approx 0.23$ fm.

Measurements are in rough agreement with these parameterizations, although systematic deviation for the proton magnetic form factor is clearly evident for $Q^2 > 1$ GeV^2 and grows to more than 10% beyond $Q^2 = 10$ GeV^2; data for G_E^p and G_M^n are poor enough that the dipole form is as good as any parameterization. G_E^n is the least determined form factor.

Theoretical understanding of the form factors is fragmentary. Vector meson dominance (VMD) models [44] have been applied successfully at low to moderate momentum scales, $Q^2 < 2$ GeV^2. In these models, the nucleon has a Dirac core with structure dynamically generated by the conversion of the virtual photon probe into a virtual neutral vector meson. At large Q^2, constituent counting rules [45] seem to be qualitatively consistent. These rules make the reasonable assumption that in the perturbative region of QCD, the struck nucleon recoils coherently by exchanging

exactly one hard gluon between each constituent quark line; the Q^2 dependence of the form factor may then be computed by counting up the powers of the strong coupling constant and quark and gluon propagators. This gives an α_s^2/Q^4 behavior for F_1 and, taking account of additional suppression from helicity conservation, α_s^2/Q^6 for F_2. A parameterization [46] of the nucleon form factors motivated by both VMD and the consituent counting rules is sometimes used instead of the dipole fit.

Bound Nucleons

Although there has been abundant speculation that the form factors should change when a nucleon is bound within the nuclear environment, there is no unambiguous corroborative experimental result. Noble [47], for instance, originally suggested that the suppression of the longitudinal nuclear response in the quasielastic region could be accounted for by a 30% increase of the nucleon charge radius. On a far more mundane level, however, one clear binding effect is that the energy and momentum of a nucleon, as described in the quasifree approximation with traditional, nonrelativistic nuclear theory, do not satisfy the mass shell relationship $M^2 = E^2 - \mathbf{p}^2$. Such a nucleon is said to be off-shell, and the question arises as to what current operator, form factors, and spinors should be used. It should be stressed that this problem originates in the conceptual inadequacies of nonrelativistic theories; methods of modern relativistic field theories would rephrase binding as a renormalization of the nucleon mass, allowing a consistent treatment of the sharing of momentum and energy between the

interacting fields. Unfortunately, such nuclear theories are not fully developed.

The dubious but generally accepted procedure for inventing an off-shell current is known as the de Forest prescription [48]. There are two such recipes, designated cc1 and cc2, corresponding to the two forms of the nucleon current indicated by equations (2.17) and (2.18). These recipes leave the form factors alone, but continuously extrapolate the free current operator to off-shell kinematics in the following manner. Both forms start by altering the initial nucleon energy to satisfy the mass shell condition $\bar{E} \equiv \sqrt{M^2 + \mathbf{p}^2}$ with the same value of initial 3-momentum $\mathbf{p}$. This alters the free current operator (2.17) in the cc1 case, since the momentum p appearing in the second term is changed to $\bar{p} = (\bar{E}, \mathbf{p})$; there is no such explicit change to the current operator (2.18) in the cc2 form. The second modification is to assume that the initial state is described by a free plane wave spinor $u(\bar{p})$. This affects the calculation of the nucleon tensor when the energy projection operator for these spinors is used to compute the spin sums:

$$\sum_s u_s(\bar{p})\bar{u}_s(\bar{p}) = \frac{\bar{\not{p}} + M}{2M} \tag{2.22}$$

For the cc2 form, this constitutes the entire alteration. For the cc1 form, these two changes completely transform the problem into one of computing the nucleon tensor for a free, moving nucleon with initial momentum $\bar{p}$. Using equation (2.7):

$$\widetilde{W}_{\mu\nu}^N = \frac{1}{2\pi} \sum_{\bar{p},p'} \int \frac{d^3p'}{(2\pi)^3} \langle\bar{p}|j_\mu^{cc1}|p'\rangle\langle p'|j_\nu^{cc1}|\bar{p}\rangle \, (2\pi)^4\delta^4(\bar{p} + \bar{q} - p')$$

$$
\begin{aligned}
&= \frac{1}{4\bar{E}E'} \cdot \frac{1}{2}\mathrm{Tr}\left[(\slashed{\bar{p}} + M)j_\mu^{\mathrm{cc1}}(\slashed{p}' + M)j_\nu^{\mathrm{cc1}}\right]\delta(\bar{E} + \bar{\nu} - E') \\
&= \frac{1}{4\bar{E}E'}\left[4\left(F_1^2 + \frac{\bar{Q}^2}{4M^2}F_2^2\right)\bar{P}_\mu\bar{P}_\nu \right. \\
&\qquad\qquad \left. -\bar{Q}^2(F_1 + F_2)^2\left(g_{\mu\nu} + \frac{\bar{q}_\mu\bar{q}_\nu}{\bar{Q}^2}\right)\right]\delta(\bar{E} + \bar{\nu} - E') \qquad (2.23)
\end{aligned}
$$

As in past expressions, $\bar{P} \equiv \bar{p} + \frac{\bar{p}\cdot\bar{q}}{\bar{Q}^2}\bar{q} = \frac{1}{2}(\bar{p} + p')$ is introduced. The difference $p' - \bar{p}$ is replaced by $\bar{q}$ everywhere it appears in the calculation of the trace, as are the related quantities $E' - \bar{E} \equiv \bar{\nu}$ and $\bar{q}^2 \equiv -\bar{Q}^2$.

Neither the off-shell current nor the off-shell nucleon tensor satisfy current conservation: $q^\mu j_\mu^{\mathrm{cc1}} \equiv \nu\rho^{\mathrm{cc1}} - |\mathbf{q}|j_L^{\mathrm{cc1}} \neq 0$, and $q^\mu \widetilde{W}_{\mu\nu}^N \neq 0$. To restore current conservation, the last step of the de Forest prescription is to enforce the equality by explicitly substituting the charge for the longitudinal current using $j_L^{\mathrm{cc1}} \to \nu\rho^{\mathrm{cc1}}/|\mathbf{q}|$. This substitution is carried through for any matrix elements involving longitudinal indices in $\widetilde{W}_{\mu\nu}^N$. When computing a cross section, this substitution is most easily done by manipulating the contraction with the lepton tensor (2.6):

$$
\begin{aligned}
L^{\mu\nu}\widetilde{W}_{\mu\nu}^N &= \left[4\left(K_0 - \frac{\nu}{|\mathbf{q}|}K_L\right)^2 - \frac{Q^4}{|\mathbf{q}|^2}\right]\widetilde{W}_{00}^N \\
&\quad -4\left[K_0 - \frac{\nu}{|\mathbf{q}|}K_L\right]\cos\phi\left(\widetilde{W}_{0\mathrm{T}}^N + \widetilde{W}_{\mathrm{T}0}^N\right) \\
&\quad +\left[4K_T^2\cos^2\phi + Q^2\right]\widetilde{W}_{\mathrm{TT}}^N \qquad (2.24)
\end{aligned}
$$

where ϕ is the angle between the electron and the nucleon scattering planes. For

inclusive calculations, ϕ is integrated over, and only the $\widetilde{W}_{00}^N$ and $\widetilde{W}_{TT}^N$ components contribute.

2.2.2 Inelastic

As previously described, there are two regions of inelastic response, the resonance region and the deep inelastic region. The structure functions in the resonance region, like the elastic form factors, are difficult to understand from first principles of QCD, so a parameterization [49] of W_1^N and W_2^N from an experimental survey of this region is frequently used. The behavior of W_1^N and W_2^N in the deep inelastic region, on the other hand, provides direct contact at large Q^2 with the predictions of the parton model and perturbative QCD.

The Parton Model and Perturbative QCD

The parton model describes the nucleon as a collection of noninteracting, massless, spin $\frac{1}{2}$ constituents. These partons correspond to the flavored quarks and antiquarks of QCD. A parton distribution function $f(x, Q^2)$ characterizes the probability density for finding a parton of flavor f carrying a momentum fraction $x \equiv Q^2/2M\nu$ of the nucleon four-momentum p_N. Inelastic scattering from the nucleon is therefore pictured as elastic scattering from partons of momentum xp_N, summed incoherently over all flavors of partons and weighted by the parton distribution functions. The

nucleon structure function $F_2^N \equiv \nu W_2^N$ takes the form:

$$F_2^N(x, Q^2) = x \sum_f e_f^2 \left[f(x, Q^2) + \bar{f}(x, Q^2) \right] \tag{2.25}$$

where e_f is the charge of the flavor f. The Callan-Gross relationship $F_1^N = F_2^N/2x$ determines the other structure function $F_1^N \equiv MW_1^N$.

In the Bjorken limit, where both $\nu \to \infty$ and $Q^2 \to \infty$ such that x remains fixed, the absence of interactions in the parton model leads to Bjorken scaling, the property that the parton distributions, and therefore the structure functions, depend solely upon the Bjorken variable x. The measured structure functions, however, do not scale exactly; rather, they show a logarithmic dependence on Q^2. It is a unique characteristic of asymptotically free theories like QCD that the scaling violations have a logarithmic dependence instead of a stronger inverse power law. This dependence follows from a perturbative analysis of the radiative corrections in QCD, and is summarized by the Altarelli-Parisi evolution equations for the structure functions and parton distributions. The evolution of flavor nonsinglet parton combinations, such as the valence quark distributions $V(x, Q^2) = \sum_f f(x, Q^2) - \bar{f}(x, Q^2)$, is given at leading order by:

$$\frac{d\, V(x, Q^2)}{d \log Q^2} = \frac{\alpha_s(Q^2)}{2\pi} \int_x^1 \frac{dy}{y} V(y, Q^2) P_{qq}(x/y) \tag{2.26}$$

The evolution equations for the flavor singlet sea quark and gluon distributions are
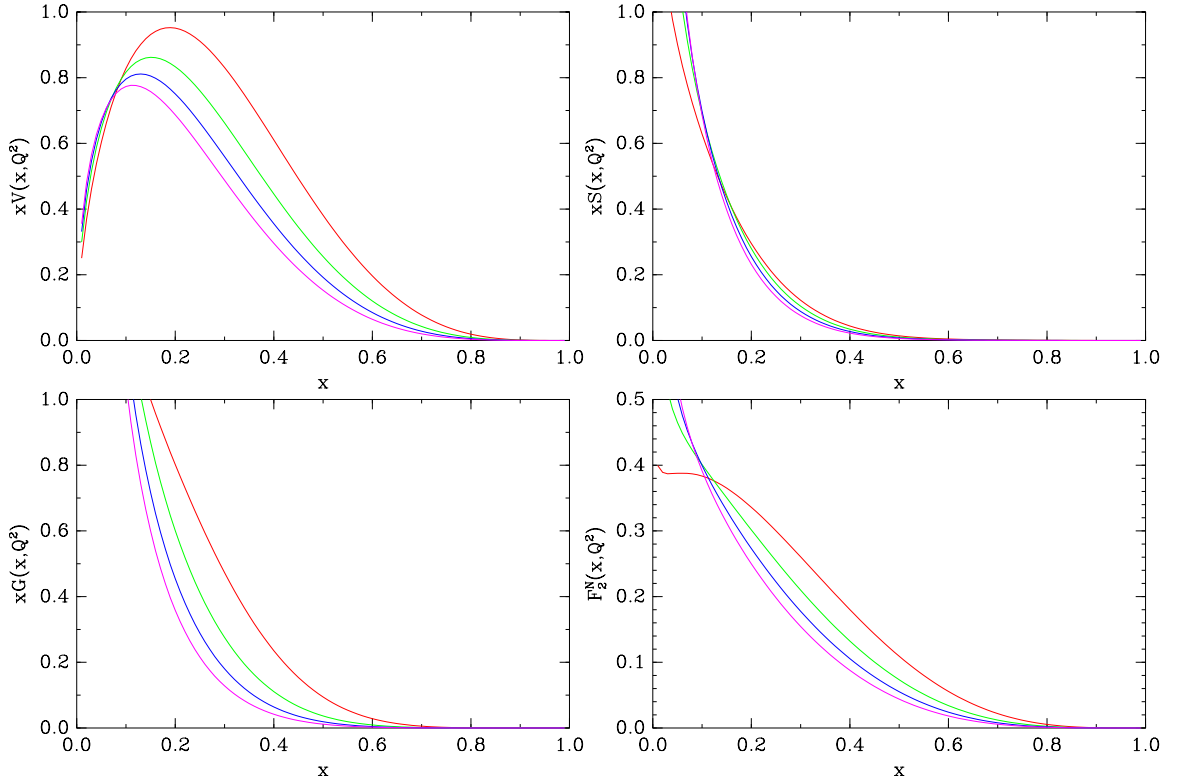
Figure 2.6: Valence, sea, and gluon parton distributions, and the total nucleon struc-
ture function $F_2^N(x, Q^2)$ at 3 (red), 30 (green), 300 (blue), and 3000 (ma-
genta) GeV^2.

similar but coupled due to the dissociation of gluons into quark-antiquark pairs. The

splitting function $P_{qq}(z)$ is the probability for a parton to lose $1 - z$ of its momentum

to gluon emission. Figure 2.6 illustrates the Q^2 dependence of the valence, sea, and

gluon distributions and of F_2^N as calculated using the CTEQ4 [32] parameterizations

and next-to-leading order evolution.

The physical interpretation of the evolution equations and the concept of renor-

malization are closely related. The parton distribution functions must be defined at

some arbitrary initial momentum scale $Q^2 = \mu^2$ in order to apply the evolution equa-

tions. The partons resolved at this momentum scale are not fundamental quarks; they are effective quarks obtained by integrating over all fluctuations at higher momentum (shorter distance) scales, and their distribution in the nucleon is determined by confinement physics at lower momentum scales. At present only experiment can provide these initial distributions. However, because QCD determines the fundamental interactions, the way the fluctuations reveal themselves when the partons are probed at shorter distance scales can be computed within perturbation theory by considering the most likely process, collinear gluon emission. The invariance of the predictions to the choice of the arbitrary renormalization scale μ^2 reflects a self-similarity within QCD described by the Callan-Symanzik renormalization group equations.

A more sophisticated approach to the evolution of the structure functions exploits their sensitivity in the Bjorken limit to the dynamics on the lightcone [6, 50]. The importance of the lightcone is evident from equation (2.8) where the nucleon tensor is written as the Fourier transform of the product of currents acting at points separated by the space-time interval τ. On the lightcone defined with respect to $-\mathbf{q}$, the component $q^- \equiv (\nu + |\mathbf{q}|)/\sqrt{2} \to \infty$ in the Bjorken limit, while q^+ remains finite. As usual, the oscillation of the exponential makes the Fourier transform sensitive to regions of τ inversely related to q; since $q \cdot \tau = q^- \tau^+ + q^+ \tau^-$, the divergence of q^- forces $\tau^+ \to 0$. This limit and the causality condition $0 < \tau^2 \equiv 2\tau^+ \tau^- - \tau_\perp^2$ together imply that $\tau^2 \to 0$, which is the definition of the lightcone. Consequently, the Bjorken limit selects the lightcone properties of the bilocal product of currents.

In order that the Fourier transform be nonzero in the Bjorken limit, as the near scaling of the observed structure functions requires, the oscillation of the exponential also demands that the product of currents diverge on the lightcone. The fluctuations in any quantum field theory result in such singularities, but only the singularities present in a *free* field theory predict *exact* Bjorken scaling. In fact, explicit calculation of the dominant lightcone singularity in the bilocal product of free field currents leads to the parton model description of nucleon structure. Since q^+ is the only finite momentum remaining in the Bjorken limit, the Nachtmann variable [51] naturally emerges:

$$\xi \equiv -\frac{q^+}{p^+} = \frac{|\mathbf{q}| - \nu}{M} = \frac{2x}{1 + \sqrt{1 + 4M^2x^2/Q^2}} \to x \qquad (2.27)$$

In this analysis, the parton distribution functions represent the probability density for finding a parton carrying a fraction ξ of the nucleon *lightcone* momentum p^+.

The Nachtmann variable was originally introduced within the context of the Operator Product Expansion (OPE). The OPE organizes the dominant lightcone singularities for the fully interacting theory. It rewrites the bilocal product of currents with an asymptotic expansion in local operators consisting of quark fields and covariant derivatives. The operators with the dominant singularity in the Bjorken limit are those for which the difference of their canonical dimension and their spin is two; this difference is called twist. It is the renormalization group equations for these operators that determine the evolution of the structure functions. In fact, the anomalous
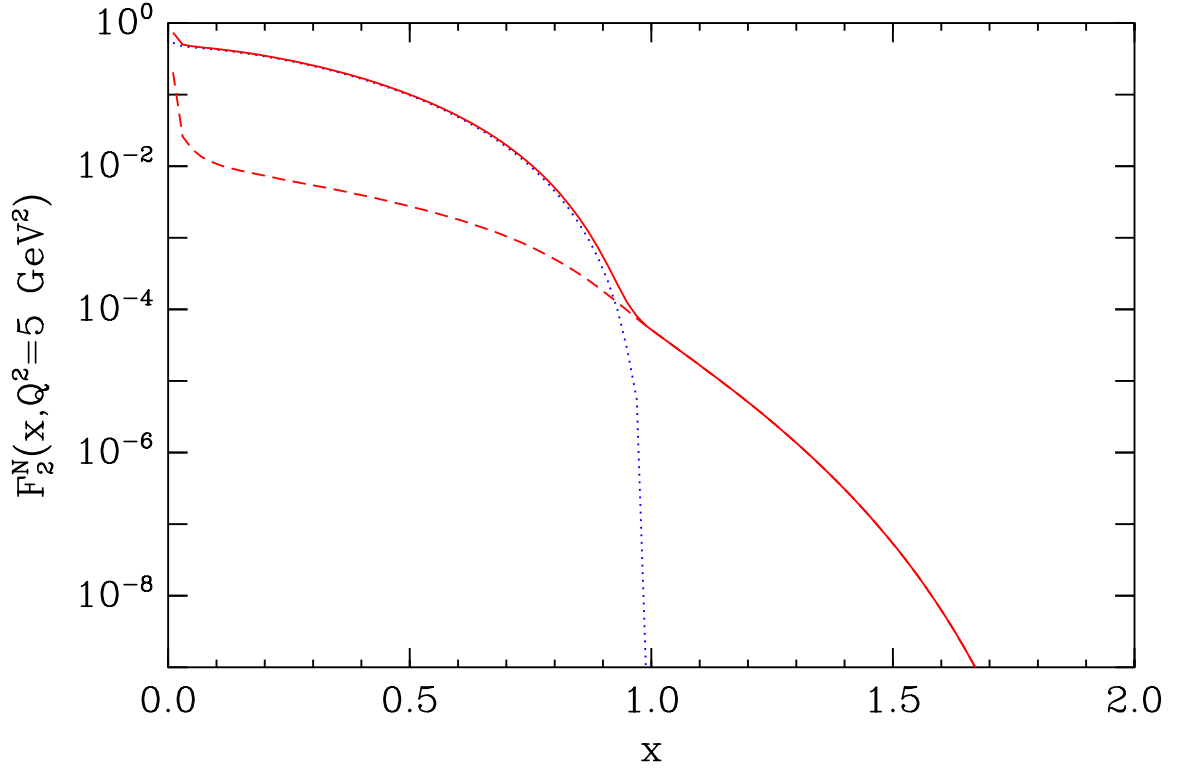
Figure 2.7: Parton recombination modifications (dashed) to the nucleon structure function F_2^N (dotted) at $Q^2 = 5$ GeV^2 for ^{56}Fe; the solid line gives the total structure function.

dimension of the twist-two operators of spin n give the order n moments in x of the Altarelli-Parisi splitting functions when quark masses are neglected. When quark masses are retained, moments in ξ are required to project out operators of pure spin.

Nuclear Effects

As in the case of the elastic form factors, little consensus exists for nuclear modifications of the inelastic structure functions. Two interesting ideas grounded in QCD address this topic: Q^2 rescaling, mentioned in Chapter 1, and parton recombination.

Parton recombination [52] is an explicit mechanism calculable within perturbative QCD for (at least part of) the short range modification of nucleon structure in a nucleus. This mechanism allows the partons of a nucleon placed in the nuclear environment to recombine, or fuse, with partons of a neighboring nucleon, forming a single parton carrying the sum of the initial parton momenta. Initial state recombination therefore populates the $x > 1$ region with quarks that have absorbed momentum from neighboring gluons. The modification to the valence parton distribution, and the nonsinglet part of F_2^N, is determined by:

$$
\begin{aligned}
\Delta V(x, Q^2) &= \frac{3}{2} R_A \bar{n}_A \frac{4\pi \alpha_s(Q^2)}{Q^2} \\
&\times \left[\int_x^1 dy\, V(y) G(x-y) \Gamma_{qq}(y, x-y, x) \right. \\
&\left. -V(x) \int_0^1 dy\, G(y) \Gamma_{qq}(x, y, x+y) \right]
\end{aligned}
\tag{2.28}
$$

where $\bar{n}_A$ and R_A are the nucleon density and radius of the nucleus, G is the gluon distribution, and Γ_{qq} are parton fusion functions, analogous and closely related to the splitting functions in the Altarelli-Parisi evolution equations. Figure 2.7 illustrates the total parton recombination contribution to the nucleon structure function computed for $Q_0^2 = 5$ GeV^2. The scale Q_0^2 at which this modification is computed is completely undetermined and must be fixed by experiment. Although equation (2.28) indicates a $1/Q^2$ dependence, the additional effect of recombination with glue radiated into the final state locks in the modification leading to slow Q^2 dependence. In fact, the

radiative recombination effects have been shown to be legitimate additions to the Altarelli-Parisi evolution equations [53].

2.3   The Quasifree Reaction and y-scaling

The inclusive electromagnetic nuclear tensor $W^A_{\mu\nu}$ can be calculated using the quasifree reaction mechanism and the results of the previous two sections for the nuclear spectral function and the individual nucleon (off-shell) tensors $\widetilde{W}^N_{\mu\nu}$. The quasifree reaction requires the assumption that the nuclear many-body current is given by the sum of one body nucleon currents:

$$J_\mu \approx \sum_{p,p'} \langle p'|j^N_\mu|p\rangle \, a^\dagger_{\mathbf{p}'} a_{\mathbf{p}} \qquad (2.29)$$

where j^N_μ is the one-body nucleon current operator. In the matrix element between initial $|A\rangle$ and final $|B,X\rangle$ plane wave states, only the term for which $\mathbf{p} = \mathbf{p}_A - \mathbf{p}_B$ and $\mathbf{p}' = \mathbf{p}_X$ survives:

$$\langle B,X|J_\mu|A\rangle = \langle p_X|j^N_\mu|p\rangle \, \langle B|a_{\mathbf{p}}|A\rangle \qquad (2.30)$$

This separation of the nuclear matrix elements which make up the spectral function from the individual nucleon current is the entire content of the quasifree reaction mechanism. Inserting this expression for the nuclear current into equation (2.7) for

the nuclear tensor and using the definitions of the spectral function and the individual nucleon tensor yields:

$$
\begin{aligned}
W_{\mu\nu}^A &= \frac{1}{2\pi} \overline{\sum_{A,B,X}} \int dN_B \, dN_X \, (2\pi)^4 \delta^4(p + q - p_X) \\
&\qquad \times \langle p | j_\mu^N | p_X \rangle \langle p_X | j_\nu^N | p \rangle \, \langle A | a_{\mathbf{p}}^\dagger | B \rangle \langle B | a_{\mathbf{p}} | A \rangle \\
&= \int dE_m \, d\mathbf{p} \, \widetilde{W}_{\mu\nu}^N(p, q, p_X) \, S(p, E_m)
\end{aligned}
\tag{2.31}
$$

No reference has been made to the nature of the nucleon final state, so this expression may be used for inelastic as well as quasielastic calculations depending upon the choice for $\widetilde{W}_{\mu\nu}^N$.

Using equations (2.23,2.24) for the off-shell elastic nucleon tensor and its contraction with the lepton tensor, and assuming the spectral function is the same for neutrons and protons, the cross section for quasielastic scattering derived from equation (2.31) takes the form:

$$
\begin{aligned}
\frac{d\sigma^{\mathrm{QE}}}{d\Omega dE'} &= \int dE_m \, d\mathbf{p} \, (Z\tilde{\sigma}_p + N\tilde{\sigma}_n) \\
&\qquad \times \delta(M_A - E_B + \nu - E_X) \, S(p, E_m)
\end{aligned}
\tag{2.32}
$$

where $\tilde{\sigma}_{p,n}$ are off-shell elastic cross sections, and Z and N are the number of protons and neutrons. The energy of the final state nucleon X is $E_X = \sqrt{M^2 + (\mathbf{p} + \mathbf{q})^2}$. The missing energy E_m determines the invariant mass M_B of the residual nuclear state B

according to $E_m = M_B + M - M_A$. When B is the $A-1$ ground state of mass M_{A-1}, the missing energy is minimal $E_{\min} \equiv M_{A-1} + M - M_A$. At most $M_B = W - M$, where $W^2 = (p_A + q)^2 = (M_A + \nu)^2 - |q|^2$ is the invariant mass of the total final nuclear state, so $E_{\max} = W - M_A$. Since B recoils with $-\mathbf{p}$, its energy is $E_B = \sqrt{M_B^2 + \mathbf{p}^2}$.

The y-scaling analysis [54, 55, 4] of quasielastic scattering starts from equation (2.32). The energy conserving delta function controls many of the important details of this analysis. For a given E_m, it enforces a specific relationship between the longitudinal p_L and transverse p_T components of $\mathbf{p}$ as defined with respect to $\mathbf{q}$. This relationship has the property that both the minimum and the maximum allowed values for the magnitude $p = |\mathbf{p}| = \sqrt{p_L^2 + p_T^2}$ are determined by entirely longitudinal momenta; symbolically, $p_{\min}(E_m) = |p_L^{\min}(E_m)|$ and $p_{\max}(E_m) = |p_L^{\max}(E_m)|$. For the particular case of $E_m = E_{\min}$, the minimal longitudinal momentum $p_L^{\min}(E_{\min})$ defines the y-scaling variable:

$$y = -\frac{W^2 + M_{A-1}^2 - M^2}{2W^2} \left(|\mathbf{q}| - (M_A + \nu) \left[1 - \frac{4W^2 M_{A-1}^2}{(W^2 + M_{A-1}^2 - M^2)^2} \right]^{1/2} \right) \quad (2.33)$$

This expression follows from an explicit calculation using energy conservation or, more simply, the mass shell condition $p_X^2 = M^2$.

The quasielastic cross section in equation (2.32) may be written in terms of the y-scaling function $F(y, |\mathbf{q}|)$ after integrating over the azimuthal and polar angles ϕ and θ of $\mathbf{p}$. The azimuthal symmetry of the inclusive off-shell cross sections and of

the spectral function make the integration of ϕ trivial. Integration over $\cos\theta$ with the energy conserving delta function leaves a factor of $E_X/|\mathbf{q}||\mathbf{p}|$ from the dependence of the delta function argument. Since they do not vary much over the breadth $\approx k_F$ of the spectral function, the $E_X/|\mathbf{q}|$ term and the off-shell cross sections may be removed from the remaining two integrals over E_m and p and evaluated at kinematics corresponding to the lower integration limits, up to an error of at most $\approx (k_F/M)^2$. These steps lead to:

$$\frac{d\sigma^{\text{QE}}}{d\Omega dE'} \approx (Z\tilde{\sigma}_p + N\tilde{\sigma}_n) \cdot \frac{E_X}{|\mathbf{q}|} \cdot 2\pi \int_{E_{\min}}^{E_{\max}} dE_m \int_{p_{\min}(E_m)}^{p_{\max}(E_m)} p\,dp\,S(p, E_m) \qquad (2.34)$$

The double integral over the spectral function defines the nuclear y-scaling function $F(y, |\mathbf{q}|)$, where the integration limits contain the y and $|\mathbf{q}|$ dependence. Scaling of $F(y, |\mathbf{q}|)$ is the simple statement that the two-dimensional integration region does not change significantly for kinematics having the same value of y; furthermore, within this derivation the scaling limit is approached from below as the integration of positive-definite spectral function becomes more complete.

To demonstrate the scaling properties of $F(y, |\mathbf{q}|)$, the $|\mathbf{q}| \rightarrow \infty$ limit must be considered. The upper bounds of both integrals tend to infinity in this limit, so all of the kinematic dependence comes from the lower bound $p_{\min}(E_m) = |p_L^{\min}(E_m)|$ on the momentum integral. The energy conservation equation as $|\mathbf{q}| \rightarrow \infty$ for longitudinal

nucleons becomes $M_A + \nu = p_L + |\mathbf{q}| + \sqrt{M_B^2 + p_L^2}$, which is readily inverted:

$$p_L^{\min}(E_m) \rightarrow \frac{(M_A + \nu - |\mathbf{q}|)^2 - M_B^2}{2(M_A + \nu - |\mathbf{q}|)} \tag{2.35}$$

but the combination $M_A + \nu - |\mathbf{q}| = y + \sqrt{M_{A-1}^2 + y^2}$ according energy conservation again and the definition $y \equiv p_L^{\min}(E_{\min})$. Therefore $p_L^{\min}(E_m)$ depends only on y, and $F(y, |\mathbf{q}|)$ scales in the limit $|\mathbf{q}| \rightarrow \infty$.

At finite but large $|\mathbf{q}|$, it is usually a good approximation to set the upper integration limits to infinity. It is also useful to rewrite $F(y, |\mathbf{q}|)$ by breaking the momentum integral into two parts:

$$
\begin{aligned}
F(y, |\mathbf{q}|) &= 2\pi \int_{E_{\min}}^{\infty} dE_m \left[\int_{|y|}^{\infty} - \int_{|y|}^{p_{\min}(E_m)} \right] p \, dp \, S(p, E_m) \\
&= 2\pi \int_{|y|}^{\infty} n(p) \, p \, dp \, - \, B(y, |\mathbf{q}|) \tag{2.36}
\end{aligned}
$$

The subtracted term defines the "binding" correction [56]. Evidently, the continuum missing energy distribution in the spectral function spoils a direct connection of the y-scaling function with the nucleon momentum distribution by an amount determined by $B(y, |\mathbf{q}|)$. This connection is preserved, however, for the special case of the deuteron, which has a single bound state and no continuum. The binding correction for the general case persists even in the limit $|\mathbf{q}| \rightarrow \infty$, and scales, according to the same arguments described above. As an illustration of this effect, Figure 2.8 com-
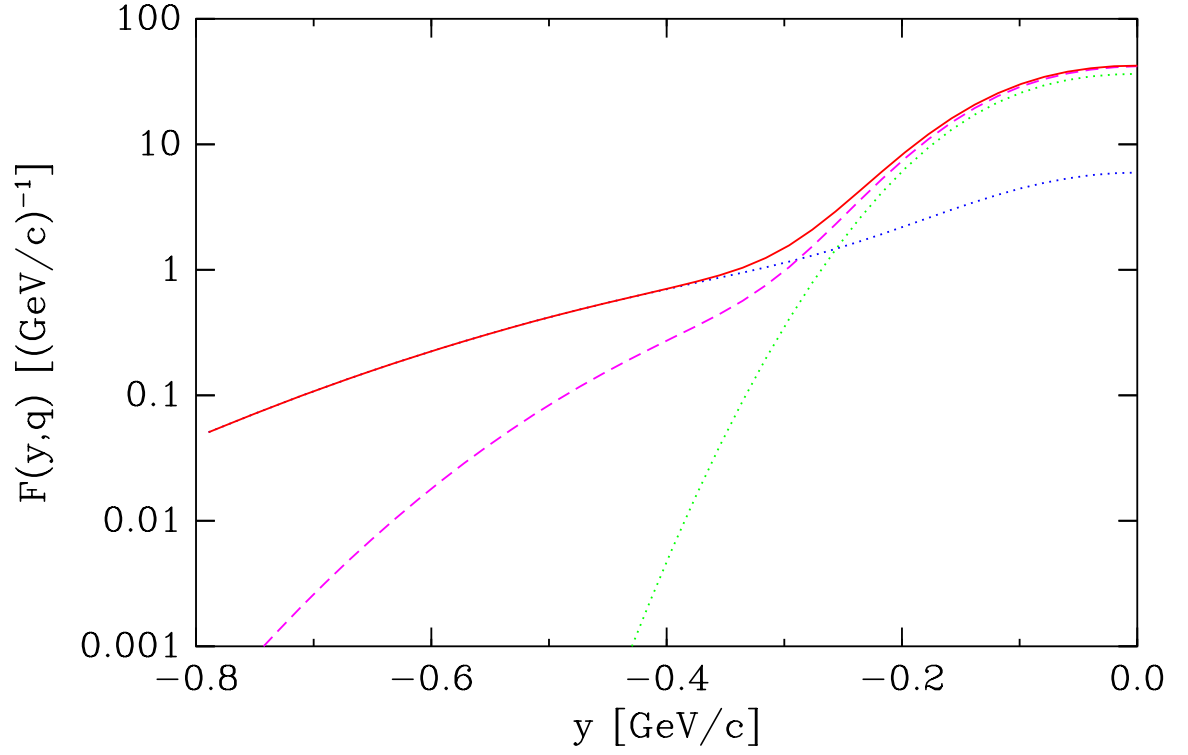
Figure 2.8: $F(y, |\mathbf{q}|)$ for ^{12}C. See the text for details.

pares the scaling function with (dashed) and without (solid) the binding correction for ^{12}C as calculated using the model spectral function described previously. The dotted lines indicate the separate contributions of the independent particle and correlation contributions, respectively, to the total momentum distribution.

Chapter 3

Apparatus

All equipment necessary for the execution of this experiment can be categorized as components of one of five main systems. The first such system is the Continuous Electron Beam Accelerator (CEBA), which delivered a 4.045 GeV continuous wave electron beam at currents ranging from 10 to 80 μA. The second is the Hall C Beam-line. The components of this system transported the beam into the experimental hall, applied a raster, and performed current and position measurements. The third, the target system, inserted solid targets of ^{12}C, ^{56}Fe, or ^{197}Au, or cryogenic targets of hydrogen or deuterium into the beam. The fourth main system is the High Momentum Spectrometer (HMS). The magnetic optics of the HMS focused and dispersed charged particles into a set of detectors. A pair of drift chambers measured trajectories, four hodoscope planes both served as the basis of the trigger and provided an accurate timing, and a Čerenkov detector and calorimeter performed particle identification.

51

The fifth and last main system is the data acquisition. Valid events latching the trigger logic initiated the digitization of the signals from the detectors and the transfer of this data from front-end module memory to disk. The following sections describe the function of each of these five systems and their components in detail.

3.1 Accelerator

The Continuous Electron Beam Accelerator (CEBA) [57, 58, 59] at TJNAF, illustrated in Figure 3.1, is a superconducting, recirculating, continuous wave accelerator capable of delivering independent current and energy beams to three experimental halls. At the time of this experiment, energies available were 45 MeV plus multiples of 800 MeV up to a total of 4.045 GeV, and current up to 200 μA. The beam quality is exceptional, with energy spread less than 1×10^{-4}, emittance less than 2×10^{-4} mm·mrad at maximum energy, and spot size less than 200 μm. Superconducting radio-frequency (SRF) accelerating cavities are the crucial piece of technology necessary for achieving such beam characteristics.

3.1.1 Cavities

CEBA relies upon superconducting radio frequency acceleration cavities. Development of this crucial piece of technology began at HEPL in the 1960's and 70's. In the mid-1980's, the resolution of current and gradient limitations, originating from un-
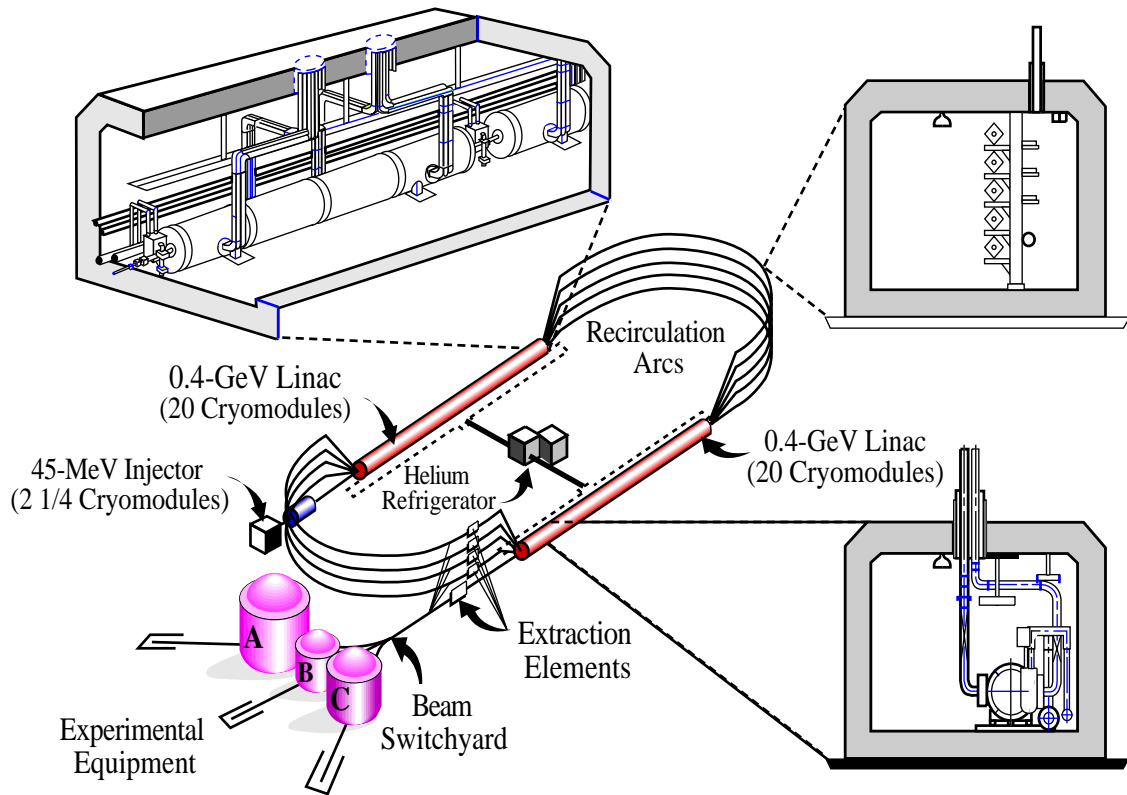
Figure 3.1: Continuous Electron Beam Accelerator (CEBA).

damped higher order modes and multipacting, led to the viability of this technology for large scale application. Ultimately, CEBAF adopted a Cornell University design for the cavities and contracted with Siemens for their manufacture.

Each niobium cavity consists of five half wavelength cells with cylindrically symmetric elliptical inner surfaces. There are waveguide couplers at both ends of the cavity, at one end one coupler for RF input, and at the other end two couplers at right angles for extraction and suppression of higher order modes. Two cavities joined at their RF input ends by a 1.25 wavelength niobium spacer form the basic accelerat-

ing unit. Each cavity is mechanically tuned to match the machine operating frequency of 1497 MHz. On average, the cavities resonate with a quality factor of 5×10^9, and produce an accelerating gradient of 9 MV/m. Both of these figures are a factor of two above the design specification. By comparison, conventional accelerating cavities at SLAC produce a similar gradient but have $Q \approx 2 \times 10^4$; the improvement, of course, comes from the superconductivity of the niobium.

This extremely efficient transfer of RF power into beam power makes modest requirements of the RF power systems. Each cavity has its own dedicated 5 kW klystron. The associated RF controls achieve power and phase regulation to better than 1×10^{-4} and 0.03 degrees, respectively. The klystron per cavity design allows for the operation of each cavity, if necessary, at maximum gradient.

Each cavity pair is mounted inside a liquid helium (LHe) vessel. An inner magnetic shield followed by a superinsulation blanket, an outer magnetic shield, a thermal radiation shield, and another superinsulation blanket surrounds the vessel. The whole assembly is contained within an isolation vacuum shell. Four such cryounits are grouped as a cryomodule. All four LHe vessels are connected and filled so that the cavities are submerged in a bath of 2 K LHe with a vapor pressure of 0.031 atm. The 2 K liquid is Joule-Thompson expanded from a 2.2 K supply at 2.8 atm from the Central Helium Liquifier (CHL). A warm helium line maintains the thermal radiation shields at 40 to 60 K. All helium exhaust returns to the CHL for recompression. Of the 3.1 kW heatload on the CHL during normal operation of CEBA, half comes from

RF losses.

3.1.2   Injector

The beam originates as a continuous stream of electrons from a Tungsten filament in the thermionic gun of the injector. After passing through emittance defining apertures, a 1497 MHz RF chopper segments this DC beam into three bunches each 60 degrees of RF phase in length. Combinations of β-graded room temperature acceleration and drift, the bunching and capture sections, squeeze the bunchlengths to 0.5 degrees (1 ps) and stabilize the bunches into a phase space bucket prior to injection at 0.5 MeV into a 5 MeV quarter cryomodule preaccelerator. The beam can be diverted and examined at this point. Final acceleration to 45 MeV occurs in the final two cryomodules. A chicane merges the beam into the first linac.

3.1.3   Linacs and Arcs

There are two 400 MeV linacs, labelled geographically as North and South. Injection occurs at the West end of the North linac. The East arc consists of five separate beamlines, one for each pass of recirculation. The West arc requires only four beamlines, as extraction occurs at the West end of the South linac. Beyond the South linac, the Beam Switchyard diverts beam to the appropriate experimental hall.

There are twenty cryomodules per linac. A quadrupole accompanied by a bump

dipole and a beam position monitor follow every cryomodule. A system of septum magnets following each linac vertically separates the beams from each acceleration pass, with first pass beam bent most and fifth pass beam bent least, for transport through the arcs. A similar system preceeding each linac recombines the beams for the next acceleration pass. Quadrupoles in these sections match each beam to the linac and arc lattices for stable transport.

Proper phasing within the linacs is accomplished by adjusting the phase of the RF supply for each cavity to match the phase of the beam as prepared by the injector. Using beam position at locations of high dispersion within the arcs as an energy measurement, a cavity is correctly phased, or "crested," when the first pass beam energy is maximized.

The arcs transport beam isochronously, such that the pathlength is uncorrelated with initial position, angle, or energy variations, and achromatically, such that the final position and angles are uncorrelated with initial energy variations. The arcs consist of four superperiods of missing dipole FODO lattice, and are tuned to allow for an integer multiple of betatron oscillations. The phase space of the beam at the end of an arc thus matches its configuration at the entrance. As designed, the total arc length is a multiple of the RF wavelength to insure the beam arrives in phase with the RF at the next linac section. Should there be pathlength errors upon recirculation, each arc is equipped with a three magnet chicane, or "dog leg," for pathlength adjustment.

At the West end of the South linac, five RF separators extract beam at any pass for use in the experimental halls. These separators are room temperature RF cavities, operating at 499 MHz, which apply a transverse impulse to one of three 1497 MHz bunches and an oppositely directed impulse to the other two. The selected bunch passes the field side of a septum magnet and is routed through the Beam Switchyard to the appropriate experimental hall, while the other two continue into the arcs.

3.2   Hall C Beamline

The 499 MHz bunches prepared at the beam switchyard for Hall C traverse a 146.2 m achromatic beamline to the Hall C target, then 27 m more into the Hall C beam dump. The Hall C beamline contains both a fast and a slow raster system; under usual operating conditions, the fast raster spreads the beam over a 1×1 mm^2 square area on the target. The instrumentation along the beamline includes three beam current monitors, six wire scanning "Superharp" position and profile monitors, and several nondestructive antenna based beam position monitors. Figure 3.2 sketches the beamline and indicates the general locations of the instrumentation.

3.2.1   Beam Transport

The Hall C beamline [60] is subdivided functionally into a first match section, an arc, and a second match section, as indicated in Figure 3.2. The first match section
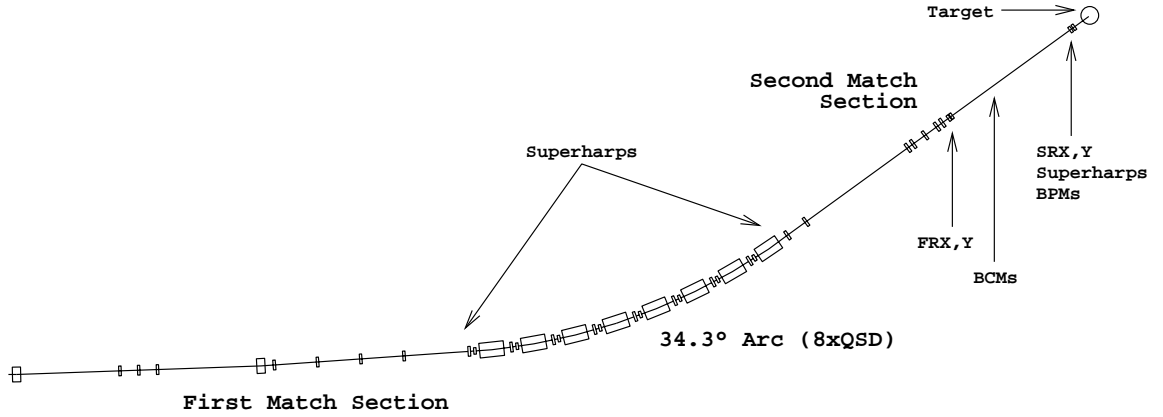
Figure 3.2: Hall C Beamline.

of the Hall C beamline accepts beam from the switchyard and prepares it with an achromatic waist at the entrance to the 40 m radius 34.3 degree arc achromat. This achromat is an eight unit FODO lattice, with each unit composed of a quadrupole, a sextupole, and a dipole. With only the dipoles energized, this arc also functions as a spectrometer with 12 cm/% dispersion for beam energy measurements. The arc returns the beam to an achromatic waist at the entrance of the second match section. This section uses a group of five quadrupoles to produce an achromatic focus in both transverse directions at the target position. The beam terminates in a beam dump located in an alcove at the rear of the experimental hall.

Located within the second match section, a fast raster system [61] distributes the energy density of the beam on the target to prevent heat damage. Two air core saddle shaped magnets, one for vertical deflections, one for horizontal deflections, are driven sinusoidally to produce a rectangular pattern on the target. Although the pattern preferentially populates the edges, it accomplishes the main task of safe beam power

distribution. A 520 W MOSFET amplifier fed with a 16.78 kHz horizontal signal and a 23.00 kHz vertical signal from a Wavetek function generator provides the current for the raster magnets. A similar system using 250 W audio amplifier and 60 Hz signals, the slow raster, is necessary when no target is present and the beam is delivered directly to the beam dump. Except during optics studies of the spectrometers, the fast raster was set for a 1×1 mm^2 scan on the target.

3.2.2 Position Monitors

The Superharp [62] makes a destructive but extremely precise measurement of the beam position and profile. The Superharp detects the signal generated in a 22 μm Tungsten wire as it moves through the beam. Survey error of approximately 100 μm contributes the largest amount to the uncertainty of the position measurement, while the limit of the profile measurement is largely given by the wire diameter. Because the beam is interrupted in the course of the measurement, separate runs are designated for Superharp operation. Three pairs of Superharps at the entrance, midpoint, and exit of the arc are used for arc optics studies and beam energy measurements. Another pair closer to the target are used to cross calibrate the beam position monitors (BPMs).

The nondestructive beam position monitors, illustrated in Figure 3.3, contain two orthogonal antenna pairs sensitive to the 499 MHz beam structure. The four thin quarter wavelength antennas are open circuited on the downstream end and oriented
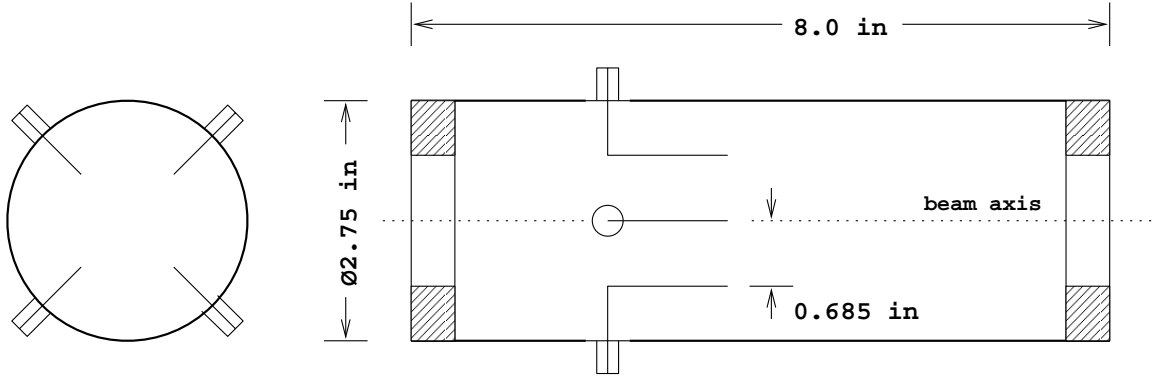
Figure 3.3: Beam Position Monitor.

at 45 degrees to the beamline coordinate system. The ratio of the voltage difference to the voltage sum from two antennas in the same plane is proportional to the deviation of the beam position from the axis [63]. The other antenna pair similarly determines the orthogonal deviation.

The signals picked up on the BPM antennas are down converted to 1 MHz and transported from the beam tunnel to a service building at ground level. The amplitude of the signal is detected and passed to CAMAC electronics for digitization and insertion into the EPICS database. A copy of the analog signal sent to the Hall C counting house is captured in a LeCroy FASTBUS ADC module and incorporated on an event by event basis into the data stream.

3.2.3   Current Monitors

Three devices measured beam current, two cavity monitors (BCMs) and one Unser monitor. All of these devices have cylindrical geometry aligned with the beam axis.

They are located in the third section of the Hall C beamline. The BCMs have extremely stable zero offsets and gains but require calibration; the Unser monitor has intrinsically poor zero offset drift, but it maintains absolute gain calibration over many months and is extremely linear. The cavity monitors are therefore used for the charge measurements once they are cross calibrated with the Unser monitor over time durations short enough to avoid problems with the zero drift.

To enter the data stream, a level shifter offsets the output voltage from the electronics instrumenting each monitor into the linear range of a voltage-to-frequency (V/F) converter. This device outputs a train of square pulses at a frequency proportional to the input voltage. These pulses are counted in a Lecroy VME Scaler module. The number of counts over a given time interval represents the average output voltage, up to an overall offset.

Cavity Monitors

Since the BCMs, like the BPMs, were originally designed for use in the accelerator, the cavity geometry of the BCMs is selected so that the fundamental harmonic in the transverse magnetic mode corresponds to 1497 MHz. The beam drives this resonance, therefore building up RF power proportional to the square of the beam current. A pick-up antenna couples out some of this stored power to provide an output signal. Low pass filtering on these signals selects the fundamental harmonic for further electronic processing. A Gigatronics 8542B power meter directly converts the power level
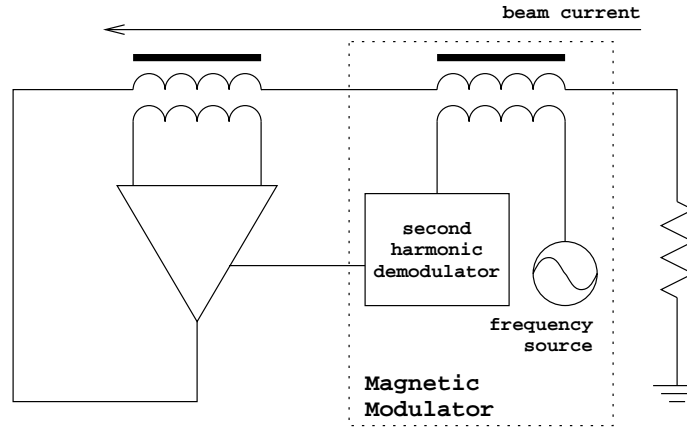
Figure 3.4: Sketch of the Unser monitor design.

from the first BCM into an output voltage. For the second BCM, a downconverter first mixes the signal with a local oscillator tuned to 100 kHz above the 1497 MHz operating frequency. An Analog Devices AD637 RMS-to-DC converter then transforms the amplitude of the beat signal into the final output voltage of the second BCM.

Unser Monitor

The Unser monitor [64, 65] is a zero flux current transformer. This device measures DC currents using a magnetic modulator and an active toroidal beam current transformer, as sketched in Figure 3.4. Without the magnetic modulator, the Unser is similar to an ordinary toroidal beam current monitor; when the secondary winding senses a change of flux, the amplifier draws current through the load resistance and maintains an image of the beam current in the primary winding. Although the operational amplifier reduces the low frequency cutoff by a factor of the gain, the magnetic modulator is essential to measure DC beam current.

The magnetic modulator consists of a fixed frequency source and a second toroid sharing the same primary winding as the first. The source drives the highly permeable core of the second toroid into saturation during each half cycle. The presence of a flux offset, indicating a mismatch of the primary current and the beam current, skews the duration of the saturation. The amplitude of the second harmonic is directly proportional to this asymmetry, and is used to bias the amplifier until the flux offset is eliminated.

3.3   Targets

The solid and cryogenic target systems are housed within a large scattering chamber. When fully evacuated this chamber opens directly to the beamline. The beam exits through a long snout sealed with a thin Titanium window mounted opposite to the entrance aperture. Thin Aluminum windows, only 0.41 mm thick, permit scattered particles to escape the chamber relatively undisturbed.

3.3.1   Solid Targets

The solid target ladder system mounts to a port in the top of the scattering chamber directly above the target position. An encoded linear motion mechanism permits accurate, repeatable placement of any of five targets at beam height. The target ladder may also be rotated to any angle about the vertical motion axis. Two carbon,

Target	Thickness [g/cm^2] ($\pm$1%)
Carbon	0.892
Carbon	2.510
Iron	0.213
Iron	0.803
Gold	0.377

Table 3.1: Solid target thicknesses.

two iron, and one gold target were used during this experiment. All were uniform, homogeneous samples with naturally occuring isotopic abundance. The thicknesses of each target are listed in Table 3.1. For visual checks of beam position, a beryllium oxide target was attatched to the bottom of the target ladder.

The beam heatload is an important concern for the solid targets. Particularly for the iron targets, proper cooling is necessary to avoid heat damage. Heat damage to a target includes melting, but any phase change, such as a transition in the lattice structure, can potentially alter the quantity of matter presented to the beam. The pyrolytic graphite (carbon) targets have not only very good thermal conductivity, but also a very high melting point. While gold melts at only 1337 K, its high thermal conductivity allows it to tolerate the beam currents used in this experiment.

Iron has the worst thermal conductivity, and suffers a body-centered cubic (BCC) to face-centered cubic (FCC) phase transition at 1185 K. Although well below its melting point of 1810 K, this phase transition can cause deformation of the target material since the unit cell in the FCC phase is smaller than in the BCC phase. To make matters worse, the thermal conductivity of iron [66] drops significantly with
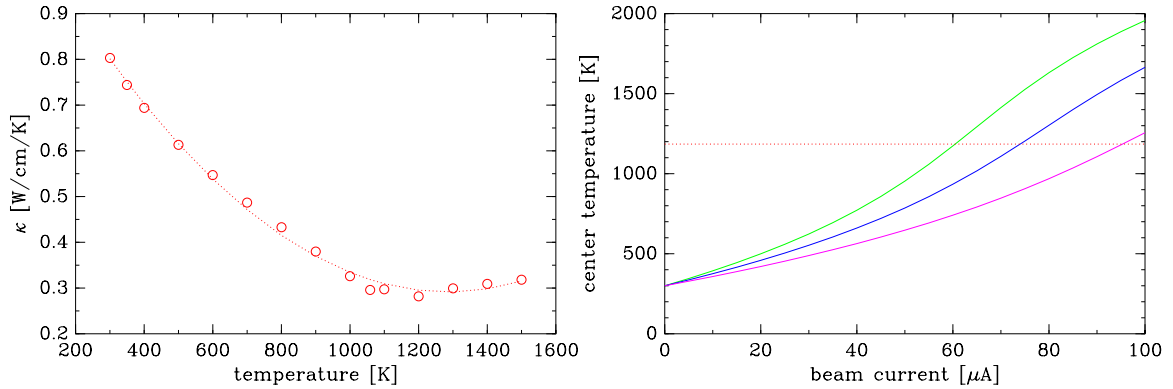
Figure 3.5: Iron thermal conductivity (left) and center target temperature as a function of beam current (right) for raster sizes of ±0.5 mm (green) ±1.0 mm (blue) and ±2.0 mm (magenta).

increasing temperature, as illustrated in the left panel of Figure 3.5. Appendix C describes a calculation of the target temperature including the nonlinearity introduced by the temperature dependence of the thermal conductivity. This calculation indicated that the iron targets could handle no more than approximately 70 μA for a 1×1 mm^2 raster, as shown in the right panel of Figure 3.5. In fact, significant target damage did occur when the current mistakenly exceeded this limit during the experiment.

The water cooling system for the solid target ladder is a closed loop consisting of a water reservoir, a pump, and a heat exchanger. Water pumped from the reservoir provides 2 gallons per minute water flow at 60 psi to the target ladder. A cooling loop plumbed through the body of the target ladder encourages heat flow out of all four sides of each target. The return line from the target ladder passes through the heat exchanger before dumping back into the reservoir. In order to maximize the heat flow

to the body of the target ladder, a layer of thermal contact grease was applied to the edges of the targets before they were clamped into their slots.

3.3.2   Cryogenic Targets

The cryogenic target system supported two liquid hydrogen targets, two liquid deuterium targets, and two dummy targets, one each of approximately 4 cm and 15 cm in length. The cryogenic target stack moves vertically to position any target at beam height; in addition, it rotates 90 degrees to the front quadrant of the scattering chamber to make room for the insertion of the solid target ladder into the beam.

Under normal operating conditions, the cryotargets were maintained at a pressure of 20 to 25 psia and at a temperature of 19 K for H_2 and 22 K for D_2. These conditions put the target liquids a few degrees below the liquid-vapor phase transition. In this state the target density is mostly a function of temperature, with very little pressure dependence. The empirical equations of state for these cryogens therefore lead to fluid densities of 0.0723 g/cm^3 for H_2, and 0.167 g/cm^3 for D_2, with a total uncertainty of approximately 0.5%. There was no measureable effect of beam heatload on target density [67]; additionally, an isotopic study [68] of the target gasses revealed that the H_2 targets were effectively 100% pure, while the D_2 targets contained 0.4% concentration of HD.

The cryogenic target system provides three target loops consisting of a target
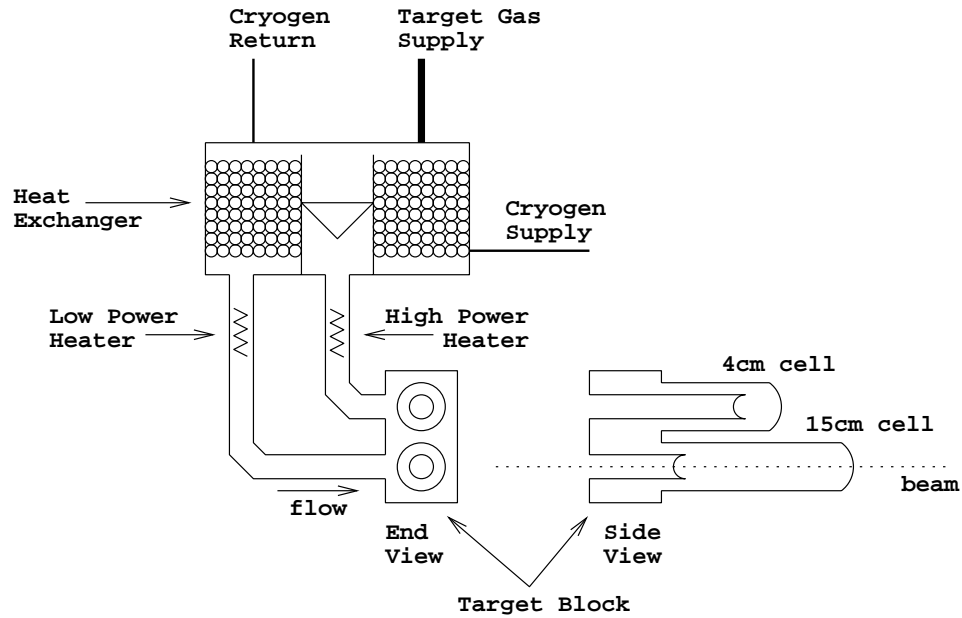
Figure 3.6: Sketch of a cryotarget loop.

block, a circulation fan, a heat exchanger, two heater coils, and a variety of ther-mometry instrumentation. A sketch of a target loop is displayed in Figure 3.6. The three target blocks are stacked vertically. Each target block houses one short target cell and one long target cell. The target cells are 6.73 cm diameter cylinders with 0.013±0.005 cm thick walls, and are wrapped with a thin blanket of superinsulation. The dummy targets are made of the same material as the entrance and exit windows of the target cells, aluminum type 5052 and 3004 respectively, but are more than ten times thicker.

A 60 Hz "Archimedes screw" fan in each target loop circulates the target liquid across a heat exchanger to remove the beam heatload. The heat exchanger is simply a coil of fin tubing; a coolant, liquid helium, flows inside the tubing, while the target

liquid passes over the tubing exterior. The fins on the tubing increase the surface area to aid the transfer of heat from the target liquid to the coolant. Joule-Thompson valves, one for the total helium flow to all target loops and two to bypass the first and third target loops, allow a fair amount of regulation of the cooling power. The design can accommodate up to 300 W of heatload. The heater coils within the target loop permit the target to be powered prior to accepting beam, and replace the beam heatload in the event of beam interruptions. A 65 W low power heater compensates for small beam current fluctuations, and a 300 W high power heater matches the majority of the beam power.

Four Lakeshore Cernox resistors provide the best temperature measurements of the target fluid. These are located above and below the fan, and before and after the low power heater. An Oxford Instruments ITC-502, one for each target loop, measures the four resistances and converts them to temperatures based on a calibration table. This device can be operated in a feedback loop with the low power heater to maintain a constant target temperature. Various other temperature and pressure instrumentation monitors the state of the cryotarget system for safe operation.

3.4   Spectrometer

The High Momentum Spectrometer (HMS) consists of a set of superconducting magnetic elements, three quadrupoles and a 25 degree vertical bending dipole, and a group
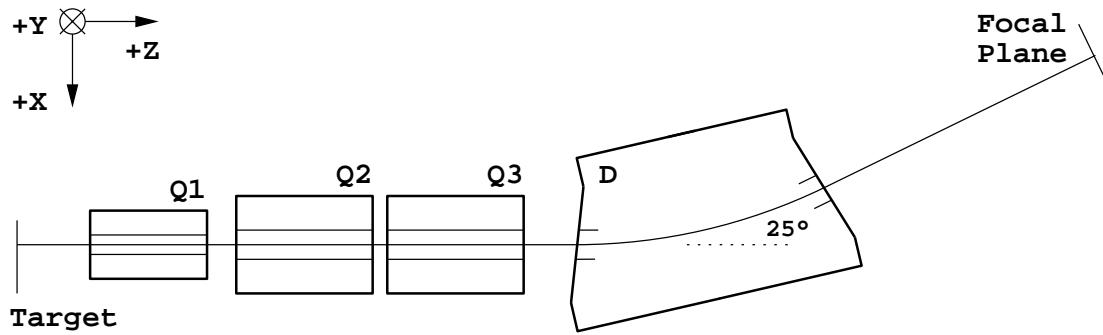
Figure 3.7: HMS magnetic elements.

of particle detectors comprised of a pair of drift chambers, four hodoscope planes, a

Čerenkov detector, and a calorimeter. The magnetic optics transport charged parti-

cles more than 23 m from a small volume of phase space at the target to the group

of detectors; the accepted particles are focused transversely and dispersed vertically

by momentum. The detectors are housed inside a shielded enclosure constructed of

high density concrete more than three feet thick and lined with lead on the interior

surfaces. This detector hut and the magnetic elements are mounted on a massive steel

carriage which can be rotated on a pair of concentric rails to any angle between 12.5

degrees and 80 degrees relative to the beam axis with an accuracy of ± 0.01 degrees.

Figure 3.7 illustrates the arrangement of the magnetic elements of the HMS. The

quadrupoles are tuned to alternately focus, defocus, and focus in the vertical plane

to maximize the azimuthal acceptance. This tuning is also intended to produce

a point to point focus at the focal plane. An octagonal aperture at the entrance

of the first quadrupole, approximately 128 cm from the object plane, defines the

solid angle for point targets to be 6.8 msr and allows maximum vertical angles of
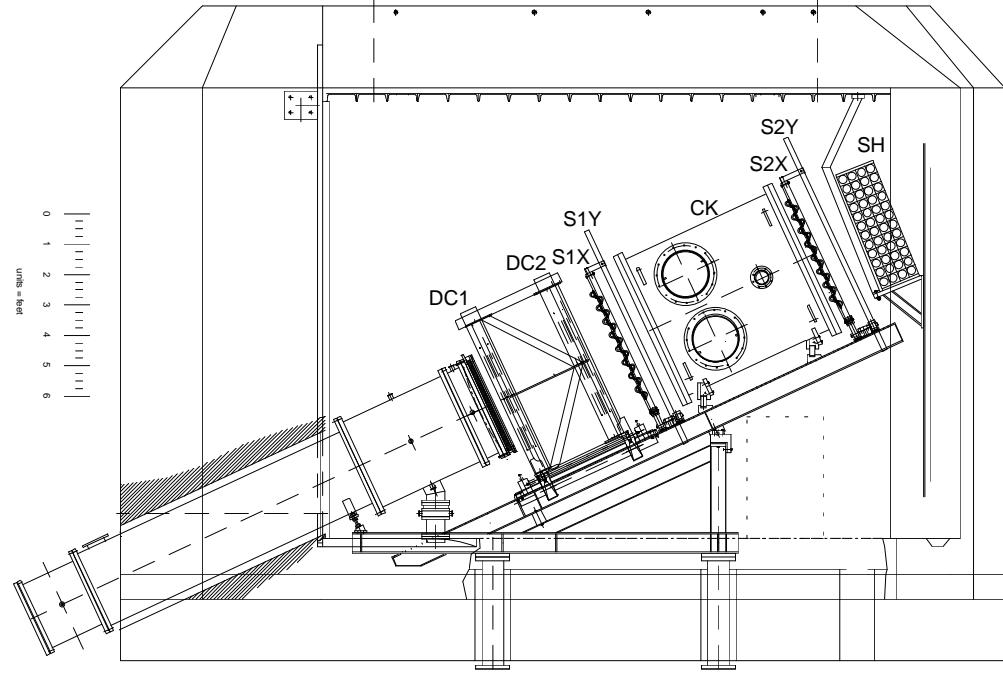
Figure 3.8: HMS detector package within the detector hut.

± 70.5 mrad and maximum horizontal angles of ± 27.7 mrad. Other apertures and the finite extent of the detectors begin to diminish the solid angle and limit the momentum acceptance beyond approximately $\pm 10\%$. The extended target acceptance is limited to approximately ± 5 cm in the object plane.

The arrangement of detectors is indicated in Figure 3.8. Straddling the focal plane, the drift chambers measure particle trajectories with position and angle resolution of approximately ± 0.3 mm and ± 0.3 mrad over an active area of approximately 110×50 cm^2. The hodoscopes establish a time marker for each event, accurate to better than 0.5 ns, used to measure time intervals such as the drift times in the drift

chambers. Sequential firing of the hodoscope planes also provides a simple indicator for the passage of a particle used in the trigger. The Čerenkov and calorimeter discriminate electrons from pions and other more massive particles; together they misidentify only one in every few thousand pions as an electron.

The signal cables for all detectors except the drift chambers run several hundred feet up to the Hall C Counting House where they are split. One copy of these analog signals is immediately discriminated and duplicated. An array of NIM and CAMAC fast logic operates on one set of these discriminated signals to form the trigger indicating a valid event. Another set are digitally delayed several hundred nanoseconds and timed relative to the trigger in LeCroy FASTBUS 1872A TDC modules. The other copy of the analog signals is cable delayed and then charge integrated in LeCroy FASTBUS 1881M ADC modules. A copy of the trigger sent back down to the detector hut provides the common stop for a bank of twelve LeCroy FASTBUS 1877 TDC modules which measure the drift chamber signals.

Throughout the following subsections, the moving coordinate system defined along the central trajectory of the spectrometer is used. The positive X direction is down, positive Y is left, and the Z direction follows the central ray from the target to the detectors. Surveys established the positions of the magnets and detectors to approximately 0.5 mm.

3.4.1 Magnetic Optics

All three quadrupoles, fabricated by Oxford Instruments, have hyperbolic laminated iron poles wound with planar superconducting coils. The second and third quadrupoles are identical. The cryostat containing the coils, poles, and return yoke for Q2 and Q3 is cylindrical with a length of 2.808 m; the pole tip radius is 0.35 m and the radius of the cryostat aperture is 0.298 m. The cryostat for Q1 is squeezed horizontally, displacing most of the return yoke vertically, to accommodate the 12.5 degree forward angle of the HMS. Its length is 2.438 m, its aperture radius is 0.203 m, and its pole tip radius is 0.25 m.

The dipole, manufactured by ELIN, also has superconducting coils. Unlike the quadrupoles, however, the iron poles are external to the cryostat. The pole gap width is 42 cm, the radius of curvature is 12.056 m, and the bend angle is 25 degrees. The poles are not indexed, but the entrance and exit pole faces are both rotated six degrees to produce a small amount of vertical focusing.

Rotating coil measurements determined the pole tip field, integral field strength, and multipole content of the quadrupoles as a function of applied current [69]. Away from hysteresis and saturation effects, the observed magnetic properties vary linearly with current over a range of approximately 200–800 A for Q1 and 150–500 A for Q2 and Q3. In these regions, the pole tip fields and effective lengths are 12.810 G/A and 1.878 m for Q1, 24.448 G/A and 2.157 m for Q2, and 24.535 G/A and 2.157 m for

Q3. For the dipole, NMR measurements [70] verified the uniformity of the field to better than 1×10^{-3} across the pole gap. However, no detailed field map was made for any of these magnets.

Initial models [71, 60] of the HMS used effective lengths and Enge parameterizations of the fringe fields from TOSCA calculations based upon the design specifications [72] for these magnets. Using the standard second order optics tools, such as RAYTRACE and TRANSPORT, the pole tip fields in the model were optimized to achieve a point to point tune. This determines a calibration of central momentum setting to pole tip field, which is transferred onto the field setting procedure for the real quadrupoles through a linear fit to the rotating coil measurements. No such transfer is necessary for the dipole since its field strength is regulated directly through NMR.

Figure 3.9 illustrates the optics of the HMS as calculated in sixth order using COSY [73, 74] and the effective lengths and pole tip fields from the rotating coil measurements set according to procedure described above. The top two drawings show views in the xz and yz planes, respectively, for rays from a point target with vertical angles ± 71 mrad and horizontal angles ± 28 mrad, and with momentum fractions of -8% (red), -4% (yellow), 0% (green), +4% (blue), and +8% (magenta). The bottom drawing indicates a yz view of rays at the central momentum with horizontal angles of ± 28 mrad originating from extended target positions of -5 cm (red), -2.5 cm (yellow), 0 cm (green), +2.5 cm (blue), and +5 cm (magenta).

Higher orders are necessary because of both the wide acceptance as well as the
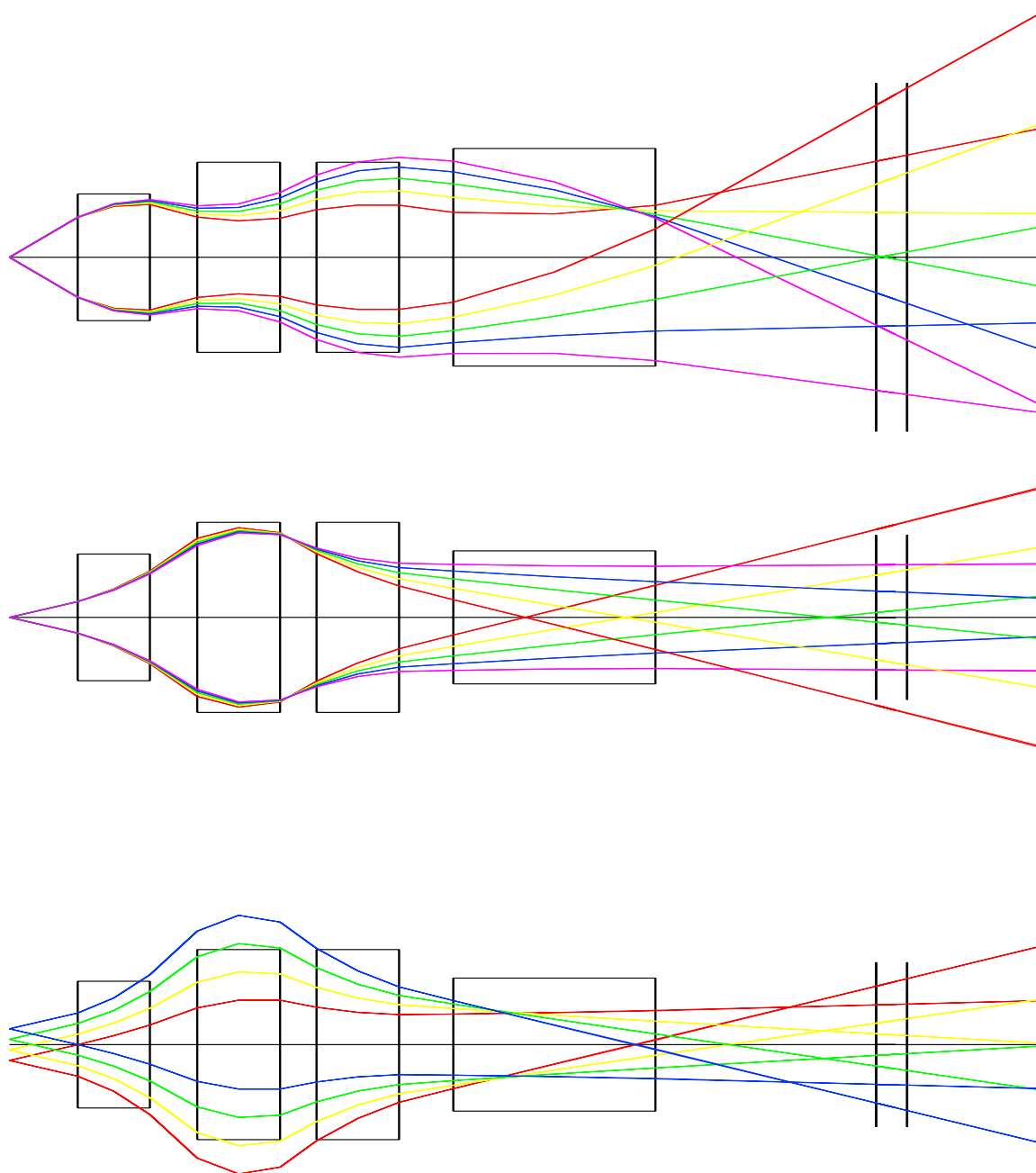
Figure 3.9: Raytrace of the HMS optics. See the text for details.

large ratios of pole tip radius to the pole length for the quadrupoles. These effects and the extreme 85 degree tilt of the second order focal plane also accentuate the importance of the fringe fields in the focusing properties of the optics; since no field map was done, these fringe fields are unknown except through the TOSCA simulations. In fact, all of these factors conspire to blur the point to point focus of the second order model into a focal volume which is relatively narrow for small angle and momentum deviations and becomes wider, curved, and more diffuse for rays with larger deviations.

3.4.2 Drift Chambers

Two drift chambers [75], spaced approximately 80 cm apart, measure the track of a particle as it traverses the detector hut. Each chamber contains six planes of high voltage and sense wires arranged to collect and amplify the ionization produced by the passing particle across an active area of approximately 110×50 cm^2. As indicated on the far right of Figure 3.10, the high voltage wires of a plane form a rectangular lattice, with a wire at each of the four corners and at the four face centers. A sense wire runs along the body center of each lattice cell. The cell size of the HMS drift chambers is 1.0×0.8 cm^2, and the total spacing between sense wires of neighboring planes is 1.8 cm.

The high voltage wires are 150 μm diameter copper beryllium; the sense wires are
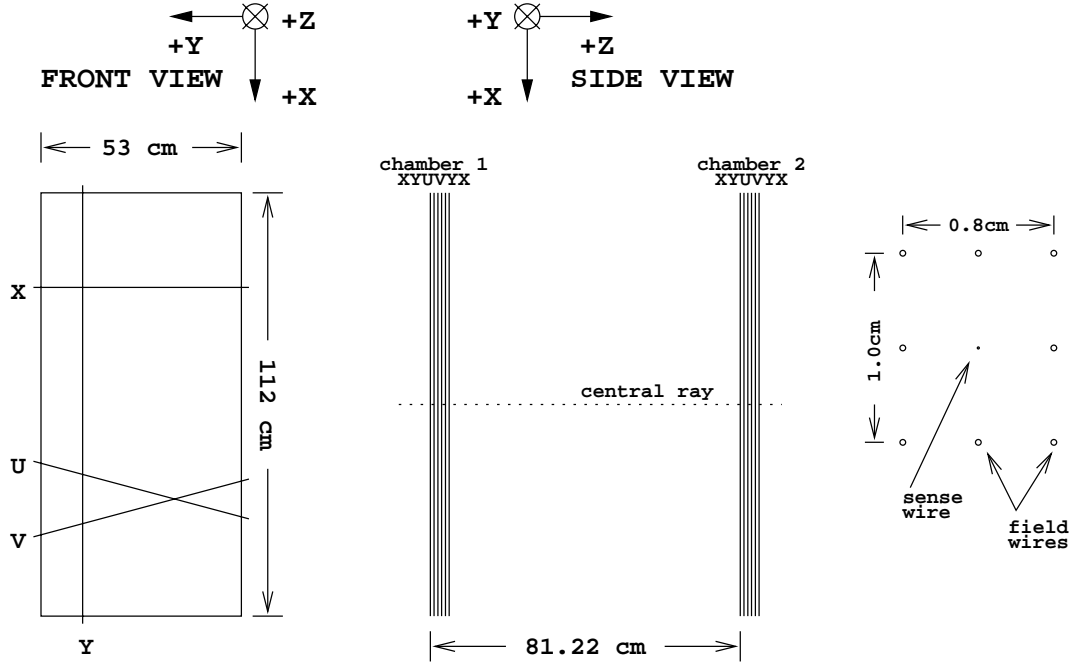
Figure 3.10: Drift chamber geometry. The drawing on the left indicates the direction of four representative wires. The cell geometry is indicated on the right.

25 μm tungsten. Both types of wires are gold plated. The diameters ideally are as small as possible to generate large electric field gradients and quickly rising signals, as well as to minimize multiple scattering events, yet are thick enough to support the tension necessary to overcome the electrostatic forces tending to bow the wires.

Each plane measures a single coordinate orthogonal to the wire direction. There are four orientations of the HMS drift chamber planes, labeled by the measured coordinate: horizontal (X), vertical (Y), and ± 15 degrees to horizontal (U and V). The plane orientations running from front to back in a chamber are X, Y, U, V, Y, X. The duplicate orientations are offset one half cell from one another. Respectively, the horizontal, vertical, and stereo planes (U and V) each have 113, 52, and 107 wires.

Electrons and negative ions from the ionization of a passing particle move in the electric field of the drift cell to the grounded sense wire. The rapid intensification of the electric field near the sense wire accelerates this charge cloud. The electrons of the primary ionization gain sufficient energy to begin creating new ion-pairs; this process exponentiates leading to an avalanche of charge at the sense wire. This charge multiplication is necessary to amplify the ionization signal to detectable levels. With the gas mixture, cell geometry, and operating voltages selected so that the drift velocity of the ionization is constant throughout most of the cell volume, the arrival time of the charge is proportional to the distance from the sense wire at which the ionization occured.

Utilizing this principle, the HMS drift chambers can measure drift distances with a resolution of approximately 300 μm. Ideally, a particle produces a signal in sense wires from all twelve planes. Each drift time is converted into a drift distance which is added to the surveyed location of the sense wire; these measurements are fit to a trajectory parameterized by the intersection x, y with the focal plane ($z = 0$) and by the slopes x', y' projected in the xz and yz planes.

The HMS chambers are filled to just above 1 atmosphere with an equal weight mixture of argon and ethane bubbled through isopropyl alcohol chilled to 0 degrees Celsius. Argon is an effective multiplier at relatively low electric field intensities, but excited argon atoms radiate many high energy photons which can induce continuous discharge. Ethane suppresses this effect [76] by absorbing and thermally dissipating

the radiation, thus permitting operation at higher amplification. The recombination of ionized ethane fragments at the high voltage wires, however, produces a polymer accumulation which degrades the chamber performance with time. The small amount of alcohol bubbled into the mixture changes the chemistry enough to retard the polymer buildup.

Each sense wire signal is sent through a 30 ns differentiator, an amplifier, and finally a discriminator to produce suitable start pulses for the timers in the FAST-BUS 1877 TDC modules. This is done with 72 LeCroy 2735DC 16 channel signal processing cards mounted directly on the chambers; some of these cards are actually manufactured by Nanometrics but are electronically equivalent. The discriminator thresholds can be remotely adjusted from the Counting House. Each TDC module is configured for leading edge timing, common stop operation with a 3 μs full scale time window, and a multiple hit FIFO depth of 3.

3.4.3   Hodoscopes

The hodoscopes establish a reference time for each event, accurate to better than 0.5 ns, used to determine time intervals such as the drift times in the drift chambers. In addition, they are an essential part of the trigger for valid events. The four hodoscope planes are organized into X-Y pairs, one pair preceeding and one pair following the Čerenkov detector. Each plane is a collection of BC-404 plastic scintillator
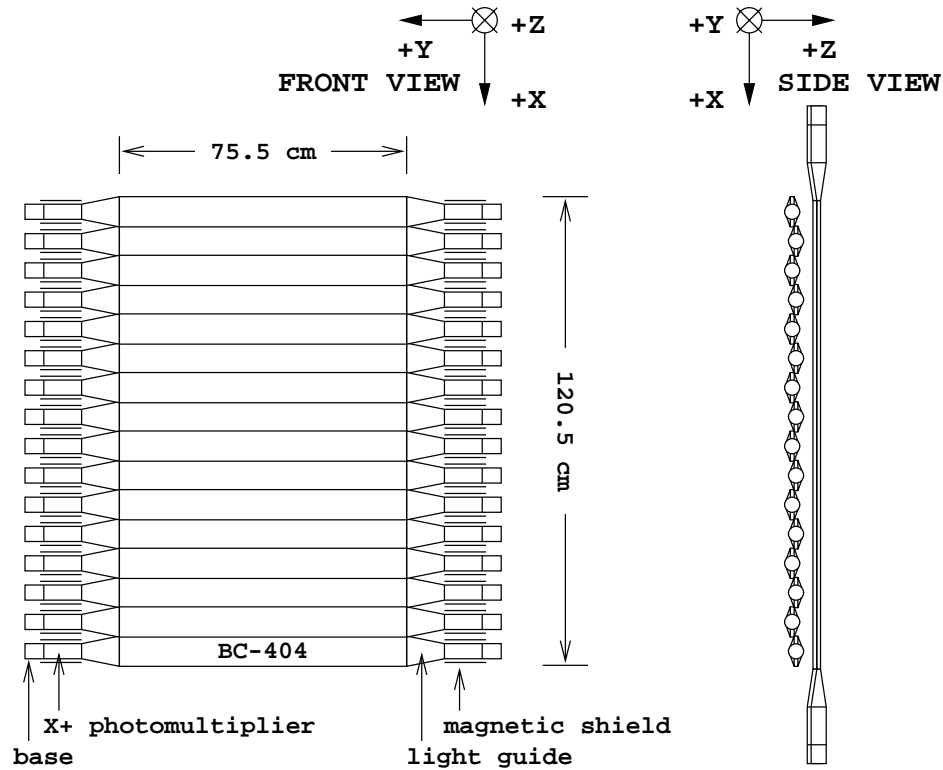
Figure 3.11: Hodoscope geometry for an X plane (left) and an X-Y pair (right).

elements. The X-planes consist of 16 horizontal elements 75.5 cm long; the Y-planes consist of 10 vertical elements 120.5 cm long. All elements are 8 cm wide and 1 cm thick. A 0.25 cm staggered overlap of adjacent elements prevents holes in the active area of each plane. Figure 3.11 illustrates this geometry.

Both ends of every hodoscope element have a lucite lightguide leading to a Philips XP2282B photomultiplier tube housed within a magnetic shield. Aluminum foil followed by one layer of tedlar forms a reflecting, light-tight wrap around the whole assembly. The BC-404 scintillator material is a polymer of an alkyl benzene. It has a low 1.032 g/cm^3 density and a 1.58 index of refraction. The spectrum of photons

emitted after the passage of a charged particle through BC-404 peaks at 434 nm and is characterized by a 1.8 ns exponential decay. The ultraviolet response and index of refraction of the lightguide is matched to the scintillator material to minimize signal attenuation. The element geometry prevents the majority of the light emission from following a straight path to the phototubes; in fact, most of the light suffers many internal reflections. This reduces the signal velocity from the value given by the dispersion of the medium, $c/n \approx 19$ cm/ns, to approximately 14 cm/ns.

All of the signals from phototubes on the same side of a plane are grouped together; a $+$ or $-$ designates the left or right (bottom or top) phototubes of an X (Y) plane. The phototubes within each group are gain matched, and their signals are discriminated with the same threshold level in a bank of Philips PS7106 16 channel leading edge discriminators. Two LeCroy 4564 OR Logic Units process these eight groups of discriminated signals to produce the logic signals required for the trigger, as indicated in Figure 3.12 for the first X-Y pair of planes.

The four output logic signals S1X, S1Y, S2X, and S2Y indicate which of the hodoscope planes are active. As defined with this logic, an active plane requires that at least one of its $+$ signals was above threshold AND at least one of its $-$ signals was above threshold. Furthermore, the signals S1 and S2 indicate whether the pairs are active; an active pair is defined as having at least one active plane. The trigger makes use of the STOF and SCIN logical signals. Of the two, SCIN is more stringent, requiring that at least three of the four planes are active. STOF requires only that at
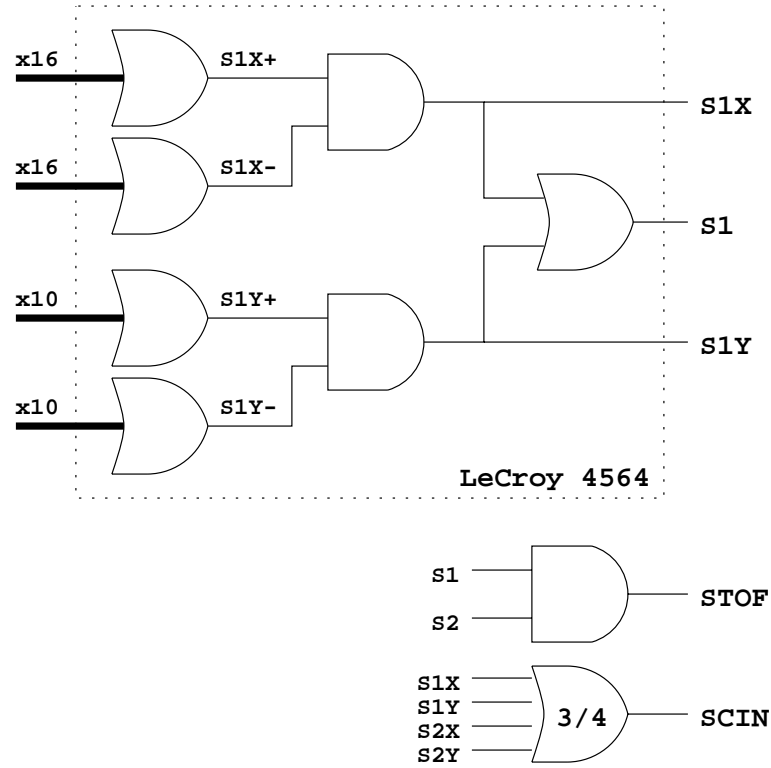
Figure 3.12: Hodoscope logic.

least one plane is active in each pair.

3.4.4 Čerenkov Detector

The Čerenkov detector distinguishes electrons from other particles. The University of Virginia constructed this device. As illustrated in Figure 3.13, it is a 1.5 m long by 1.5 m diameter cylindrical tank. A pair of front reflecting spherical mirrors mounted vertically with 1 cm overlap at the rear of the detector are rotated 15 degrees to focus onto a pair of Burle 8854 5 inch photomultiplier tubes. Each mirror is a 0.3 cm thick, 65×60 cm^2 glass pane slump molded into a 163 cm radius of curvature, and has a

vacuum deposited aluminum layer with a protective coating of MgF_2. Hydroformed windows only 40 mil thick seal the ends of the tank. From vacuum, the detector is filled with 0.4 atm of C_4F_{10} at room temperature. This sets the index of refraction of the gas to be $n = 1.00061$.

The electromagnetic response of the gas to a charged particle cannot propagate faster than c/n. When a particle travelling through the gas exceeds this speed, part of the electromagnetic field radiates away as a conical wavefront of visible light along its direction of motion. This is known as Čerenkov radiation. The operating conditions of the Čerenkov detector are selected so that a pion needs a momentum of at least 4.1 GeV/c to exceed c/n. Therefore, over the momentum range of interest to this experiment, no pion can produce a signal in the Čerenkov detector. Electrons, on the other hand, need only 0.015 GeV/c to radiate, so a signal in the Čerenkov detector identifies electron events.

The amount of Čerenkov light produced is small and fluctuates from event to event. Inefficiency in the conversion to photoelectrons further diminishes the observable signal and amplifies the statistical fluctuations. Since the signal must exceed a modest threshold to be distinguishable from noise, it is important to produce the largest possible average photoelectron yield. One of the steps taken to accomplish this was the use of a custom designed phototube base which applied 1 kV between the photocathode and first dynode to increase the photoelectron collection efficiency [77]. Another was to improve the sensitivity of the detector to the ultraviolet part of the

FRONT VIEW

+Z

+Y

+X

TOP VIEW

+Y

+Z

+X

150 cm

hydroformed
windows

rohacell

mirror

30° 15°

phototube

magnetic
shield

base

150 cm

BNC   HV
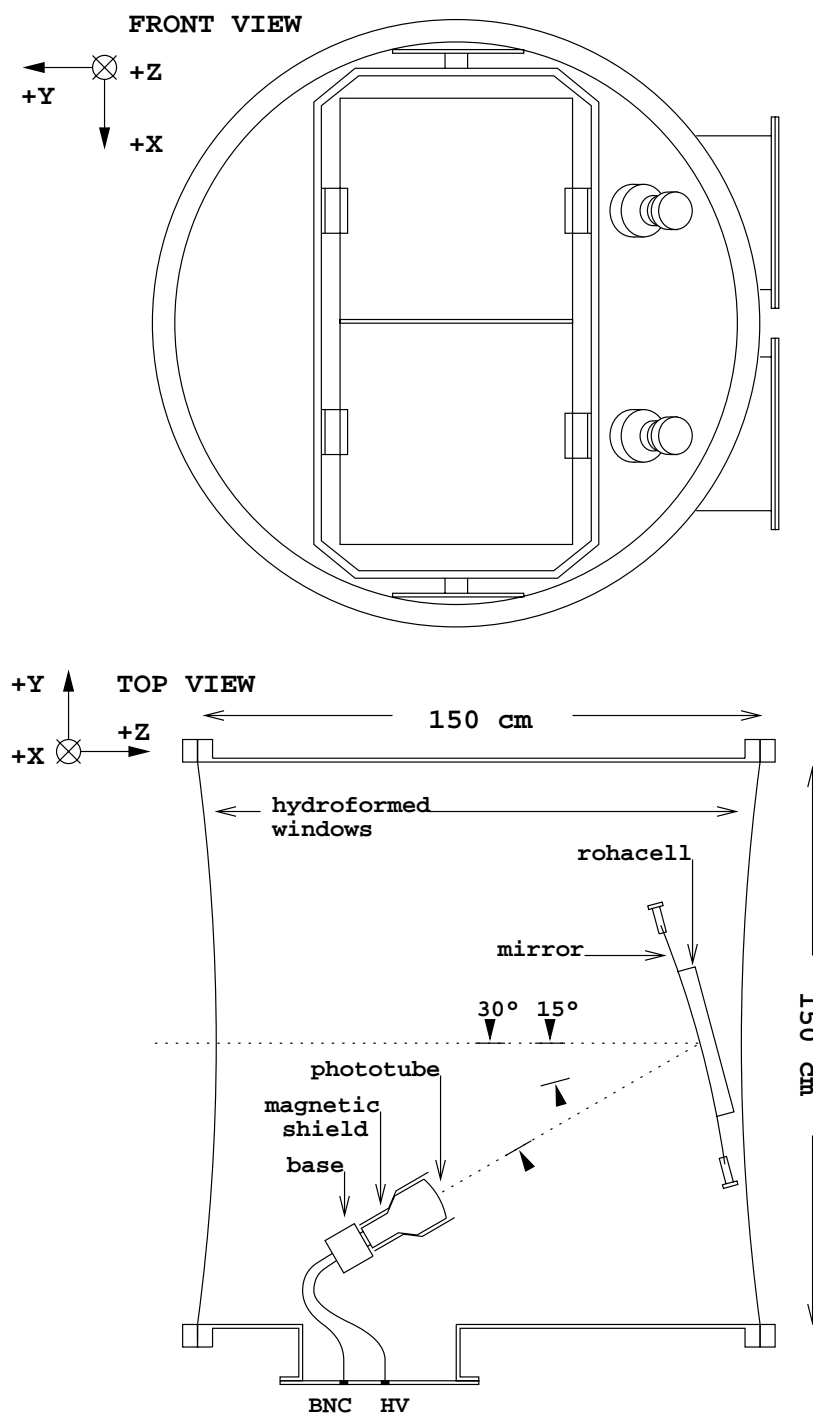
Figure 3.13: Čerenkov detector geometry.
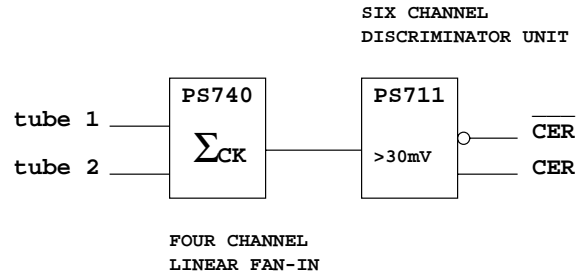
Figure 3.14: Čerenkov logic.

Čerenkov spectrum.

Since the $1/\lambda^2$ dependence of the Čerenkov spectrum heavily weights short wavelengths, the total photoelectron yield is largely constrained by the ultraviolet properties of the gas and optical components. Pure C_4F_{10} is known to be transparent [78] down to at least 160 nm; UV absorbing contaminants, such as water vapor and O_2, were diluted to negligible levels by repeatedly flushing the tank with dry N_2 prior to filling. Since the reflectance of the mirrors is approximately 87% from 250 nm to 180 nm, dropping modestly to 79% at 150 nm, the phototube entrance windows, which are opaque below 200 nm, pose the greatest limitation to UV sensitivity. To overcome this deficiency [79], a 2430 nm layer of the wavelength shifting material para-Terphenyl protected by 25 nm of MgF_2 was deposited onto the phototube entrance windows. This thickness of para-Terphenyl converts all light at wavelengths below approximately 320 nm into a fluorescence at 360 nm where the phototube entrance window is transparent.

To create the logic signals necessary for the trigger, the signals from the two

phototubes are summed and discriminated with a threshold set approximately at the one photoelectron level. This is illustrated in Figure 3.14.

3.4.5 Calorimeter

The calorimeter [80] is also used to select electron events. As indicated in Figure 3.15, it consists of a 4×13 array of TF-1 lead glass blocks at the rear of the detector hut. Each $10 \times 10 \times 70$ cm^3 block is wrapped with aluminum foil and an outer layer of mylar, and has a Philips XP3462B photomultiplier tube with a magnetic shield mounted on one end. The TF-1 lead glass contains 41.3% SiO_2, 51.2% PbO, 7% Na_2O, and 0.5% As_2O_3 by weight. Its density is 3.86 g/cm^3 and its index of refraction is 1.65. The radiation length of TF-1 is 2.5 cm.

The heavy nuclei in the lead glass encourage an electron entering the calorimeter to lose energy by radiating a high energy photon (bremsstrahlung). The primary electron can continue to lose energy this way, and the photons produced can undergo a closely related process which converts them into electron-positron pairs. The calorimeter therefore distributes the energy of the initial electron among more and more photons, electrons, and positrons. This electromagnetic shower stops when the produced particles no longer have enough energy to radiate and ionization becomes the dominant energy loss mechanism.

The calorimeter is designed so that the energy deposition of the shower peaks
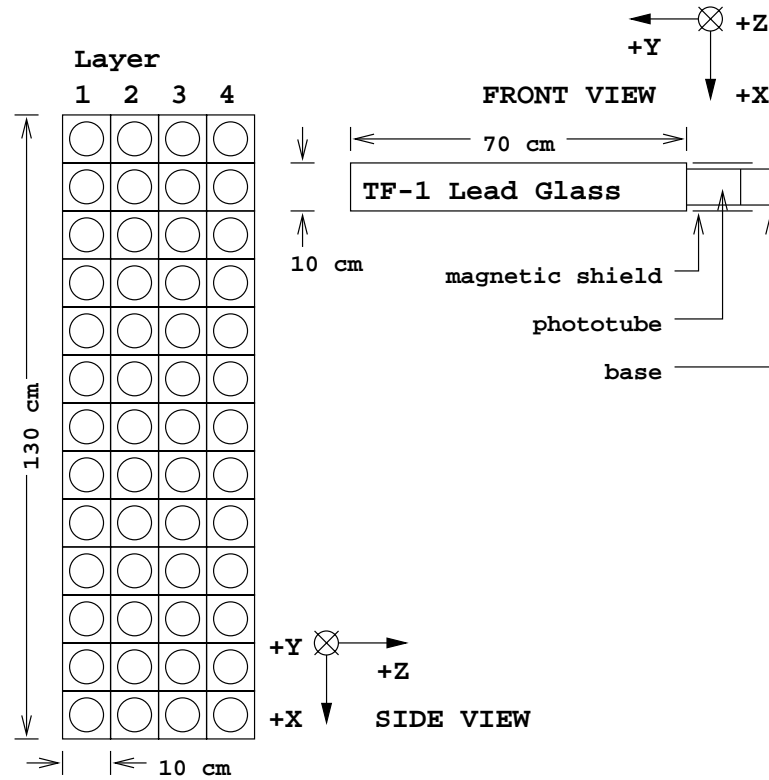
Figure 3.15: Calorimeter geometry.

within the first two blocks, and for all practical purposes the entire energy of the initial electron is absorbed within all four layers of the detector. Because the processes involved are peaked in the forward direction, the transverse development of the shower, characterized [81, 76] by the Molière radius, is almost entirely contained within a 4 cm radius. Consequently, the shower from a single event is contained (conservatively) within at most a 4×3 block volume.

The phototubes detect mainly the Čerenkov light produced by the electrons and positrons in the shower. When these signals are suitably normalized and summed, the total response of the calorimeter is proportional to the energy of the initial electron.
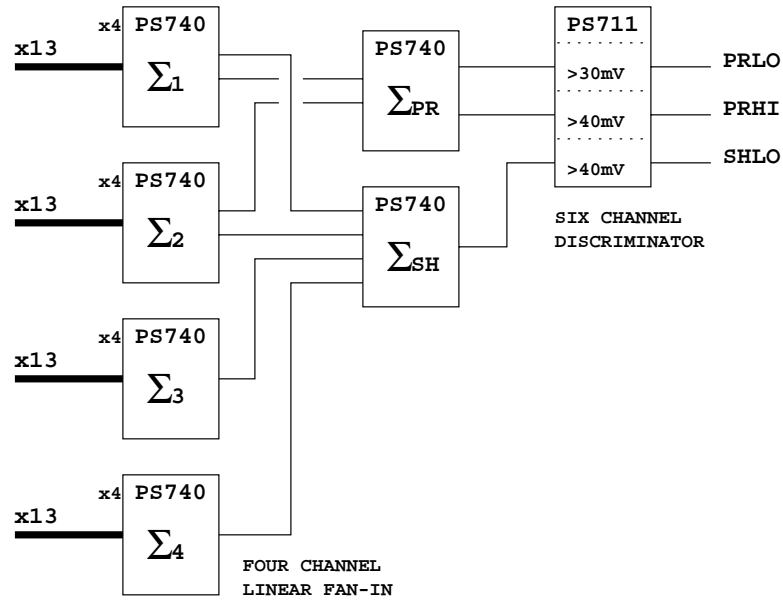
Figure 3.16: Calorimeter logic.

Because of their mass, it is very unlikely for a pion to initiate an electromagnetic shower. The calorimeter therefore serves as another means of separating electron events from pion events. Although infrequent, pions can, unfortunately, leave a significant amount of energy in the calorimeter if they experience a nuclear reaction within the lead glass. In combination, however, the calorimeter and the Čerenkov detector define a very clean sample of electrons.

Figure 3.16 sketches the electronics used to form the calorimeter logic signals used in the trigger. The sum of the signals from the first two layers, the preradiator, is discriminated at two thresholds to generate two logic signals, PRLO and PRHI. The preradiator is distinguished because most of the energy deposition for electrons is contained in the first two layers, while any large deposition from pions tends to be
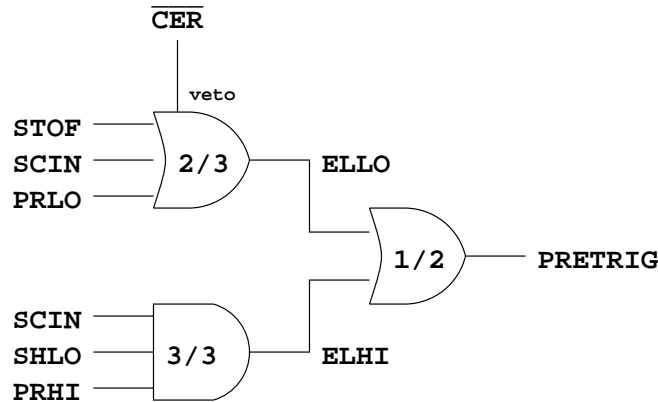
Figure 3.17: Electron trigger.

contained in the back layers. The sum of all 52 signals is discriminated at a single threshold to produce `SHLO`.

3.4.6   Trigger Logic

Using the logic signals described in the previous sections, the trigger is responsible for recognizing in real time the passage of a particle through the detectors of the HMS. The implementation indicated in Figure 3.17 is based on a design often used at SLAC. It is extremely efficient ($> 99.9\%$) for identifying energetic electron events, while being relatively inefficient ($\approx 4\%$) for pions. Unless it is busy, the data acquisition system will respond to a `PRETRIG` by initiating the digitization and storage of the response of the detectors. Copies of all of the logic signals are counted in scaler modules.

The `SCIN` logic signal from the hodoscope is the backbone of the trigger logic. This signal indicates that at least three of the four hodoscope planes were hit, which nearly always is the case for an energetic particle transported through the spectrometer from

the target. The `STOF` signal in the `ELLO` branch of the trigger is therefore ordinarily redundant with the `SCIN` requirement. Consequently, the primary difference between the `ELLO` and `ELHI` branches resides in the particle identification requirement. The `ELHI` is clearly determined by the calorimeter. Under ordinary circumstances, the `STOF` and `SCIN` redundancy makes `PRLO` irrelevant in the 2/3 OR, so that `ELLO` is mostly determined by the Čerenkov detector. These conditions are easily summarized as:

$$
\begin{aligned}
\texttt{PRETRIG} \quad = \quad & \texttt{ELLO} + \texttt{ELHI} \\
\simeq \quad & \texttt{SCIN} \cdot (\texttt{PRHI} \cdot \texttt{SHLO} + \texttt{CER})
\end{aligned}
$$

Since pions usually deposit more of their energy deeper within the calorimeter, the requirement of a high preradiator signal in addition to a minimal total shower energy suppresses the number of pions accepted. Events which latch the trigger are therefore those for which the hodoscopes registered a passing particle *and one or both* of the particle identification detectors showed a minimal response.

The apparent complexity in the `ELLO` branch is intended to handle the more unusual circumstances when the `SCIN` fails to respond to otherwise interesting events. Such a circumstance could arise from a hole in the response of the hodoscopes, for instance, from a dead tube in a front plane and a dead tube in a rear plane. The `STOF` signal would still fire, therefore allowing a trigger provided *both* the Čerenkov

fired *and* the preradiator was above a low threshold.

This trigger design was modified for a variety of special circumstances during the experiment. By simply removing the negated Čerenkov veto from `ELLO`, the trigger is effectively determined by `SCIN` alone; this was done to study the effect of the particle identification requirements on the data sample. Alternately, the more stringent requirement of *both* Čerenkov and calorimeter is accomplished by changing `PRETRIG` from a 1/2 to a 2/2 requirement on `ELLO` and `ELHI`; this greatly increases the pion rejection of the trigger.

3.5 Data Acquisition

The data acquisition system [82] manages the conversion, digitization, and storage of a sample of events identified by the trigger logic. It is composed of the ADC and TDC front-end modules, a distributed computer network, and the Trigger Supervisor. The Trigger Supervisor, a VME module custom designed at TJNAF, is the gateway to the data acquisition system; it regulates the rate at which pretriggers initiate an acquisition cycle according to the status of the front-end electronics and the computer network. Components of the CEBAF Online Data Acquisition (CODA) software (version 1.4) run on each node of the computer network to coordinate the data transfer from the front-end modules to storage on disk.

Figure 3.18 illustrates the data acquisition system. For simplicity, the components
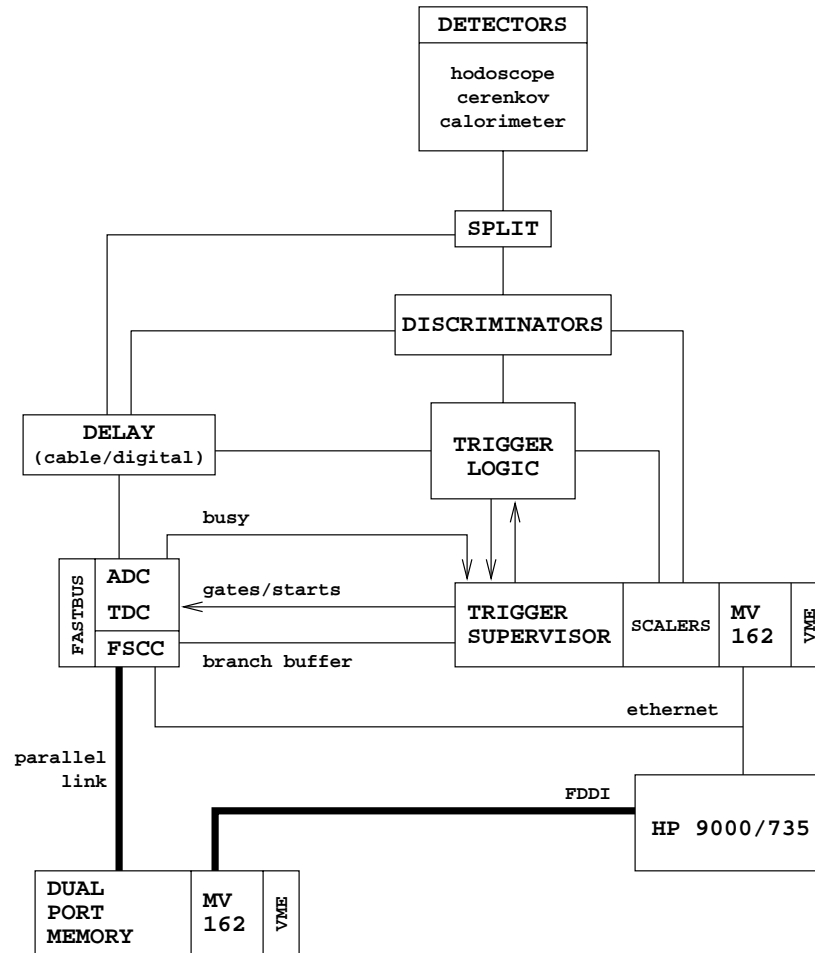
Figure 3.18: Sketch of the data acquisition system.

for the acquisition of the drift chamber data are omitted. The ADC and TDC modules
are installed in FASTBUS crates, each of which contains a FASTBUS Smart Crate
Controller (FSCC). The FSCC is a diskless, single board computer with a Motorola
68020 CPU, 2 MB RAM, a 32-bit ECL parallel port, and an ethernet interface. The
VME crates have a similar controller, the MV162, which has in addition a FDDI
interface. Both of these computers run the VxWorks operating system which they
download via ethernet from the HP 9000/735 host computer at startup. The 125 MHz

HP 9000/735 runs the HP-UX operating system and has 24 GB of hard disk storage.

There are two main data acquisition modes, either buffered or unbuffered, and two transport paths, either ethernet or FDDI. The front-end modules contain a memory buffer capable of storing the results of up to eight acquisition cycles. In buffered mode, these modules do not have to wait for the FSCC to readout their data; instead, once digitization is complete they are re-enabled for acquisition. Buffered operation therefore significantly improves the live time of the DAQ.

Of the two transport paths, the FDDI is fastest. At 100 Mbit/s, the FDDI network has ten times the bandwidth of ethernet, although both are limited in practical circumstances to approximately 30% of their maximum rates. Since the FSCCs do not have an FDDI interface, a 40 MB/s parallel link was implemented. The FSCCs send data through their 32-bit ECL parallel port to a LeCroy 1190 VME Dual Port 128 kB Memory. Through the second of the two ports, the MV162 controller reads the 1190 at up to 40 MB/s over the VME backplane bus and provides communications through its FDDI interface. Buffered operation over the FDDI network has the greatest throughput, approximately 2 MB/s of data flow, corresponding to 2 kHz of 1 kB events.
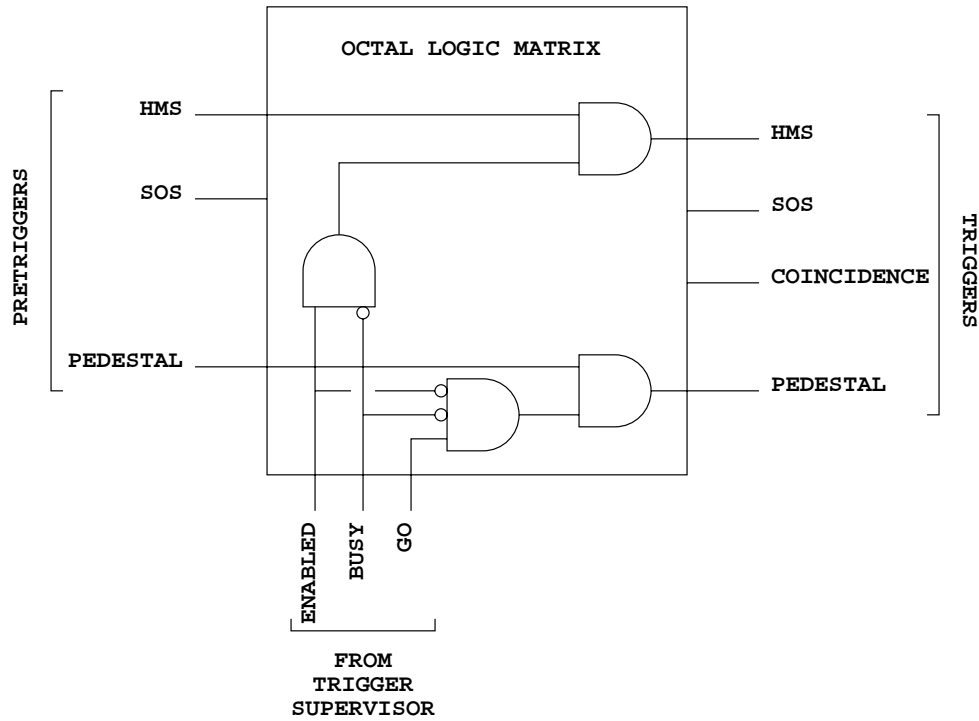
Figure 3.19: Octal logic matrix.

3.5.1 Trigger Supervisor

The Trigger Supervisor [83] provides centralized control of the data acquisition activity. Its implementation for this experiment was extremely simple, with only four Level 1 trigger types consisting of HMS, SOS, coincidence, and pedestal triggers. A LeCroy 2365 Octal Logic Matrix (8LM) constructed these triggers using the PRETRIGs from the trigger logic and the Trigger Supervisor status lines as indicated in Figure 3.19. To handle high rates, the Trigger Supervisor is capable of prescaling each of its trigger inputs by a programmable factor.

When one or more of the trigger inputs is active, the Trigger Supervisor latches the

trigger pattern and simultaneously sets the BUSY to the 8LM to suppress any further triggers. The trigger bit pattern addresses a memory location holding a two byte code. Based on this code, the Trigger Supervisor activates a particular combination of its eight Level 1 Accept outputs; these are transformed externally into gates for ADC modules and starts or stops for TDC modules. The modules receiving these signals acknowledge that their acquisition cycle is under way by asserting their front-end busy.

When all of the front-end modules have completed acquisition, a task which takes approximately 80 μs, the Trigger Supervisor places a readout code corresponding to the trigger type onto its four branch buffers. Each branch buffer communicates with up to eight readout controllers (FSCCs or MV162s). In buffered mode, the depth of the branch buffers is set to eight, the same as the buffer depth within the individual front-end modules. As long as the buffers are not full, the Trigger Supervisor strobes all four branches, rearms itself to accept another trigger, and drops the BUSY to the 8LM. The strobe interrupts the CPU of the controllers and causes them to begin reading the data in the front-end modules according to the readout code on the branch. When all controllers acknowledge completion of their activity, the branch buffer pointer is decremented; if the buffer is not empty, this cycle is repeated. Therefore, buffered mode allows acquisition and readout to proceed relatively independently. In unbuffered mode, the buffer depth is set to 1, which forces the Trigger Supervisor to remain locked to further triggers until the FSCCs

have completed readout of the front-end modules; both acquisition and readout must be complete before a new trigger can be processed.

3.5.2   CODA

CODA components [84] run on each of the computers in the data acquisition system. The primary components are the Readout Controllers (ROCs) and the Event Builder and Analyzer (EBANA). The ROCs, running on the FSCCs and MV162s, handle the readout of the front-end module memory and place these event fragments onto the network data stream. The EBANA, running on the HP 9000/735, collects and reassembles the fragments into whole events. The implementation of EBANA used during this experiment simply saved the events to disk without performing any analysis. In addition to EBANA, the HP 9000/735 also ran a process called RunControl. The RunControl process communicates with the various CODA components to ensure not only that the entire data acquisition system is in the same state, either Booted, Configured, Downloaded, Active, Paused, or Terminated, but also that transitions between these states occur in an organized fashion.

Chapter 4

Analysis

The goal of the data analysis is to reduce and combine the raw data recorded during the experiment from the individual detectors to form the cross sections for inclusive scattering. This analysis divides into three broad sequential tasks. First, the detectors must be properly calibrated. Second, cuts on the response of the calibrated detectors determine reconstructible electron events; this data determines the counting efficiencies, count densities at the central angle as a function of energy loss, and incident charge which combine to produce cross section measurements. Finally, background contributions from charge symmetric processes are removed and radiative corrections are applied to produce the final cross section measurements.

The first two analysis tasks are highly computing intensive, requiring multiple passes through the raw data stored in log files on 25 5 GB data tapes. The following strategy ultimately evolved for dealing with such large volumes of correlated data. A

96

custom built analysis program, written in `FORTRAN`, reduced the log file data for each run into column formatted text files which were compressed using `gzip`, a standard `UNIX` utility. This stage was implemented as a filter. A combination of shell scripts and the `awk` utility were used to access this multifile database and extract data matching various required conditions. This strategy proved highly flexible, simple, efficient, and platform independent, much more so than one based upon the common, but inscrutable and out dated, `PAW` analysis package.

4.1   Calibration

Calibration required a complete pass through the experimental log files on tape. Very crude analysis of the raw data permitted the selection of events appropriate for calibration purposes. The calibration analysis sought to achieve a consistent treatment of the detector responses based on the totality of data collected throughout the experiment. The hodoscope signal velocities and timing offsets were determined first. With the hodoscopes thus functioning properly to measure the start time, the drift times from the drift chambers could be measured and converted to the drift maps needed for track fitting. The Čerenkov detector was easily calibrated by isolating the single photoelectron response of each phototube. Using electron events selected by the calibrated Čerenkov signal, the average response for each calorimeter block was measured and parameterized as a function of momentum, with a correction for the

attenuation of signal along its length. The normalized responses of each block were weighted with a layer dependent coefficient and summed to produce the calorimeter energy measurement. The following describes these calibration procedures in greater detail.

4.1.1 Timing

Figure 4.1 is a timing diagram for a representative hodoscope element and its two phototube signals. The goal of the hodoscope calibration is to correct for the known variations and relative offsets in the signal times so that they cluster around a constant, arbitrarily selected reference time. The shifted and corrected TDCs then measure the start time indicated in the timing diagram. Addition (subtraction) of the start time to any TDC stopped (started) by the trigger produces measurements relative to the fixed reference time rather than to the trigger time, which contains the unknown variation arising from the time the trigger logic takes to decide the validity of the event. Since in this experiment the start time is used only in the determination of the drift times, as discussed in the next subsection, the start time needs to be known only to about 0.5 ns, which is the bin size used in the calculation of the drift maps.

Because of this relatively loose requirement, the only significant variation in the signal time is the time s/v for the scintillation to travel with velocity v the distance
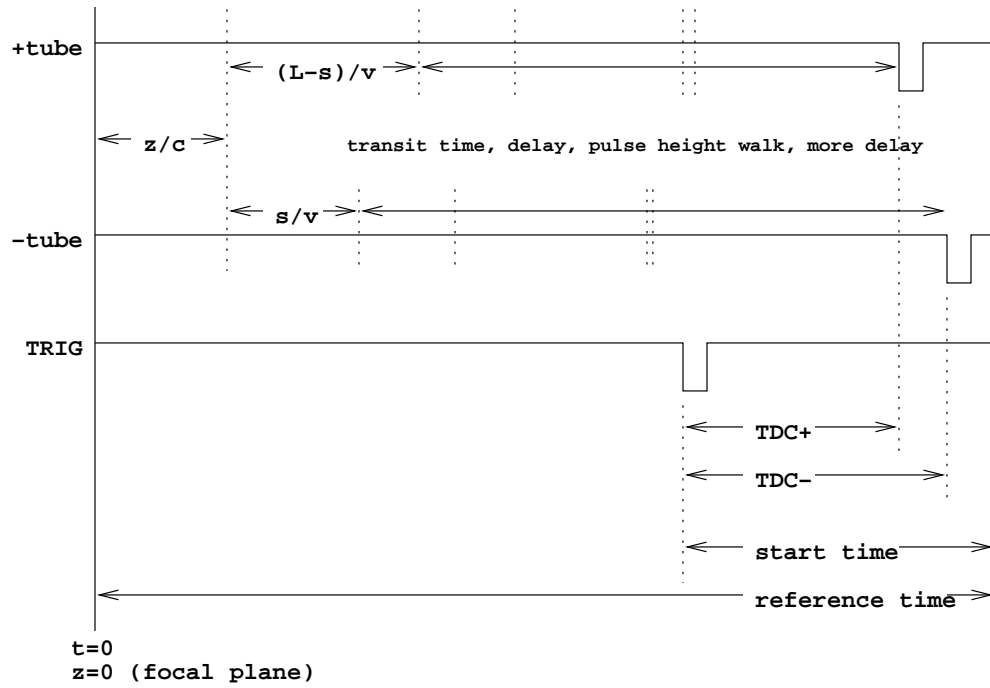
Figure 4.1: Timing diagram for the two signals on a representative hodoscope element. See the text for details.

s from the point of origin down the element of length L to the phototube. Since the particle tracks are nearly parallel to the central ray, the time of flight z/c from the focal plane ($z = 0$) to the hodoscope plane varies negligibly. Likewise, the transit time jitter, fluctuations in the time for the photoelectron signal to travel down the dynode chain to the anode, is extremely small ($\sigma \approx 100$ ps) for these phototubes. The variation in the pulse height walk, the timing shift due to the discrimination at a fixed level of pulses of varying size, is typically less than 0.5 ns and can also be neglected for the present purposes.

One of the calibration tasks therefore is to determine the signal velocities v for each hodoscope element. Considering both signals in the timing diagram, it is evident that
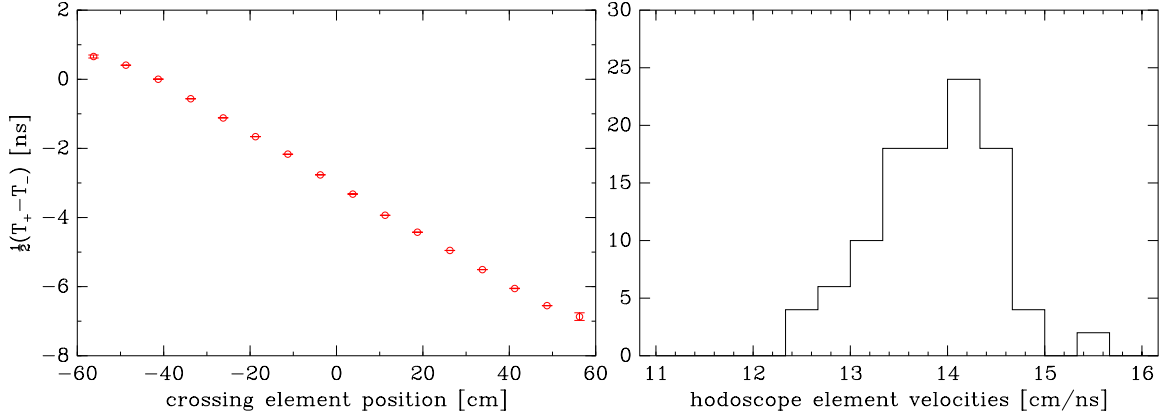
Figure 4.2: The left panel indicates the timing difference of the $+$ and $-$ tubes as a function of the location of the signal; the slope determines the signal velocity. The right panel indicates the distribution of velocities determined for all 52 hodoscope elements.

the trigger time cancels out in the difference of the TDC measurements, leaving only a dependence on s/v. The location s can easily be determined from the index of the crossing element from the immediately neighboring hodoscope plane. The correlation of the TDC differences with s is shown on the left in Figure 4.2 for a representative element. Evidently, the slope determines the signal velocity; the distribution of signal velocities measured in this manner is indicated in the right panel. These velocities are somewhat smaller than the value determined by the index of refraction ($c/n \approx$ 19 cm/ns) due to the multiple internal reflections needed for the light to reach the end of the hodoscope element.

The other calibration task is the determination of the timing offsets among the signals. This procedure is best described with a specific example. Consider just the signals from the 1X+ group. A central element from the 1Y plane is selected to
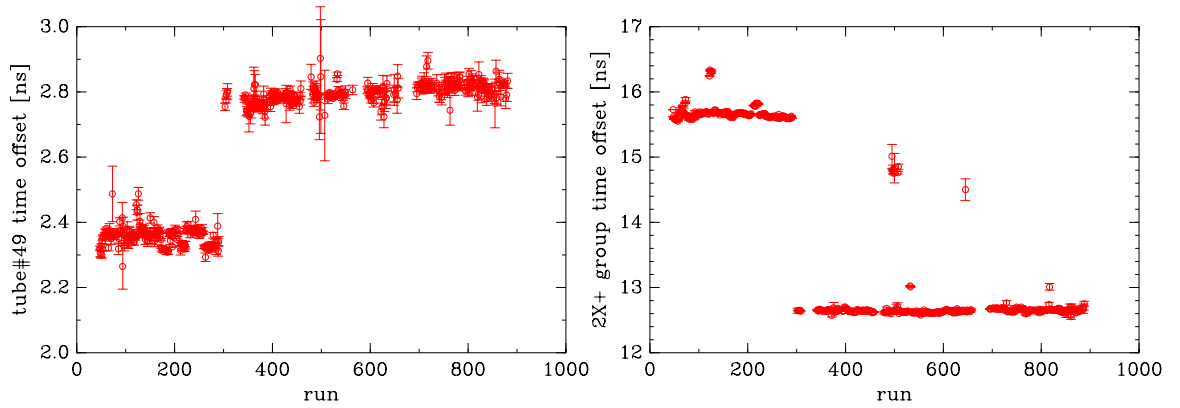
Figure 4.3: Hodoscope timing offsets.

provide a reference time for this group. The reference time is the average of the +

and − signals from this reference element. The average contains just the timing of the

trigger and an unimportant overall timing offset: from the timing diagram, it is clear

that the velocity corrections average to the constant value $L/2v$, where L is the total

length of the element, which simply contributes to the overall timing offset. When

the 1X+ signals are measured relative to this reference time, the trigger time cancels

out, and the velocity correction across the width of the crossing reference element is

negligible. These relative times therefore measure the offsets among the 1X+ signals.

Once the relative offsets are determined and the signals are thus self-aligned within

each of the eight groups (1X±, 1Y±, 2X±, 2Y±), the relative timing between the

groups is determined in an analogous manner by choosing the 1X+ group as the

timing reference. Just as before, the trigger timing cancels out, and after applying

the velocity corrections, the relative time contains just the group timing offsets. Fig-

ure 4.3 illustrates examples of the signal and group offsets as measured throughout

the experiment. There was one significant shift in the offsets occuring at run 9300, which coincided with a one day shutdown. As the figure indicates, the timing shifts of individual signals were small, but the shifts between signal groups were significant, on the order of a few nanoseconds.

Finally, with the hodoscope properly calibrated, the start time is computed from the corrected TDC values for each event. The simplest approach is to average the corrected TDCs. However, it was found that the average can be significantly affected by noise hits. Instead, the median value was found to be a much more robust determinant of the start time.

4.1.2 Tracking

The calibration of the drift chambers requires the construction of drift maps from the drift time histograms; these drift maps convert drift times into the drift distances used in the tracking algorithm. Since the idea of a drift map assumes that a direct functional relationship $x = f(T)$ exists between the drift distance x and drift time T, the number of events in an interval dx in drift distance must equal the number of events in the corresponding interval dT in drift time:

$$\frac{N}{0.5 \text{ cm}} \, dx = h(T) \, dT$$
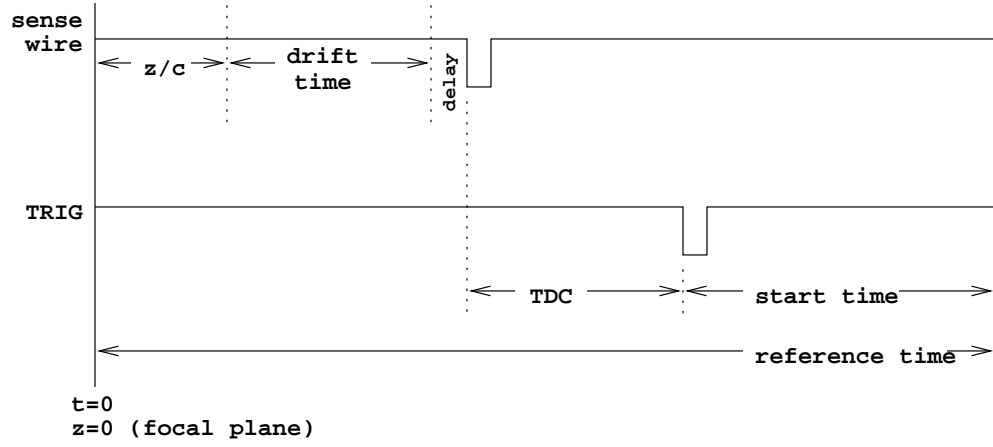
Figure 4.4: Timing diagram for a representative sense wire in the drift chambers.

where the drift distance event distribution is uniform ($N/0.5$ cm) across a drift cell, and the drift time event distribution (histogram) is $h(T)$. Evidently:

$$x = 0.5 \text{ cm} \cdot \frac{1}{N} \int_0^T h(T') \, dT'$$

That is, the drift map $x = f(T)$ is obtained by simply integrating the (normalized) drift time histogram.

Figure 4.4 indicates the timing of a representative sense wire in the drift chambers. As described in the last subsection, the TDC value recorded for this sense wire signal contains the variation of the time required for the trigger logic to issue the trigger signal to stop the TDC unit; consequently, the start time is added to the TDC to produce a measurement of the timing sense wire signal relative to the fixed reference time. The timing diagram indicates that, up to an overall offset, the negative of this sum determines the drift time. Part of the offset in the drift time arises from the
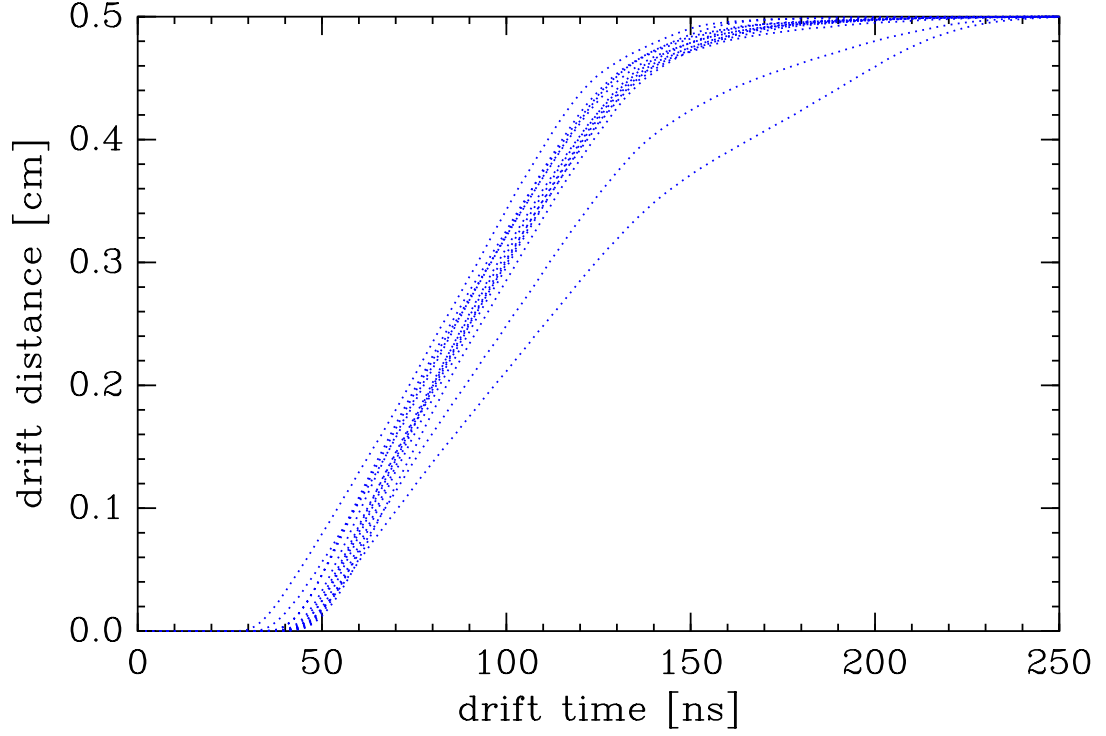
Figure 4.5: A representative set of drift maps.

delay from the length of ribbon cable connecting the electronics card on which the sense wire signal is processed to the TDC module.

These offsets must be accounted for before the drift maps are computed. The standard Hall C analysis does not account for these cable delays; drift maps are constructed for each of the twelve planes. Consequently, the tracking would degrade when the event distribution favored some cards over others, thus weighting the importance of the offsets differently, and the frustrating situation would arise that the drift maps would frequently need to be recalculated. The approach adopted for this analysis is to compute one drift map for each of the 72 cards, which by default accounts for

the timing offsets. In addition, the drift map for a card was recomputed as soon as sufficient statistics were accumulated for an accurate measurement (typically every 30000 events) in order to compensate for the effect of varying gas mixtures on the performance of the drift cell.

Figure 4.5 illustrates the set of all drift maps at one point during the experiment. There is a clear linear relationship between drift distance and time; this corresponds to the slow dependence of mobility on field strength as discussed in the previous chapter. The effect of the timing offsets among the cards is seen as the roughly 20 ns wide band. This range of offsets is extremely large by comparison to any other timing standard. The two abnormal drift maps sagging below the others illustrate the effect of a poor gas mixture.

4.1.3   Čerenkov

Calibration of the Čerenkov detector simply requires the normalization of the signals from each phototube. Since the Burle phototubes provide good single photoelectron resolution, such a normalization is readily accomplished by identifying the location of the single photoelectron peaks in the ADC histograms. The single photoelectron response may be isolated by choosing only events which should produce little or no response in a given phototube, for example pion events as identified by the calorimeter or any event with a trajectory not passing through the active range of
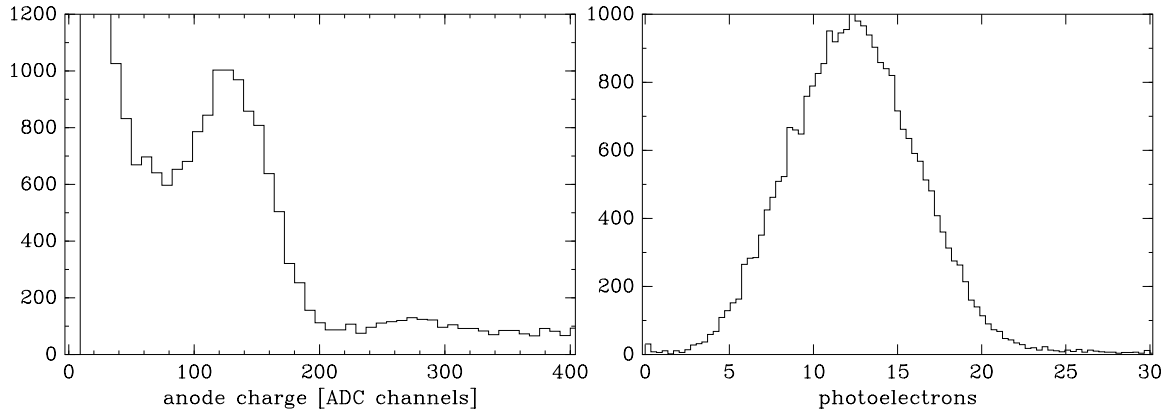
Figure 4.6: The single photoelectron peak for one of the phototubes in the Čerenkov detector (left) and the calibrated Čerenkov total photoelectron yield right).

the phototube/mirror pair.

An example of such an ensemble is illustrated in the left panel of Figure 4.6. The tail of the pedestal is evident at low ADC values; unfortunately, throughout the experiment, the pedestal showed a broad width of 30 to 50 channels indicating considerable noise. The single photoelectron peak shows up clearly near channel 135. As corroboration, a prominence from double photoelectron events appears in the proper place near channel 270.

The normalized signals from both phototubes are summed to produce a single signal representing the total response of the Čerenkov detector. The right panel of Figure 4.6 presents an example of the full Čerenkov response. This signal averages approximately 14 photoelectrons per event. Although not enough to produce any significant effect on the electron identification efficiency, the Čerenkov response does contains some position dependence, with less yield near the overlap of the two mirrors

as well as at the extremes of position and angle. Internal optical misalignments are partly to blame, as is the completely unknown alignment of the entire detector relative to the optical axis of the spectrometer. Thorough simulations of the optics of this detector indicate tight tolerance for full transport of the Čerenkov cone to the phototubes over the entire range of accepted phase space. Position dependence of the photoelectron yield is therefore not surprising.

4.1.4 Calorimeter

Each of the 52 blocks of the calorimeter must be calibrated for the attenuation of the light signal along the length of the block. In addition, the gains must be normalized for calculation of the shower energy. Rather than identifying 52 gain calibration coefficients, however, a slightly more complicated approach was taken. The momentum dependence of the average ADC for each block was parameterized. The sum of the ADCs normalized by these parameterizations are then weighted with four parameters, one for each layer, and summed to compute the normalized calorimeter energy E/p with minimum width. Since the calibration in this approach is momentum dependent, the E/p computed in this manner is not a pure measurement of the shower energy; instead this approach is aimed at optimizing the particle identification performance since electron events will cluster in the tightest possible peak at $E/p \equiv 1$.

The energy deposition from an electromagnetic shower is well described by a
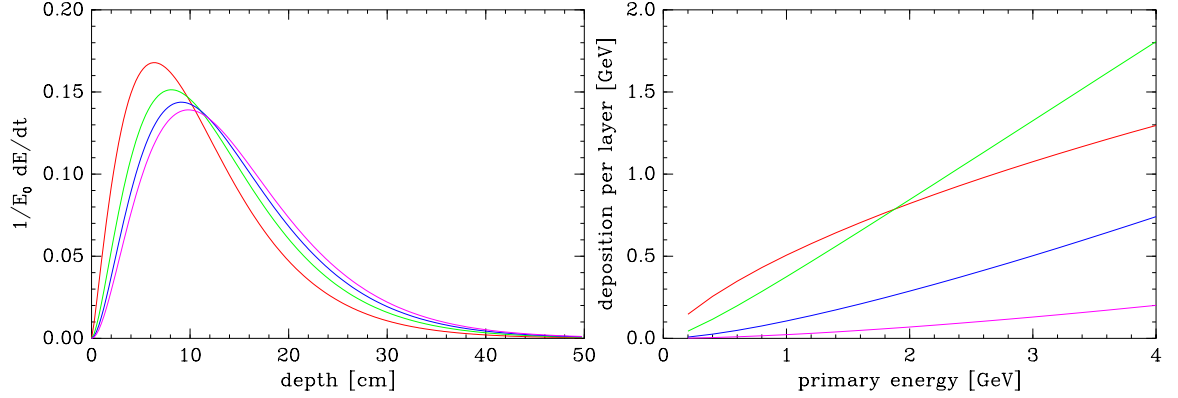
Figure 4.7: Calculations of the calorimeter response using the gamma distribution. See the text for details.

gamma distribution [81]:

$$\frac{dE}{dt} = E_0 b \frac{(bt)^{a-1} e^{-bt}}{\Gamma(a)}$$

where E_0 is the primary (incident electron) energy, t is the depth within the material in radiation lengths, $b \approx 0.5$, and $a - 1 = b\left(\ln(E_0/E_c) - 0.5\right)$ with the critical energy E_c, defined as the energy at which the radiative and ionization energy losses are approximately the same, approximately 48 MeV for the TF-1 lead glass used in the calorimeter. Figure 4.7 illustrates this calculation. The left panel shows how the energy deposition broadens as E_0 increases (the red, green, blue and magenta curves correspond to E_0 = 1, 2, 3, and 4 GeV), and that the total energy of the primary electron is absorbed within the 40 cm depth of the calorimeter. The right panel indicates the deposition in each layer as a function of E_0 (red, green, blue, and magenta correspond to the first, second, third, and fourth layer).

The same qualitative dependence of the deposition per layer on E_0 is, in fact, seen
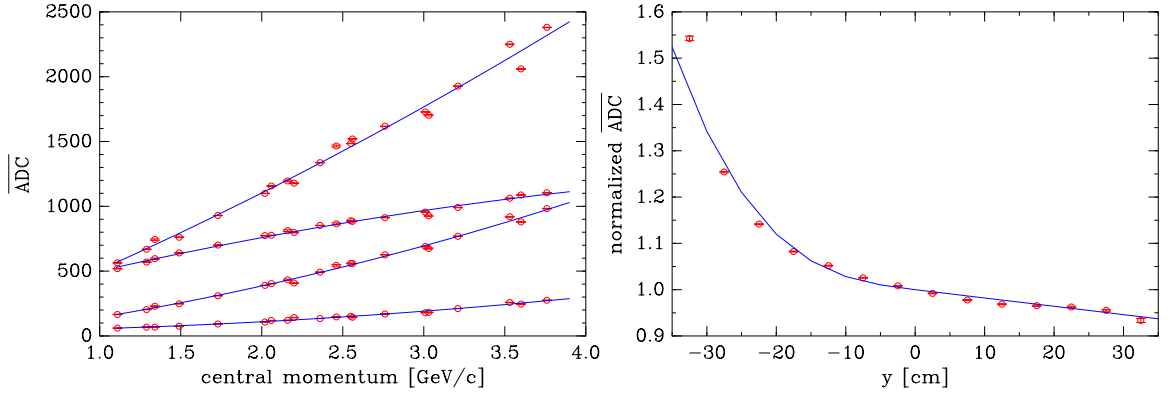
Figure 4.8: Examples of the calibration of the momentum dependence (left) and signal attenuation (right) in the calorimeter. In the left panel, the curves from top to bottom correspond to the second, first, third, and fourth layers.

in the ADC response of the individual lead glass blocks. Using the trajectory from the drift chambers and the Čerenkov for electron identification, electron events which track to a narrow 15 cm vertical stripe along the center of the calorimeter are used to generate the average ADC yield from each block as a function of central momentum. The left panel of Figure 4.8 shows an example of this for the sixth block from each of the four layers as a function of the momentum setting. This behavior is clearly similar to the computed dependence shown in the last figure, with the response of the rear layers increasing relative to the front layers as the energy deposition pushes deeper into the calorimeter.

With this momentum dependent normalization from the central 15 cm region parameterized for each lead glass block, it remains to calibrate the effect of the attenuation of signal along the length of the blocks (y). An example of this for one block is illustrated in the right panel of Figure 4.8. The location of the phototube at the

Layer	1	2	3	4
Coefficient	0.365	0.421	0.157	0.057

Table 4.1: E/p calibration coefficients for each layer of the calorimeter.

end of the block causes the rapid increase in response at negative y.

Now that all of the dependences in the ADC responses have been measured and parameterized, the normalized shower energy E/p can be calibrated. E/p is computed as the weighted sum of the ADC values normalized by both the momentum and attenuation parameterizations. The weights in the sum are layer dependent coefficients selected so that the ensemble average of the sum is 1 with minimum width. Table 4.1 indicates the weights as determined by a χ^2 minimization on this requirement. As described in the previous chapter, the transverse spread of the energy deposition is contained (conservatively) within a 3×4 block region. Rather than summing over all blocks, the contribution of noise to the sum is limited by selecting the 3×4 block region with the largest response.

Figure 4.9 illustrates the result. The distribution of E/p has a very narrow width of $3.5\%/\sqrt{E}$. The small bump below the electron peak comes from pions; although well separated, the long tail of the pion response in the calorimeter leaks under the electron peak.
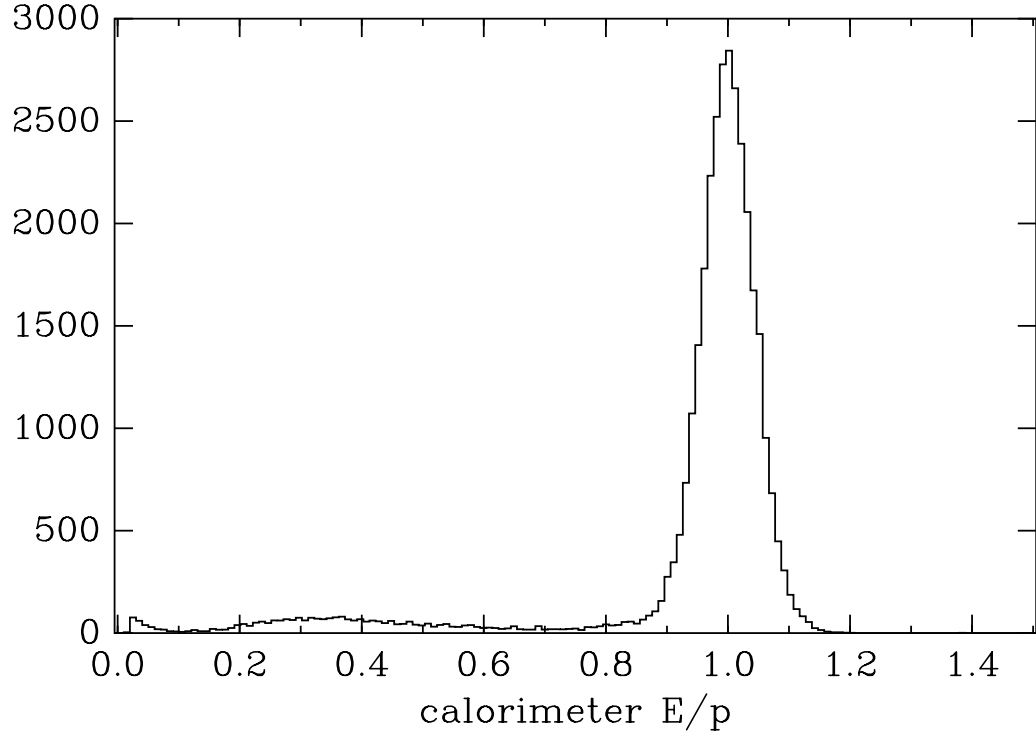
Figure 4.9: An example of the E/p measurement.

4.1.5 Reconstruction

The reconstruction transformation converts the measured set of four parameters x, x', y, y' reported from the tracking algorithm which represent a focal plane trajectory into a set of four parameters x', y, y', δ representing the trajectory as the particle left the target. The parameter $\delta \equiv (p - p_c)/p_c$ is the momentum fraction relative to the central momentum setting of the spectrometer p_c. The other parameters are the two slopes x' and y' projected into the xz and yz planes, and the horizontal coordinate y in the object plane.

The projected slopes relative to the spectrometer coordinate system are readily

converted into the polar and azimuthal angles θ and ϕ relative to the beam axis:

$$
\begin{aligned}
\cos\theta &= \frac{y'\sin\theta_c + \cos\theta_c}{\sqrt{1 + (x')^2 + (y')^2}} \\
\tan\phi &= \frac{x'}{y'\cos\theta_c - \sin\theta_c}
\end{aligned}
$$

where θ_c is the central angle of the spectrometer.

Since no transformation of four parameters can determine five independent parameters, the trajectories are assumed to always originate from the target with the vertical coordinate $x \equiv 0$; this condition is maintained experimentally with a sufficiently small raster and a stable beam position. The reconstruction transformation for each target quantity is a multidimensional polynomial truncated at fifth order:

$$
\sum_{i,j,k,l=0}^{i+j+k+l=5} c_{ijkl} \cdot (x)^i (x')^j (y)^k (y')^l
$$

The coefficients c_{ijkl} are referred to as reconstruction matrix elements, in reference to the matrix formalism of optics.

A set of reconstruction matrix elements were determined from a combination of nuclear elastic, sieve slit, and slanted target data [85]. By adjusting the momentum setting of the spectrometer incrementally, the nuclear elastic data allow for the calibration of the dispersion matrix elements (δ reconstruction). Angular matrix elements may be determined by requiring that the holes of the sieve slit placed at the entrance
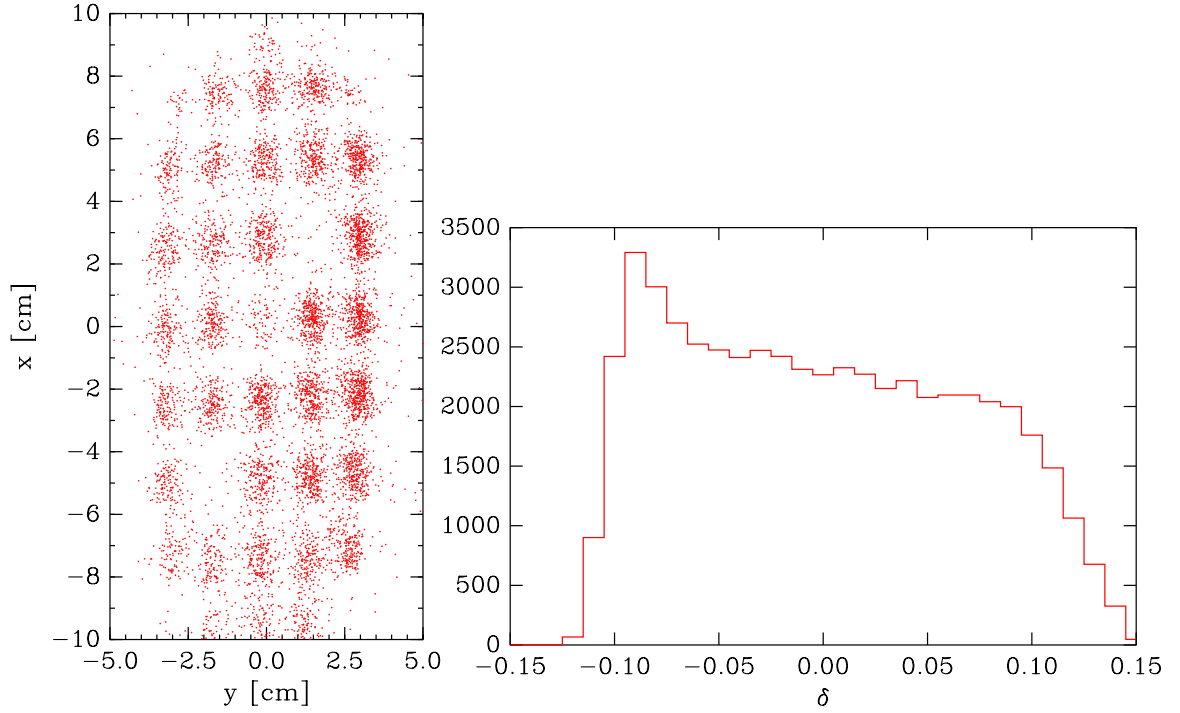
Figure 4.10: Sieve slit (left) and δ (right) reconstruction. See the text for details.

to the spectrometer be resolved. Finally, adjusting the height of a slanted target allows the intersection of the beam and target to be set at different locations along the beam axis, which allows calibration of the extended target (y) reconstruction.

As illustrated in the Figure 4.10, the reconstruction is not perfect. The left panel shows that there is a clear distortion in the location of the reconstructed sieve slit holes. In addition, the momentum reconstruction, shown in the right panel, is also inadequate at large negative momentum fractions. This is evident in the increase in yield beyond $\delta \approx -8\%$. Aperture effects can only reduce the accepted volume of phase space; increasing yield therefore indicates improper momentum calibration. In fact, the reconstruction is actually an extrapolation in this region since the last set

of nuclear elastic data stopped at $\delta = -8\%$, so the poor results are not surprising.

4.1.6   Beam current

In order to turn the scaler data (see section 3.2.3) from the current monitors into current and charge measurements, there are two calibration tasks required. First is the determination of the zero offsets of the scaler rates, and second is the gain calibration. The current is parameterized by:

$$
I = \begin{cases} C \cdot \sqrt{r - r_0} & \text{BCM1} \\[2ex] C \cdot (r - r_0) & \text{BCM2, Unser} \end{cases}
$$

where r is the scaler rate, r_0 is the zero offset of the scaler rate when beam is absent, and C is the gain calibration constant. The two different forms reflect the differences in the electronics instrumenting the monitors, as described in the previous chapter.

The Unser zero offset drifts and fluctuates severely on a time scale of a few minutes, but the gain is extremely stable and linear. An absolute calibration of the Unser gain was performed prior to the experiment, which measured C=250.10±0.05 μA/MHz. Therefore, for a few minutes following an Unser zero offset measurement, the Unser provides an absolute measurement of the beam current and can therefore be used to cross calibrate the gain of the cavity monitors BCM1 and BCM2.

The calibration procedure involves the selection of beam off to beam on transitions
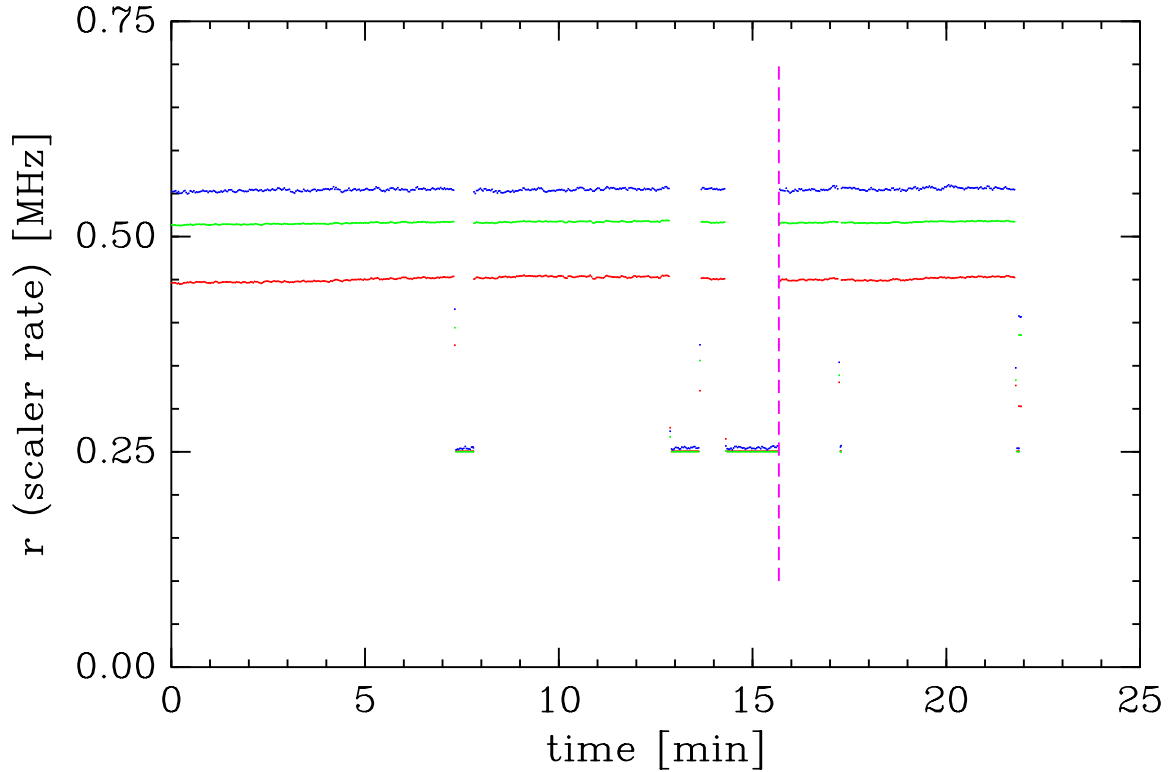
Figure 4.11: Current monitor scaler data (blue, green, red) for run 9579. The vertical dashed line marks a beam off/on transition useful for calibration. The transitions not marked were of insufficient duration.

that occurred either accidentally or intentionally during the course of the experiment.

An example of the scaler record indicating a transition useful for calibration is shown in Figure 4.11. The beam off periods of such transitions are used to measure the zero offsets r_0. As expected, the values obtained for r_0 for both BCM1 and BCM2 over the course of the experiment showed very little systematic variation and negligible fluctuation; the averages $r_0 = 0.25067$ MHz for BCM1 and $r_0 = 0.25004$ MHz for BCM2 sufficiently characterized the offsets for the whole experiment.

The transfer of gain calibration from the Unser to BCM1 and BCM2 from these
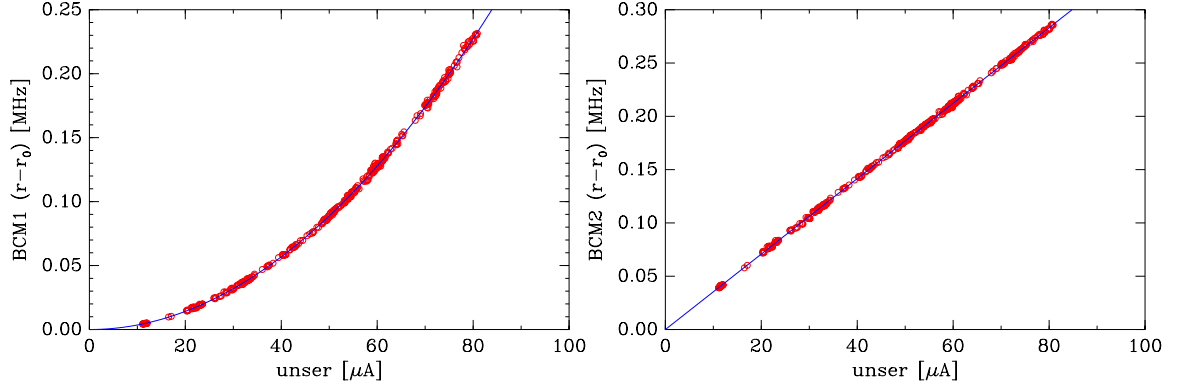
Figure 4.12: Gain calibration transfer from the Unser monitor to the cavity monitors.

transitions is indicated in Figure 4.12. These data are fit to the appropriate forms to obtain the values $C = 167.78 \pm 0.05$ $\mu A/\sqrt{MHz}$ for BCM1 and $C = 282.60 \pm 0.08$ $\mu A/MHz$ for BCM2. Although these parameters are accurately determined, the fluctuations of the data about the parameterization indicate that the current measurement using these calibrations for BCM1 and BCM2 is good only to approximately 1%.

4.1.7 Beam energy

There are several independent measurements of beam energy, all of which are consistent within approximately 5 MeV of the nominal beam energy of 4.045 GeV reported by the accelerator. For one pass beam at 845 MeV, the differential recoil method measured the separation of the elastic peaks for Oxygen and Beryllium from a BeO target; from kinematics, the mass differences make this peak separation proportional to the square of the beam energy. The accuracy of this method [86] was determined to

be approximately 0.2%. Additional kinematic cross checks, including using the known location of the ^{12}C diffraction minimum and coincidence H(e,e'p), produced similarly consistent results with similar uncertainty. Lastly, special runs were designated to operate the Hall C arc as a 12 cm/% beam energy spectrometer, as described in the last chapter, which obtained beam energy measurements for all passes of beam with slightly better accuracy of 0.1%.

4.2   Cross section measurement

Following the calibration analysis, a second analysis through the raw data tapes was executed to compute the calibrated output of the detectors for each event; the results for each run were stored in a compressed text file database consisting of 92 columns of data per event. This body of processed data occupied only 8 GB of disk space.

Using the results of this second analysis pass, the set of events which produced a Čerenkov signal exceeding 3 photoelectrons, a calorimeter response satisfying $E/p > 0.7$, and an unambiguous track in the drift chambers were defined as electrons and used for the construction of the cross section measurements. These electron events were sorted into E' bins defined by $\ln(E'_i/E'_0) = i \cdot 0.01$ where $E'_0 = 1.0$ GeV/c and i is an integer index; this is a global 1% binning, independent of the central momentum settings for individual runs. Although this fractional width is large in comparison to the spectrometer resolution, which is approximately 0.2%, the bin widths in E' cover

a reasonable range from 10 MeV to 40 MeV.

For each bin, the distribution of events in E' and θ was analyzed to determine the count density $dN/dE'd\Omega$ at the central values $E' = E'_i$ and $\theta = \theta_c$, where θ_c is the spectrometer angle. These count densities, suitably normalized, determine the cross sections:

$$\frac{d\sigma}{dE'd\Omega} = \frac{1}{Q \cdot \rho t N_A/M} \cdot \frac{\text{PS}}{\epsilon_{trig} \cdot \epsilon_{daq}} \cdot \frac{1}{\epsilon_{track} \cdot \epsilon_{pid}} \cdot \frac{dN}{dE'd\Omega}$$

The first factor normalizes the counts to the total number of electrons Q incident on the target and to the number of nuclei per unit area $\rho t N_A/M$, where ρ is the density, t is the thickness, and M is the atomic mass of the target, and N_A is Avogadro's number. The second factor corrects the number of counts for the hardware inefficiencies from the trigger and data acquisition system. The factor PS is the prescale factor which is programmed into the Trigger Supervisor to dilute the number of recorded events for runs with excessively high data rates. The third factor corrects for the inefficiency of the software cuts used to define the electron sample for this pass of analysis.

All cross section measurements sharing the same E' bin, spectrometer angle, target thickness, and target angle were accumulated using the weighted mean. Once the charge symmetric backgrounds were removed and the radiative corrections were applied, these measurements with differing target thicknesses and target angles were combined, again using the weighted mean, to produce the final cross section measure-

Source	Uncertainty [%]	
charge	1.0	
target thickness	1.0	
trigger	< 0.1	
tracking	< 1.0	
particle identification	0.5	
$e^\pm$ subtraction	< 4	(45 deg.)
	< 10	(55 deg.)
radiative correction	3.0	

Table 4.2: Sources of systematic uncertainty.

ments for each nucleus, at each spectrometer angle, and as a function of E'. Each of the contributions to the cross section measurements, the hardware and software efficiencies, the count densities, the charge symmetric background, and the radiative corrections, is described in detail in the following subsections. Table 4.2 summarizes the systematic uncertainties associated with each contribution.

4.2.1 Hardware efficiencies

Trigger

There are two contributions to the cross section measurement from the trigger, the trigger efficiency and the dead time correction. As described in the previous chapter, the trigger is designed to be extremely efficient for electrons while inefficient for all other particles. The trigger is the logical OR of the ELLO and ELHI logic, each built from logic signals derived from the hodoscopes (SCIN and STOF), the Čerenkov and the calorimeter (SHLO, PRHI, and PRLO).
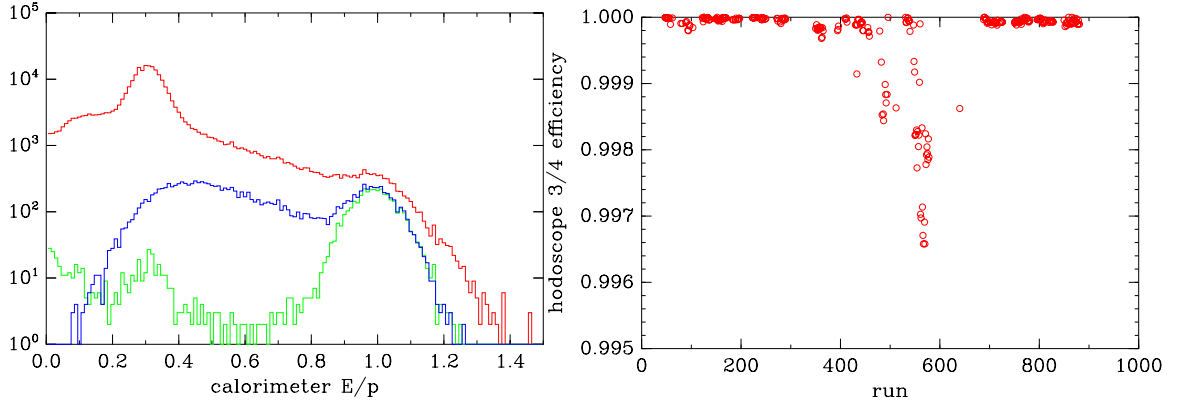
Figure 4.13: The left panel is discussed in the text. The right panel indicates the hodoscope 3/4 efficiency.

The particle identification components of the trigger are extremely efficient. A few runs were taken during the experiment with the particle identification requirements removed from the trigger; a TDC was used to record the logic signals so that the unmodified trigger could be reconstructed in software. From these runs, the calorimeter requirements of the ELHI logic is found to be approximately 96% efficient for electrons. The PRHI requirement in ELLO accounts for almost all of this inefficiency. The left panel of Figure 4.13 illustrates this; the red curve is the full histogram, while the blue curve corresponds to those events which would have passed through the ELHI part of the unmodified trigger. The overall suppression comes from the PRHI requirement of ELHI, while the cut-off below $E/p \approx 0.4$ comes from the SHLO requirement. The green curve indicates the events passing the ELLO part of the unmodified trigger. Since the PRLO is correlated with PRHI, the Čerenkov controls the particle identification contribution of the ELLO logic. Combining the 96% ELHI efficiency with even

an unreasonably low 99% Čerenkov efficiency, the trigger efficiency is 99.96%. Since the Čerenkov is typically *much* better than this, the overall particle identification contribution to the trigger efficiency is, for all practical purposes, unity.

The trigger efficiency is therefore controlled by the hodoscope `SCIN` efficiency, which is also nearly 100% efficient. This is evident in the right panel of Figure 4.13 which illustrates the `SCIN` efficiency throughout the experiment. The `SCIN` logic requires that three of the four hodoscope planes fired; the efficiencies in the figure are computed using simple combinatorics with the individual plane efficiencies.

The remaining effect of the trigger is its dead time. Should a second particle arrive within the time interval required for the trigger to latch a prior particle, the second particle may not be counted. This effect can be measured by establishing copies of the trigger with varying duration and observing the difference in the number of counts recorded in the different scaler channels. Unfortunately, this hardware was not implemented properly. Nevertheless, due to the CW beam and the short 30 ns trigger, the event rates never were high enough to make this a relevant effect, so no correction is applied.

Data acquisition

The data acquisition system requires a nonzero time interval, on the order of a few hundred microseconds and depending upon the acquisition mode, to digitize and record the signals from the detectors for an event. Therefore, when event rates are
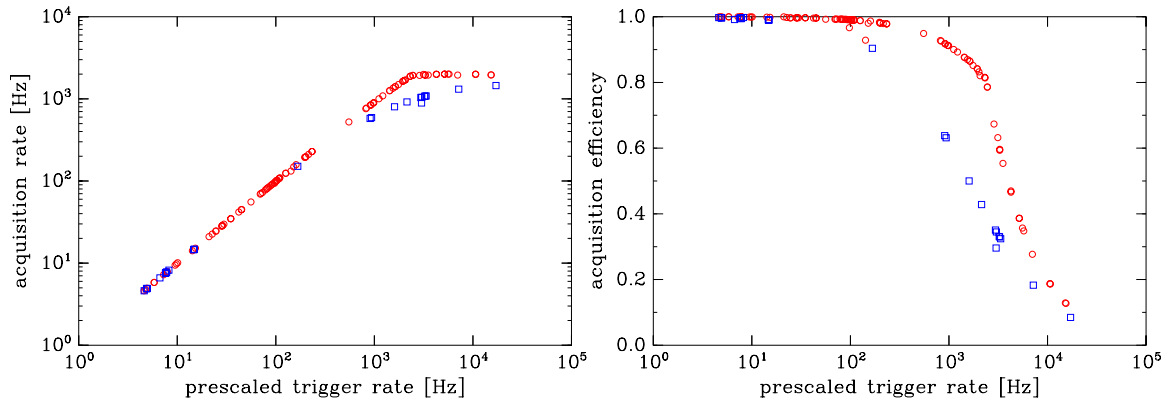
Figure 4.14: The dependence of the DAQ performance on trigger rate. The red circles correspond to the parallel-linked, buffered acquisition mode, and the blue squares correspond to the unbuffered mode.

high enough, there is a bottleneck at the interface between the trigger and the data acquisition system. This increases the dead time and makes the DAQ inefficient.

Figure 4.14 indicates the dependence of both the acquisition rate and the acquisition efficiency as a function of the trigger rate. The linear region is where the DAQ can keep up, but at high enough rates, the limiting value of the acquisition rate is evident. The linearity of the parallel-linked and buffered acquisition mode clearly extends to much higher event rates than does the unbuffered mode.

The remaining effect of the data acquisition is the prescaling factor, which is the fraction of the events automatically rejected by the Trigger Supervisor. There is no error associated with either the acquisition efficiency or the prescale factor.

4.2.2 Software efficiencies

Particle identification

The criteria used to identify electrons require that the Čerenkov detector response exceed 3 photoelectrons *and* that the calorimeter response satisfy $E/p > 0.7$. Since these detectors act independently, this total particle identification efficiency is simply the product of the individual efficiencies of these two detectors, and is found to be $99.3 \pm 0.5\%$, as explained in the following discussion.

Except under special circumstances, measurement of the individual detector efficiencies on a run to run basis is not possible. The simplest measurement uses one detector to define an electron sample; the fraction of these events also identified as electrons in the other detector determines the efficiency. The quality of this measurement depends upon the purity of the electron sample. Contamination, particularly from pions, causes this straightforward measurement to falsely report poorer efficiency. Because the Čerenkov does a good job of rejecting pions, this is not so much of a problem for the calorimeter efficiency measurement, but the long pion tail in the calorimeter contributes a significant amount of contamination under the electron peak.

This also introduces a dependence of the efficiency measurements on the relative amount of contamination. Figure 4.15 illustrates the set of efficiency measurements obtained throughout the experiment binned and averaged according to their relative
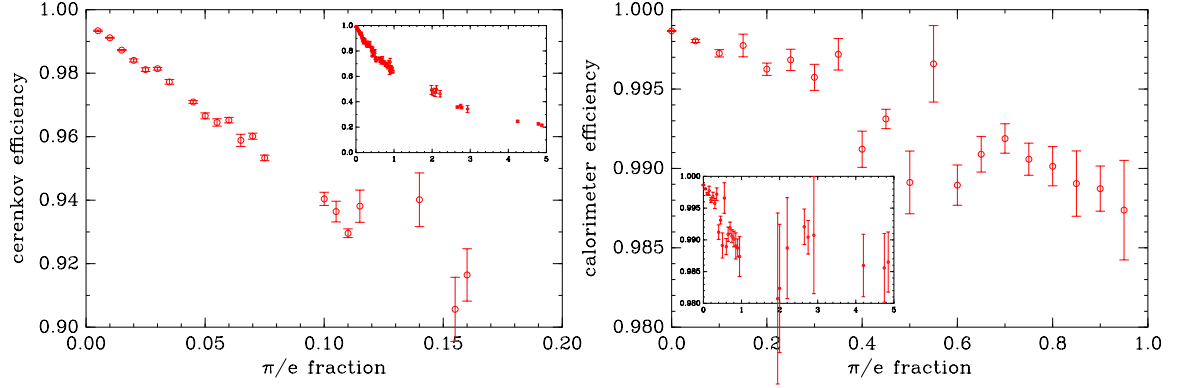
Figure 4.15: Effect of the pion contamination on the Čerenkov and calorimeter effi-
ciency measurements. The extrapolation to zero contamination deter-
mines the true efficiencies. The insets show the dependence over a wider
range of contamination.

pion content. Pions, for this purpose, are defined as events for which the Čerenkov
response is less than 1 photoelectron and the calorimeter response satisfies $0.5 <
E/p < 0.7$. The reason for the relatively high calorimeter cut is to avoid any spurious
problems arising from the hardware trigger inefficiency for pions.

Provided the electronics are stable, there is no reason to expect that the true
efficiencies should change throughout the experiment, so the extrapolation to zero
pion content in the figures should represent a suitable measure of the true efficiencies.
Using this procedure, the 3 photoelectron cut on the Čerenkov is determined to be
$99.5\pm0.5\%$ efficient and the $E/p > 0.7$ cut on the calorimeter is $99.8\pm0.2\%$ efficient.
Therefore, the total particle identification efficiency is $99.3\pm0.5\%$.

Tracking

For an event to be unambiguously trackable, it is required that the tracking algorithm identify only one track from the pattern of hits in the chambers, and that the hits on the track be isolated from any other hits by at least 2 wires for the X, U, and V planes, and at least 4 wires for the Y planes. This ensures that the track corresponds to the primary particle, rather than to any secondary particles that might have been produced, and that it accurately reflects the correct parameters of the trajectory. The tracking efficiency corresponding to these requirements is illustrated in Figure 4.16; the events deemed appropriate for measuring the drift chamber efficiency were those which indicated a clear track in the hodoscopes which roughly matched up to the location of energy deposition in the calorimeter. The justification for these conditions defining a trackable event is presented in the following discussion; the nomenclature from the original description of the tracking algorithm [87] is adopted here.

The tracking efficiency can be broken down into two pieces. First is the efficiency of the algorithm, and second is the likelihood that a unique track can be identified from a given pattern of hits in the chambers. The algorithm efficiency may be tested by simulation. When hits are placed in the chambers from a known track, with no noise, the algorithm has no problem identifying the track except when at least one Y plane is missing. In these cases, the efficiency may drop as much as 10% depending upon the value of y'. Despite this inefficiency, the tracks formed in these
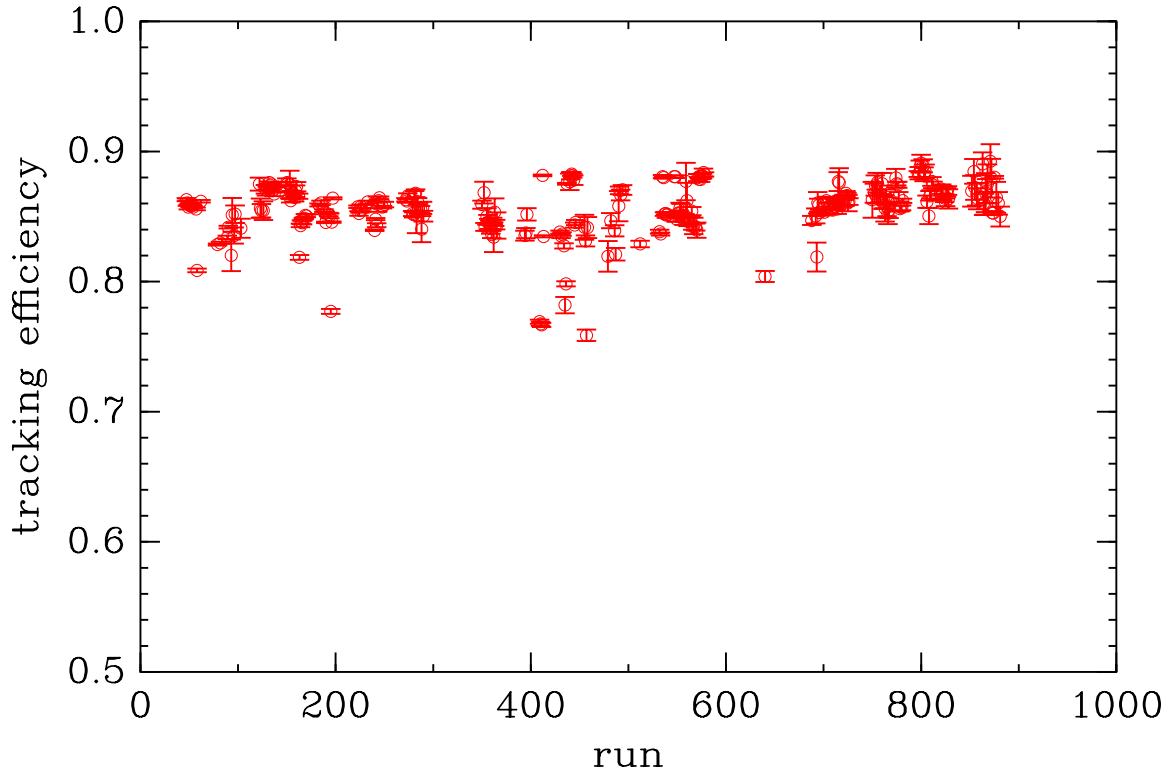
Figure 4.16: Tracking efficiency as measured throughout the experiment.

cases correctly reproduce the input trajectory.

The addition of noise can confuse the algorithm, causing it to report tracks which differ from the real trajectory. The stereo (U and V) planes ordinarily play an extremely important role in the function of the drift chambers as a tool for tracking. The minimal configuration of any drift chamber consists of one X, one Y, and one U plane; without the U plane, an event with just one noise hit on either the X or the Y plane produces two indistinguishable wire intersections. The stereo plane removes this degeneracy. Unfortunately, the shallow 15 degree angle of the stereo planes in the HMS drift chamber design greatly limits the precision of this capability. There

must be at least four wires separating genuine hits from noise hits on Y wires in order that the tracking algorithm function properly. For the remaining planes, the required separation is 2 wires.

If these conditions are not satisfied, the tracking algorithm either generates multiple spacepoints, or returns a single spacepoint constructed of a mix of noise and real hits. In the latter case, the reported track will not reproduce the real trajectory. In the former case, the algorithm will falsely identify multiple tracks. True multiple track events, two or more particles originating in the target arriving close enough in time to be recorded in a single event, are extremely rare. Occasionally, a single track will produce energetic secondary particles which leave genuine multiple tracks in the chambers. The algorithm most frequently returns multiple tracks, however, due to noise. Incidences of false spacepoints composed of mixtures of noise and real hits increase as the number of noise hits in a chamber increase; in this analysis, up to 20 hits per chamber were accepted. Any algorithm will suffer this flaw, to a greater or lesser degree, simply because there is fundamentally no way to distinguish real hits from noise hits. Every spacepoint must be treated as perfectly legitimate.

For an event to be unambiguously trackable, therefore, it is required that the algorithm recognize only one track among the pattern of hits, and that the hits of the track be isolated from any other hits by the spacing indicated above. This ensures that the track determined for the event corresponds to the primary particle, and that it accurately reflects the correct parameters of the trajectory.

4.2.3 Count density

From the events observed in a particular momentum bin i it is necessary to determine the count density at the central values θ_c and E'_i of the bin. The simplest estimate of the count density at the center of the bin is the ratio $N/\Delta E'_i \Delta \Omega_i$ of the total number of events N found in the bin to the total volume of phase space $\Delta E'_i \Delta \Omega_i$ of the bin. This estimate is valid only when the event distribution either is completely flat in E' and θ, or varies at most linearly *and* the accepted volume of phase space is symmetric about the center of the bin. If a second or higher order expansion is required to adequately describe the shape of the event distribution, a more sophisticated analysis is necessary to correctly extract the count density at the center of the bin.

Figure 4.17 illustrates the problem in θ. (For notational convenience, θ and $\theta - \theta_c$ will be used interchangably.) The left panel shows the reconstructed distribution of events across the octagonal entrance slit of the HMS. On the right, the red histogram in θ contains the effect of both the acceptance of the slit and the shape of the cross section; taking a rectangular cut in θ and ϕ (magenta) inside the acceptance isolates the cross section and reveals a quadratic angular dependence. The concentration of events at $\theta < \theta_c$ due to the combined effect of the acceptance and the cross section skews the simple average $N/\Delta \Omega_i$ so that it does not represent the count density at the central angle.

The following describes the procedure used in this analysis to measure the count
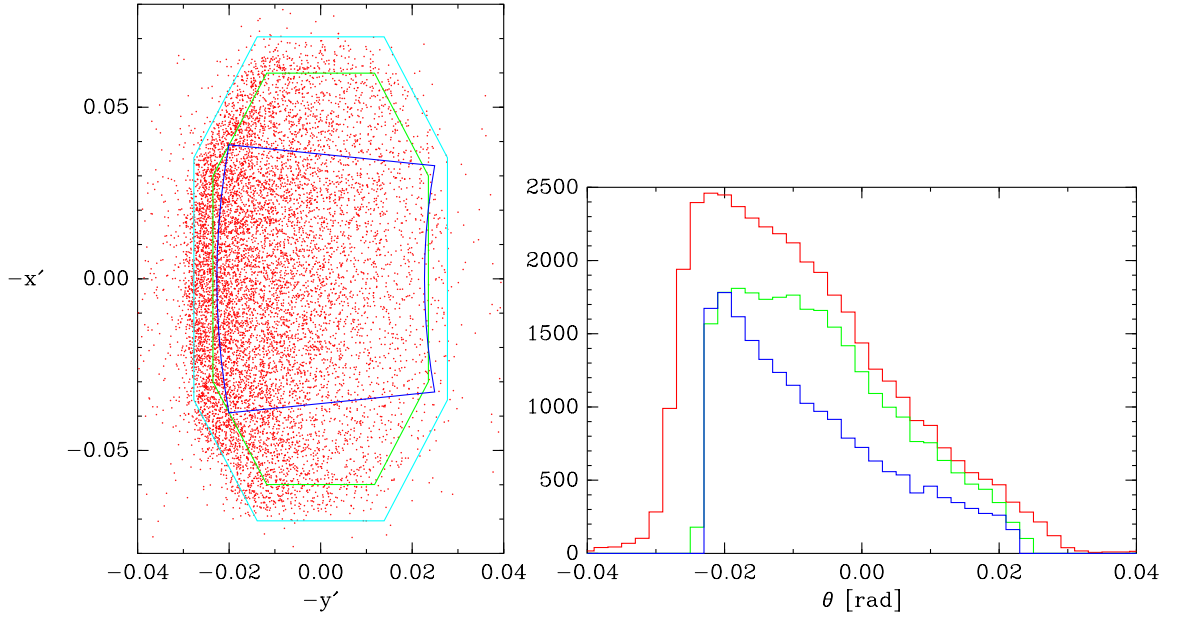
Figure 4.17: The reconstructed event distribution across the octagonal HMS entrance slit (left) and the corresponding histograms in θ (right). The blue rectangular cut in θ and ϕ (appearing as a sector in x' and y') isolates the quadratic angular dependence of the cross section.

density at the central angle. If the angular dependence of the distribution is expanded about the central angle as $a_0 + a_1\theta + a_2\theta^2 + \cdots$ then the leading term a_0 is exactly the count density at the central angle. Using this expansion, the expectation values of the moments of the angular distribution are:

$$
\begin{aligned}
M_0 &= a_0 \int_A \theta^0 \, d\Omega + a_1 \int_A \theta^1 \, d\Omega + a_2 \int_A \theta^2 \, d\Omega + \ldots \\
M_1 &= a_0 \int_A \theta^1 \, d\Omega + a_1 \int_A \theta^2 \, d\Omega + a_2 \int_A \theta^3 \, d\Omega + \ldots \\
M_2 &= a_0 \int_A \theta^2 \, d\Omega + a_1 \int_A \theta^3 \, d\Omega + a_2 \int_A \theta^4 \, d\Omega + \ldots \\
&\vdots
\end{aligned}
$$

The two dimensional integrals involved in this expression are purely geometric quantities characteristic of the accepted phase space volume A of the bin, and can be computed given a suitable model of the spectrometer. Truncation of this expansion at some finite order produces a set of linear equations which can readily be inverted; this means that the count density a_0 can be expressed as a linear combination of the moments of the angular distribution:

$$\frac{dN}{d\Omega} \equiv a_0 = \sum c_{0i} M_i$$

where the c_{0i} are elements of the inverse matrix. Since $M_0 \equiv N$ and $\int_A d\Omega \equiv \Delta\Omega$ by definition, this method clearly reduces to the simple average $a_0 = N/\Delta\Omega$ when the distribution is completely flat (truncation at lowest order). The error is also easily obtained:

$$\begin{aligned} (\Delta a_0)^2 &= \left(\langle a_0^2 \rangle - \langle a_0 \rangle^2 \right) + \frac{1}{N} \langle a_0 \rangle^2 \\ &= \sum_{i,j} c_{0i} c_{0j} M_{i+j} \end{aligned}$$

where the effect of the statistical fluctuation of the number of events N observed been added in quadrature. Although this discussion has focused on the angular dependence, the method can be extended in a straightforward manner to include momentum dependence across the bin as well as any cross dependence.

Therefore, a measurement of the count density at the central angle of each bin can be performed using the moments $M_i = \sum_{j=1}^{N} \theta_j^i$ of the observed distribution in θ and a set of coefficients characteristic of the solid angle. The distortions in the reconstruction, indicated in the previous section, inspired a lack of confidence in the internal consistency of any spectrometer model used to calculate these coefficients. To eliminate completely any model dependence, therefore, the (possibly poor) decision was made to create a well defined artificial aperture by applying an octagonal cut just inside the expected boundary of the physical aperture, as illustrated by the green octagon in Figure 4.17. The trade-off is that this cut omits approximately 30% of the events in each bin, which corresponds to a modest 20% increase in the statistical error.

The top panels of Figure 4.18 indicate the magnitude of the effect for the 15 and 23 degree data from the ^{12}C targets. These figures show the ratio of the count density determined from the procedure described above to the simple estimate given by the ratio of the total number of counts to the solid angle. The size of this effect progressively decreases for the other spectrometer angles. As indicated in the lower two panels, the completely analogous examination of the momentum dependence revealed no statistically significant deviation from the simple average $N/\Delta E'$. Although the E' dependence is certainly very steep, the curvature across the width of the bins is insufficient to produce any sizeable effect, and a linear dependence alone cannot skew the average away from the center of the bin due to symmetry.
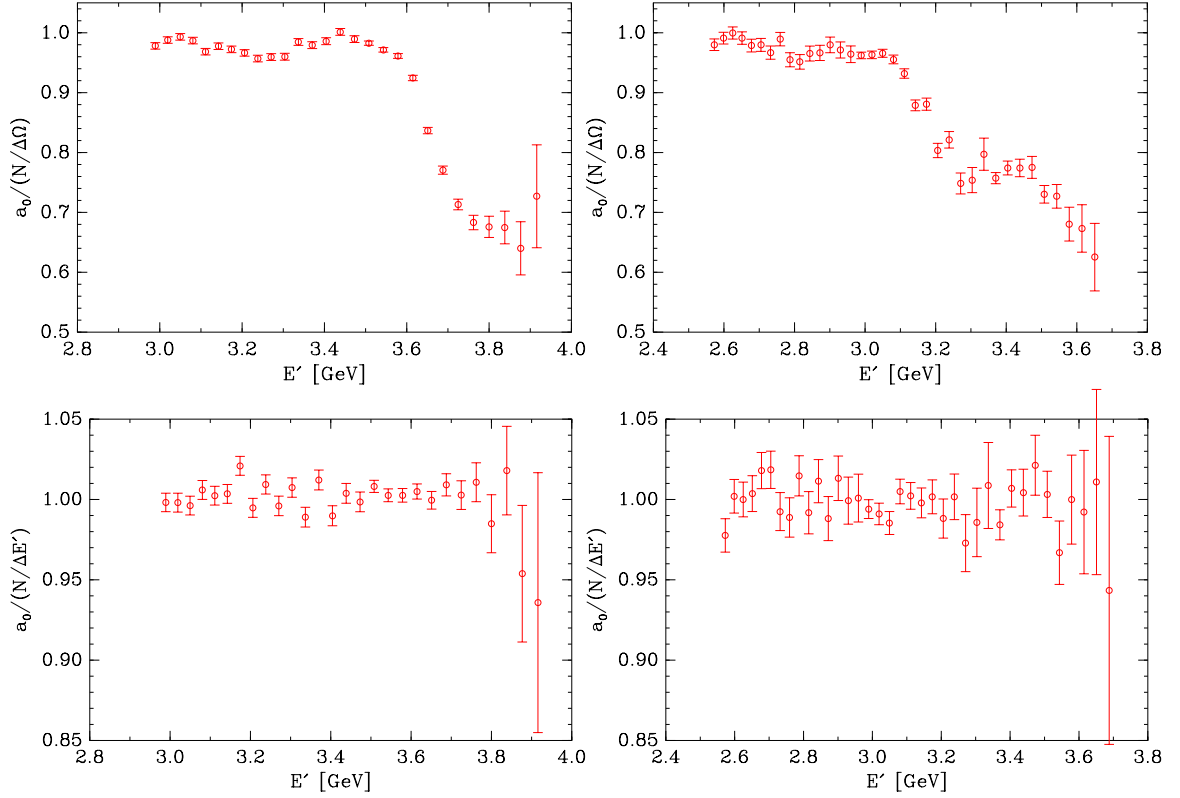
Figure 4.18: The top panels show the ratio of the measured count density a_0 at the central angle to the simple estimate $N/\Delta\Omega$ (the ratio of the total number of counts to the solid angle) for the 15 (left) and 23 degree data (right) from ^{12}C. The bottom two panels indicate the absence of any statistically significant effect coming from the momentum dependence.

4.2.4   Charge symmetric background

Electrons produced in charge symmetric processes are the dominant background for this experiment. These backgrounds are easily measured by setting the spectrometer to positive polarity to detect the positrons instead. Unfortunately, the positive polarity runs suffered from a myriad of problems. The majority of the data was taken at settings where the background contribution was small. For the only measurement where the background was significant (at 55 degrees), the dipole setting was incon-

sistent with the quadrupole settings; these measurements therefore could not be used to perform the subtraction.

An alternate solution was contrived to attempt a rescue of the situation. The dominant charge symmetric process is the conversion into e^+e^- pairs of one (or both) of the high energy photons coming from the decay of neutral pions produced in the target, $\pi^0 \rightarrow 2\gamma$. Studies of particle multiplicities in hadronic reactions at large transverse momenta indicate that $\pi^\pm$ and π^0 are produced in roughly fixed proportion to one another. If this is true, then:

$$
\begin{aligned}
N(e^\pm) &= (1 - e^{-w/\lambda})N(\gamma) \\
&\approx \frac{w}{\lambda}N(\gamma) \\
&\propto N(\pi^0) \propto N(\pi^+) \propto N(\pi^-)
\end{aligned}
$$

where $\lambda \equiv 9/7 X_0$ is the photon attenuation coefficient [81] in terms of the radiation length X_0 and w is the total thickness of material from the center of the target to the spectrometer entrance. The first line characterizes the likelihood the photons are converted to e^+e^- pairs, and the last line expresses the hoped proportionality among the pion production rates. Since π^- data is collected along with the scattered electrons during the usual negative polarity running, the idea is to estimate the charge symmetric e^- background as $\kappa w/\lambda$ times the measured π^- yields, where κ is the as yet undetermined proportionality constant.

θ_c	p_c [GeV]	target	θ_T	w/λ	$N(e^+)$	$N(\pi^+)$	κ
37	1.730	6% Fe	20	0.0506	2057	13356	3.0 ± 0.1
55	1.402	2% C	0	0.0213	91	1216	3.5 ± 0.4
55	1.402	2% Fe	0	0.0181	42	632	3.6 ± 0.6
55	1.402	6% Fe	0	0.0484	90	627	3.0 ± 0.3

Table 4.3: Results for the positive polarity runs. The target angle θ_T and spectrometer angle are in degrees. See the text for the definition of κ.

Table 4.3 indicates the data from all but one of the positive polarity runs. The run not listed, at 45 degrees and 1.730 GeV on the gold target, was taken with the trigger modified to require both ELLO and ELHI, which severely suppressed the π^+ yield, and could not be compared with the others. The last column indicates the ratio $\kappa \equiv N(e^+)/(w/\lambda)/N(\pi^+)$ which, according to the previous argument, should be constant. Although the statistics are poor, it does appear to be constant within error for these two settings and targets. It should be noted that since only the ratios are of interest here, the improper magnet setting for the 55 degree data should not affect the results.

As an additional check to these assumptions, the normalized π^- yields from the complementary negative polarity runs were confirmed to match the normalized π^+ yields. A similar cross check was possible with the 45 degree run not listed. The π^- yield from the negative polarity run at 45 degrees and 1.730 GeV was used to estimate the π^+ yield which should have been observed had the trigger not been modified; then, using the average value of κ, the e^+ yield was indeed correctly predicted.

All of these checks seem to validate the proposal to estimate the charge symmetric
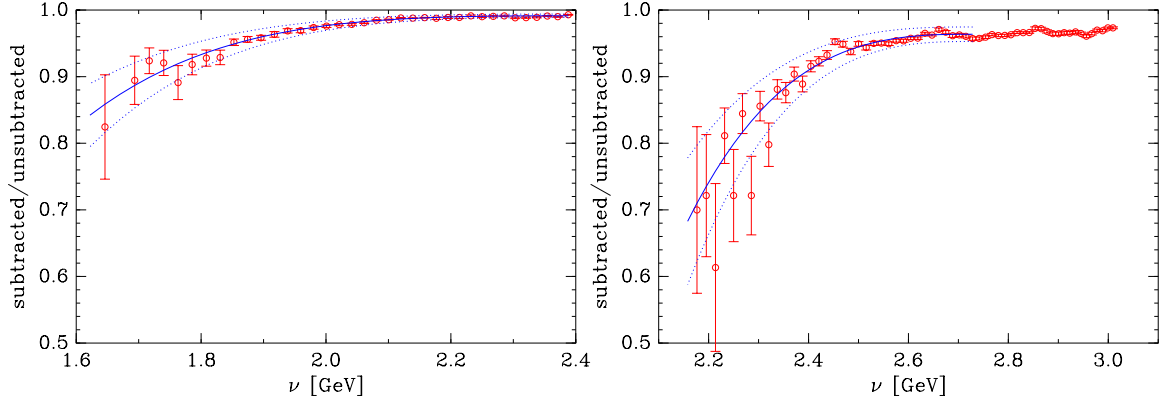
Figure 4.19: Charge symmetric correction for the thick iron target at spectrometer angles of 45 degrees (left) and 55 degrees (right).

e^- background with $\kappa w/\lambda$ times the π^- yields. Figure 4.19 shows the ratio of the corrected to uncorrected electron yields for the thick iron target at 45 and 55 degrees. Instead of using these subtracted results, the fit indicated in the figures is applied as a correction factor to the data. The dotted lines indicate a systematic uncertainty of 30% added to account for the variation of κ listed in Table 4.3. For all targets, the correction is significant only for the 45 and 55 degree data sets, and has a similar overall shape for all targets. For the thick carbon target, the correction is at most 1% at 45 degrees and 4% at 55 degrees; for the gold target, the correction is at most 6% at both 45 and 55 degrees.

4.2.5 Radiative corrections

Radiative corrections account for the additional amplitudes beyond the first order Born approximation for the hard scattering event (internal corrections), and for the

energy loss of the incident and scattered electron as they pass through the target material (external corrections). To the next order in $\alpha \approx 1/137$, the vertex and vacuum polarization corrections, which are purely quantum field effects, as well as the effect of the radiation of photons (bremsstrahlung) constitute the internal correction. Both bremsstrahlung as well as ionization energy loss in the bulk of the target material, properly corrected for multiple soft photon emissions, are accounted for in the external correction. A thorough treatment of these corrections is described in a series of publications by Y. Tsai [88, 89, 90, 91].

The internal and external bremsstrahlung part of the correction are lumped together under the equivalent radiator approximation, which assumes that they share the same spectrum. Rather than compute a double integral over all lower beam energies and higher scattered energies, the peaked nature of bremsstrahlung is used to estimate the contribution as the sum of two integrals, one representing the radiation of photons by only the incident electron and one representing the radiation of photons by only the scattered electron.

Since these integrands contain the product of the bremsstrahlung spectrum and the Born approximation cross section, two difficulties arise. First, the Born approximation cross sections can be known only after the radiative corrections have been applied to the measured experimental cross sections. To handle this circular condition, an iterative approach [92], originally introduced during the early SLAC experiments, was used. The radiative correction is initially computed using the uncorrected ex-
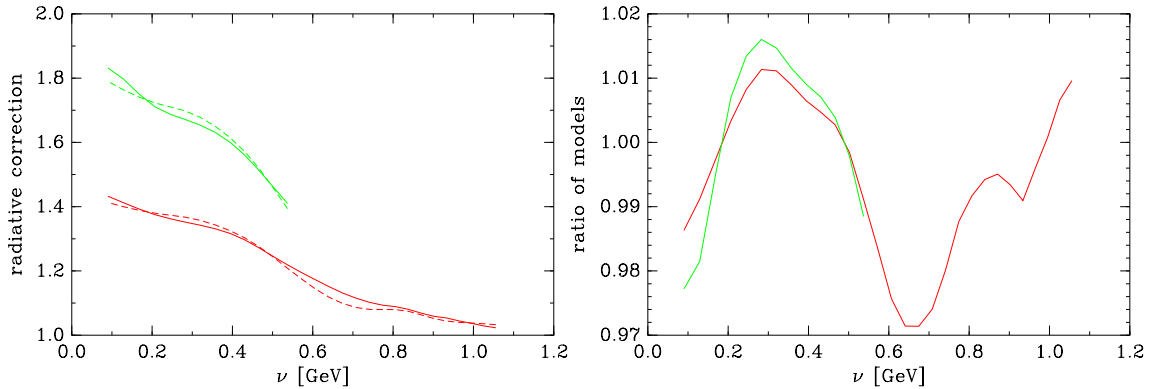
Figure 4.20: Radiative correction factor at 15 degrees for the thin (red) and thick (green) ^{56}Fe targets. See the text for details.

perimental data. This correction is applied to the data and the radiative correction is recomputed; as this process repeats, the radiative correction factor converges to a stable value, usually within four iterations.

The second difficulty arises from the fact that no cross section measurements are made at lower beam energy, so the contribution to the radiative correction from the integral due to bremsstrahlung of the incident electron cannot be performed in the same way as the integral at higher scattered electron energy. The values of the cross section needed for the calculation of this integral are computed by interpolation at fixed y using a database of previous measurements of $F(y, |\mathbf{q}|)$, seeded initially with the results of the SLAC experiment NE3. Simple exponential fits to the values of $F(y, |\mathbf{q}|)$ for each spectra in the database are used when extrapolation is necessary.

The radiative corrections are applied to the data sets in order of increasing spectrometer angle. In succession, the corrected cross sections are added to the database to assist the interpolation required for the next angle; similarly, for a given angle, the

b		α	γ	β
15.40	$[(\mathrm{GeV/c})^{-1}]$	0.598	1.272	4.203

Table 4.4: Model parameters for estimation of the radiative correction systematic uncertainty.

data points are corrected in the order of decreasing E'. Figure 4.20 illustrates the radiative correction factor obtained from this procedure at 15 degrees for the thin (red) and thick (green) $^{56}\mathrm{Fe}$ targets. In the left panel, the solid lines indicate the radiative correction obtained from the iterative interpolation procedure, and the dotted lines indicate the radiative correction as computed without iteration from a crude model based on exact scaling in y for the quasielastic and exact scaling in x for the inelastic:

$$F(y) \; = \; \frac{b}{4}\left(1 + b|y|\right)e^{-b|y|}$$

$$F_2(x) \; = \; \begin{cases} \alpha\sqrt{x}\,(\gamma - x)^\beta & x < \gamma \\ 0 & x \geq \gamma \end{cases}$$

where the parameters are indicated in Table 4.4. The right panel of Figure 4.20 shows the ratio of the two calculations, indicating approximately 3% systematic uncertainty in the correction. Comparisons for the results at other angles also indicate that these two calculations for the radiative correction factor fall within a $\pm 3\%$ band. The model differs by as much as a factor of 5 from the data and, unlike the interpolated cross sections, contains none of the Q^2 dependence. Although not rigorous, such comparisons
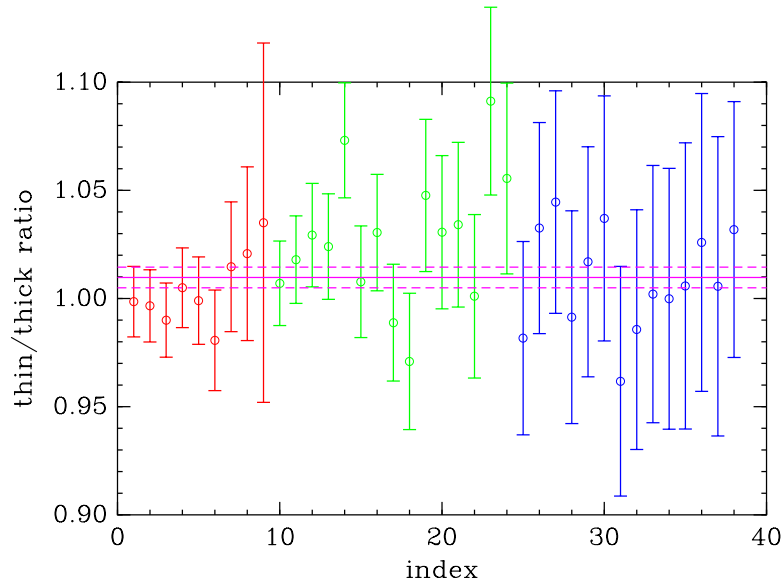
Figure 4.21: The ratio of the cross sections computed for the thin and thick ^{56}Fe targets. The red, green, and blue data points correspond to 15, 30, and 55 degree data. See the text for details.

therefore offer a fairly conservative estimate of the systematic uncertainty.

Figure 4.21 indicates the ratio of the cross sections for the thin and thick ^{56}Fe targets. The red, green, and blue data points correspond to 15, 30, and 55 degree data. The average of all the data yields 1.010±0.005; each set averages separately to 0.998±0.007, 1.022±0.007, and 1.008±0.015. These ratios are consistent with the ≈ 1% uncertainty in the target thicknesses and the estimated 3% systematic uncertainty in the radiative correction.

Chapter 5

Results

The experimental cross sections are the final product of the data reduction described in the previous chapter. Figure 5.1 displays these results. From left to right, the data sets within each panel correspond to the scattering angles 15, 23, 30, 37, 45, and 55 degrees. The following sections provide an examination of the quasielastic and inelastic contributions to the cross sections and their derived structure functions. It is observed that the quasielastic function $F(y, |\mathbf{q}|)$ becomes independent of $|\mathbf{q}|$ out to $y \approx -0.4$ GeV/c. The structure function F_2^A largely scales in the Bjorken variable x when the quasielastic contribution is removed. In contrast, it is shown that the scaling behavior of F_2^A in the Nachtmann variable ξ requires cooperation of both the inelastic and the quasielastic contributions. Throughout, these results are compared against calculations using the quasifree approximation and the model spectral function described in Chapter 2.
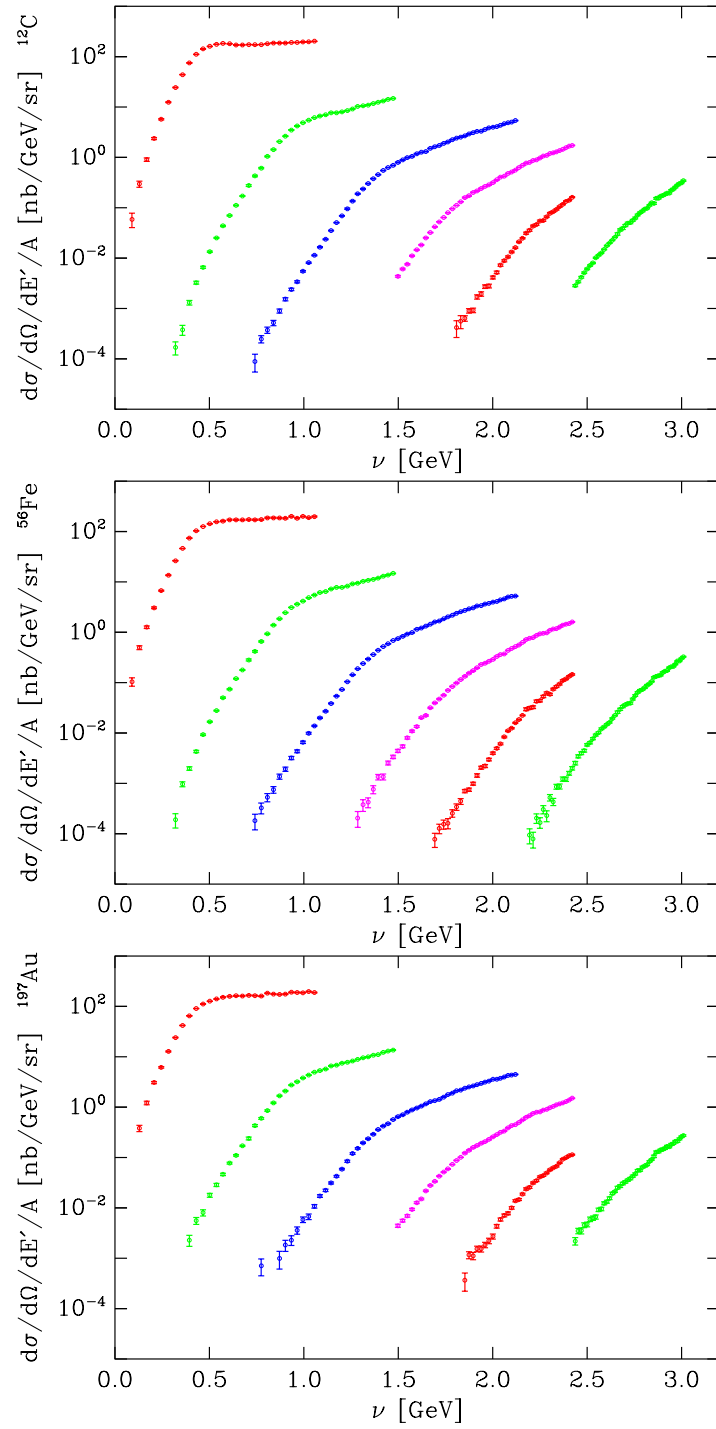
Figure 5.1: Experimental cross sections per nucleon.

5.1   Quasifree model comparison

Figure 5.2 compares the experimental cross sections for ^{12}C at 15, 30, and 55 degrees with the results of the calculations using the quasifree reaction and the model spectral function described in Chapter 2. The results for the other targets and angles are similar. In this figure, the solid lines indicate the sum of the quasielastic and inelastic contributions. Both of these contributions consist of two parts, corresponding to the division of the model spectral function into independent particle (dashed) and correlation (dotted) components.

For all angles, the calculation falls short of the data on the small energy loss side of the quasielastic peak. This is evident in the 15 and 30 degree data; the 55 degree data do not extend to small enough ν for this discrepancy to appear. The low ν region is clearly dominated by the quasielastic contribution from the correlation component of the model spectral function. Although it possibly indicates inaccuracy of the correlation calculation, this underestimate of the data is usually ascribed to the neglect of final state interactions in the quasifree approximation. More sophisticated calculations [40, 93] which include the final state interactions better reproduce the cross sections on the low energy loss side of the quasielastic peak. This is also supported by the y-scaling analysis presented in the following sections.

On the high energy loss side of the quasielastic peak, the inelastic contribution from the independent particle component of the model spectral function dominates

$d\sigma/d\Omega/dE'$ [nb/sr/GeV]

$\theta = 15°$

$\theta = 30°$

$\theta = 55°$

ν [GeV]
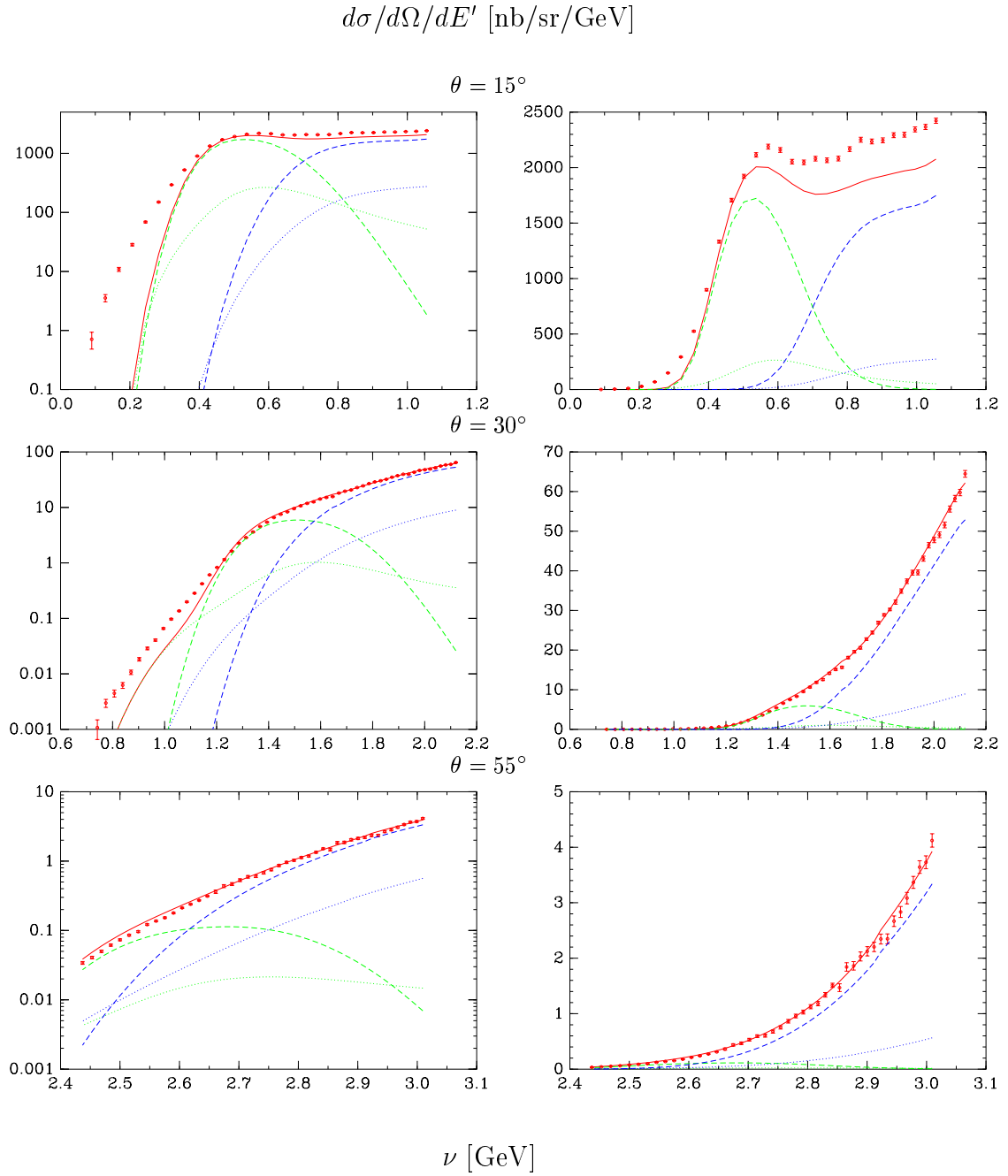
Figure 5.2: Experimental and calculated cross sections for ^{12}C. The left and right panels show the same data on logarithmic and linear axes. See the text for details.

the response. While the calculation agrees with the data at 30 and 55 degrees, the comparison at 15 degrees shows that the calculation underestimates the data. This problem is endemic to most calculations at low $|\mathbf{q}|$; possible explanations include inadequate representation of the missing energy continuum near the quasielastic peak, or contributions from additional reaction mechanisms such as meson exchange and isobar excitations, as discussed in the Introduction. It is worthwhile to note that the Δ excitation of the nucleon is evident in the 15 degree data.

5.2 Quasielastic contribution

The dependence of the quasielastic function $F(y, |\mathbf{q}|)$ on the scaling variable y most effectively isolates the nuclear dynamics responsible for the quasielastic contributions to the inclusive cross section. Equation (2.34) indicates that $F(y, |\mathbf{q}|)$ may be extracted from the measured cross sections $\sigma^{\mathrm{exp}} \equiv d\sigma/d\Omega/dE'$ according to:

$$F(y, |\mathbf{q}|) = \frac{\sigma^{\mathrm{exp}}}{Z\tilde{\sigma}_p + N\tilde{\sigma}_n} \cdot \frac{|\mathbf{q}|}{\sqrt{M^2 + (y + |\mathbf{q}|)^2}} \tag{5.1}$$

where $\tilde{\sigma}_{p,n}$ are the off-shell elastic cross sections for protons and neutrons. For the calculation of y given by equation (2.33), the values of $E_{\mathrm{min}} \equiv M_{A-1} + M - M_A$ used are 16.0 MeV, 8.7 MeV, and 7.8 MeV for ^{12}C, ^{56}Fe, and ^{197}Au, respectively. Figure 5.3 displays the experimental $F(y, |\mathbf{q}|)$ obtained in this manner.
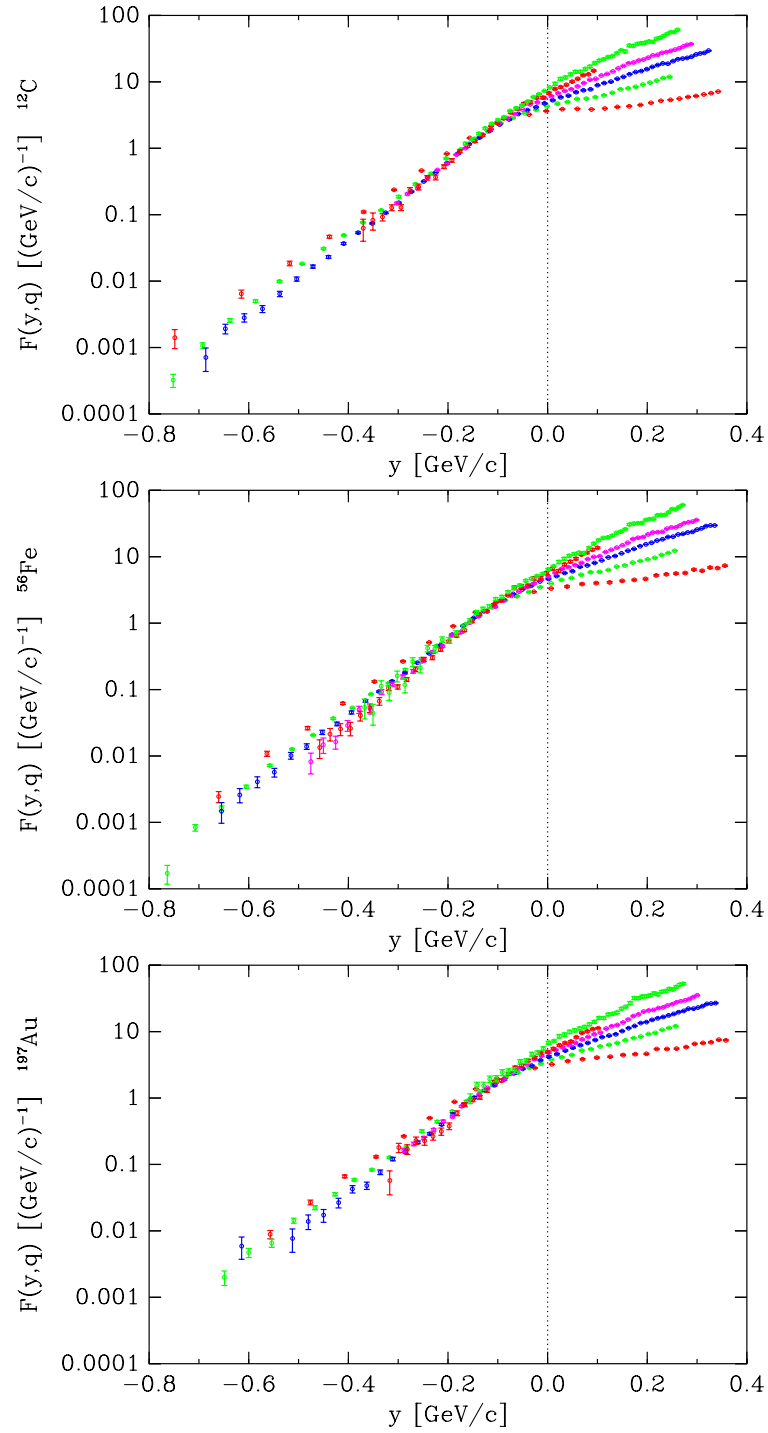
Figure 5.3: Experimental quasielastic functions $F(y, |\mathbf{q}|)$.

Figure 5.4 examines the y-scaling behavior of $F(y, |\mathbf{q}|)$ for ^{56}Fe in greater detail. The results for the other targets are similar. This figure displays the dependence of $F(y, |\mathbf{q}|)$ on $|\mathbf{q}|$ at six fixed values of y from 0 GeV/c to -0.5 GeV/c. In each panel, the model calculations for the quasielastic (green dashed), inelastic (blue dashed), and total (red solid) contributions are indicated. Along with the data from this experiment (solid circles), this figure includes data from previous experiments at lower $|\mathbf{q}|$; open circles indicate data from the SLAC NE3 experiment [16], and crosses indicate various other SLAC measurements [94, 15, 95].

The scaling violation at small y is evidently due to the rising inelastic contribution. At $y = -0.2$ GeV/c and $y = -0.3$ GeV/c, the data have clearly reached the scaling limit; scaling appears to have just set in for $y = -0.4$ GeV/c. No definitive statement can be made for $y = -0.5$ GeV/c. The approach to the scaling limit from above as indicated by the data contrasts with the results of the quasifree calculation, which predicts that scaling should come from below. As mentioned in the previous section, the final state interactions included in more sophisticated calculations account for this contrary approach to the scaling limit.

One of the original motivations for studying y-scaling was the possibility of utilizing these measurements of the quasielastic function that have reached the scaling limit $F(y) \equiv F(y, |\mathbf{q}| \to \infty)$ to obtain the nucleon momentum distribution $n(p)$. These two quantities are related by an integral equation with a correction due to the

$F(y, |\mathbf{q}|) \, [(\mathrm{GeV/c})^{-1}]$
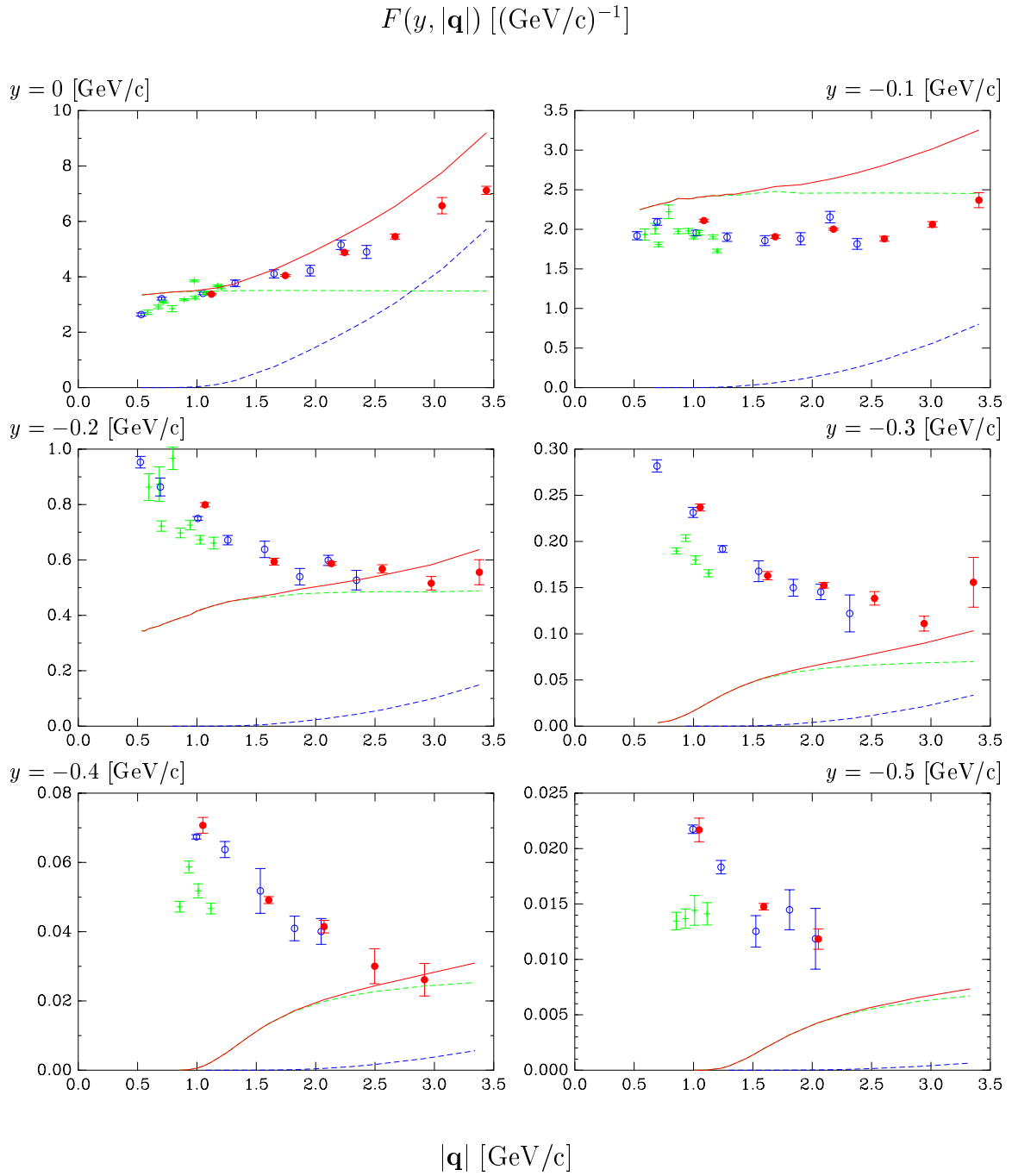
Figure 5.4: Convergence of $F(y, |\mathbf{q}|)$ in $|\mathbf{q}|$ for ^{56}Fe. See the text for details.

missing energy dependence of the spectral function, as indicated in equation (2.36):

$$F(y) = 2\pi \int_{|y|}^{\infty} n(p)\, p\, dp \, - \, B(y) \qquad (5.2)$$

The binding correction must be computed from the model spectral function, and therefore is a source of theoretical uncertainty in the extraction of the momentum distribution. $B(y)$ is small for moderate values of $|y|$. At large $|y|$, unfortunately, the binding correction is very large and severely spoils the connection between $F(y)$ and $n(p)$, exactly where it might be hoped to learn about the correlation part of the nucleon momentum distribution.

The top left panel of Figure 5.5 indicates this important difference between the scaling function $f(y) \equiv 2\pi \int_{|y|}^{\infty} n(p)\, p\, dp$ originating from the momentum distribution alone (dashed), and the quasielastic function $F(y)$ observable in the scaling limit (solid), as computed from the model spectral function for ^{12}C. Evidently, a significant portion of the high momentum components are simply not accessible to inclusive electron scattering experiments. To emphasize this point further, the top right panel explicitly shows the binding correction $B(y, |\mathbf{q}|)$ for each data set. In order to reveal the shape of the quasielastic peak for $y > 0$, the inelastic contribution calculated with the quasifree model has been subtracted from the ^{12}C data displayed in these graphs; only data for which the inelastic calculation amounted to less than 30% of the total are retained.
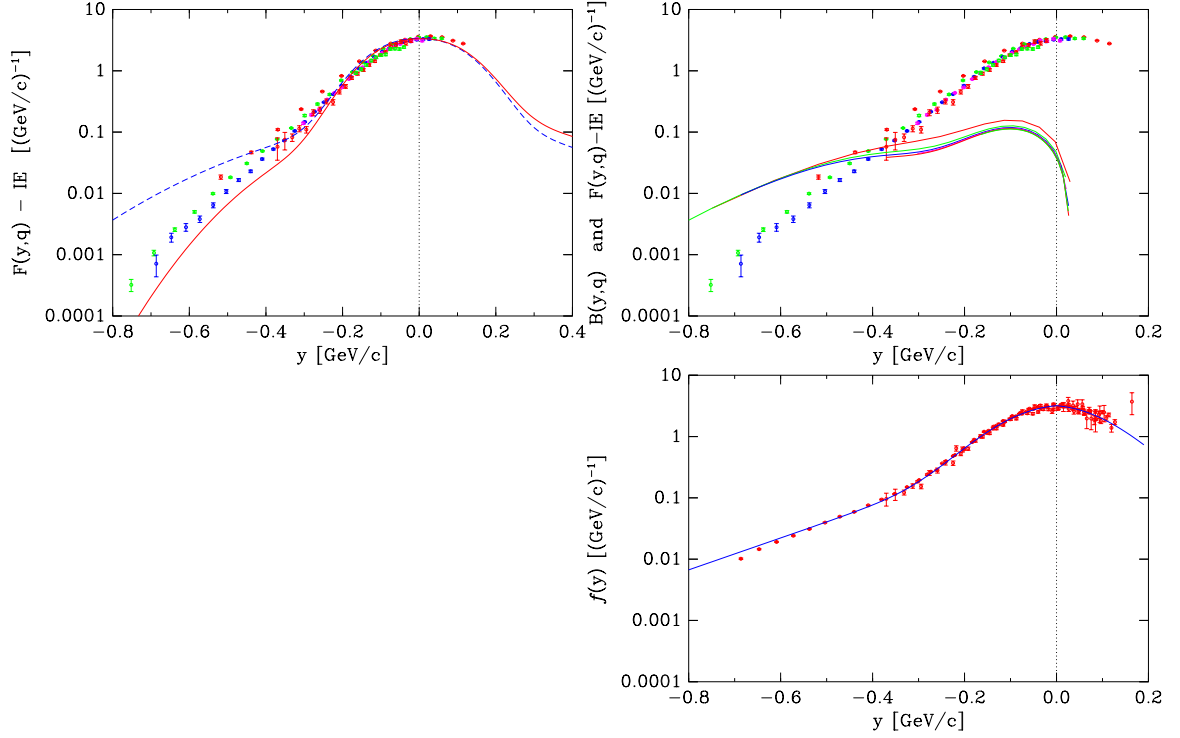
Figure 5.5: Experimental $F(y, |\mathbf{q}|)$ for ^{12}C with the inelastic contribution removed and the computed effects of the binding correction. See the text for details.

The dominance of the binding correction seems to have been ignored by Ciofi and West in their recent phenomenologically motivated parameterization [96] for $f(y)$:

$$f(y) = A\frac{e^{-ay^2}}{\alpha^2 + y^2} + Be^{-b|y|} \qquad (5.3)$$

A, a, α, B, and b are all free parameters; the two terms correspond to the independent particle and correlation parts of the momentum distribution. The lower right panel of Figure 5.5 reproduces this fit to the sum of the experimental $F(y, |\mathbf{q}|)$ and the model calculation of $B(y, |\mathbf{q}|)$. Observing that the parameter b in the correlation
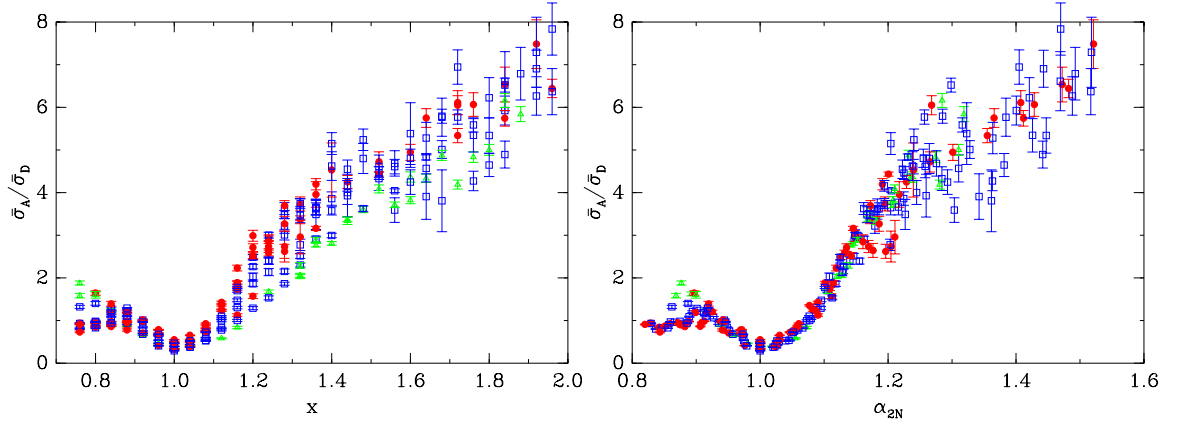
Figure 5.6: Ratio $\bar{\sigma}_A/\bar{\sigma}_D$ for ^{56}Fe as a function of the Bjorken variable x and of the two-nucleon correlation variable α_{2N}.

term attains a common value for deuterium, ^{4}He, and ^{56}Fe as well as for ^{12}C, Ciofi and West conclude that the correlations have a universal behavior independent of the nuclear environment. However, this conclusion suffers from circular logic: b is clearly determined entirely by the large negative y behavior of $B(y)$ computed from the model spectral function which *assumes* a universal correlation momentum distribution.

The ratios $\bar{\sigma}_A/\bar{\sigma}_D$ of the cross sections per nucleon for complex nuclei to the deuteron might afford an alternate means of studying the high momentum components. In the first examination of these ratios at $x > 1$, Frankfurt *et. al.* [97] suggested that if short range correlated nucleon pairs generate the high momentum components then the ratios should reach a plateau beyond $x \approx 1.5$ and scale in the lightcone variable α_{2N} defined by:

$$\alpha_{2N} = 2 - \frac{\nu - |\mathbf{q}| + 2M}{2M}\left(1 + \frac{\sqrt{W_{2N}^2 - 4M^2}}{W_{2N}^2}\right)$$

where $W_{2N}^2 = (2M + \nu)^2 - |\mathbf{q}|^2$ is the invariant mass of a two nucleon system initially at rest. Figure 5.6 indicates the cross section ratios for ^{56}Fe data both from this experiment and from NE3; the deuteron cross sections needed to compute the ratios were determined by the same interpolation method on the same body of world deuteron data [13, 14] as in the original study [97]. Although these ratios do seem to converge better in α_{2N} than in x, no plateau is evident.

5.3   Inelastic contribution

The inelastic contribution to the cross section is best studied through the structure function $F_2^A \equiv \nu W_2^A$. However, since the cross section also depends upon W_1^A, an assumption must be made in order to isolate F_2^A from the cross section. The necessary assumption is the smallness of the ratio R of the longitudinal to the transverse cross section, which is related to the ratio of the structure functions according to:

$$\frac{W_1}{W_2} = \frac{1 + \nu^2/Q^2}{1 + R} \tag{5.4}$$

Using this relation and equation (2.11), F_2^A can be expressed in terms of R:

$$F_2^A = \nu \cdot \frac{\sigma^{\mathrm{exp}}}{\sigma_{\mathrm{M}}} \left[1 + 2\tan^2(\theta/2) \cdot \left(\frac{1 + \nu^2/Q^2}{1 + R} \right) \right]^{-1} \tag{5.5}$$

R has not been measured in the kinematic range of this experiment. However, there are measurements [98] of R for the inelastic response of the free proton and of the deuteron at $x < 1$ which have been parameterized to vary as $\approx 0.5/Q^2$, with Q^2 in units of GeV^2. Since this is consistent with the value expected from the quasielastic response, as determined by the elastic form factors, it is adopted for the present analysis. Figure 5.7 displays structure function per nucleon $\bar{F}_2^A$ as a function of the Bjorken variable x and of the Nachtmann variable ξ.

Bjorken scaling

The $\bar{F}_2^A$ data shown in Figure 5.7 clearly do not scale in the Bjorken variable x. While there does appear to be some hint of convergence setting in for $x < 1$, the quasielastic contribution dominates the $x > 1$ region and produces the severe Q^2 dependence seen in $\bar{F}_2^A$. To examine the inelastic contribution, it is necessary to remove the quasielastic using the quasifree model calculation. The result for ^{12}C is displayed in Figure 5.8; only data for which the quasielastic calculation amounted to less than 30% of the total are retained. In line with the parton model expectations, the remaining inelastic contribution does indeed exhibit much better scaling in x.

Figure 5.8 also illustrates the parton recombination modification computed for $Q_0^2 = 1$ GeV^2. There is clear disagreement in the vicinity of $x = 1$ where the modification begins to dominate, and the calculation and the data appear to cross near $x \approx 1.15$. However, it is important to note that the choice of $Q_0^2 = 1$ GeV^2 is
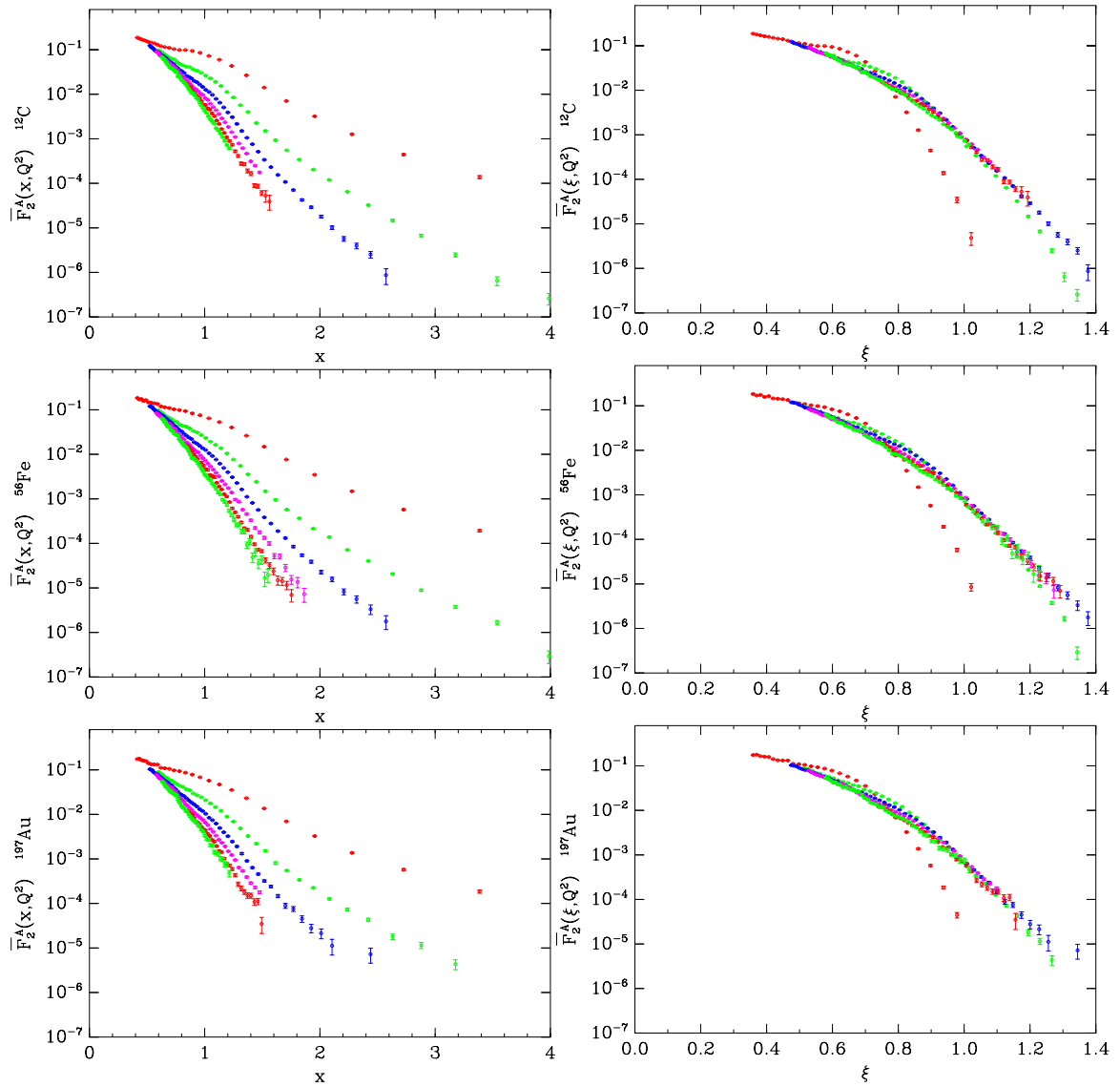
Figure 5.7: Structure function per nucleon $\bar{F}_2^A$ as a function of the Bjorken variable x and the Nachtmann variable ξ.
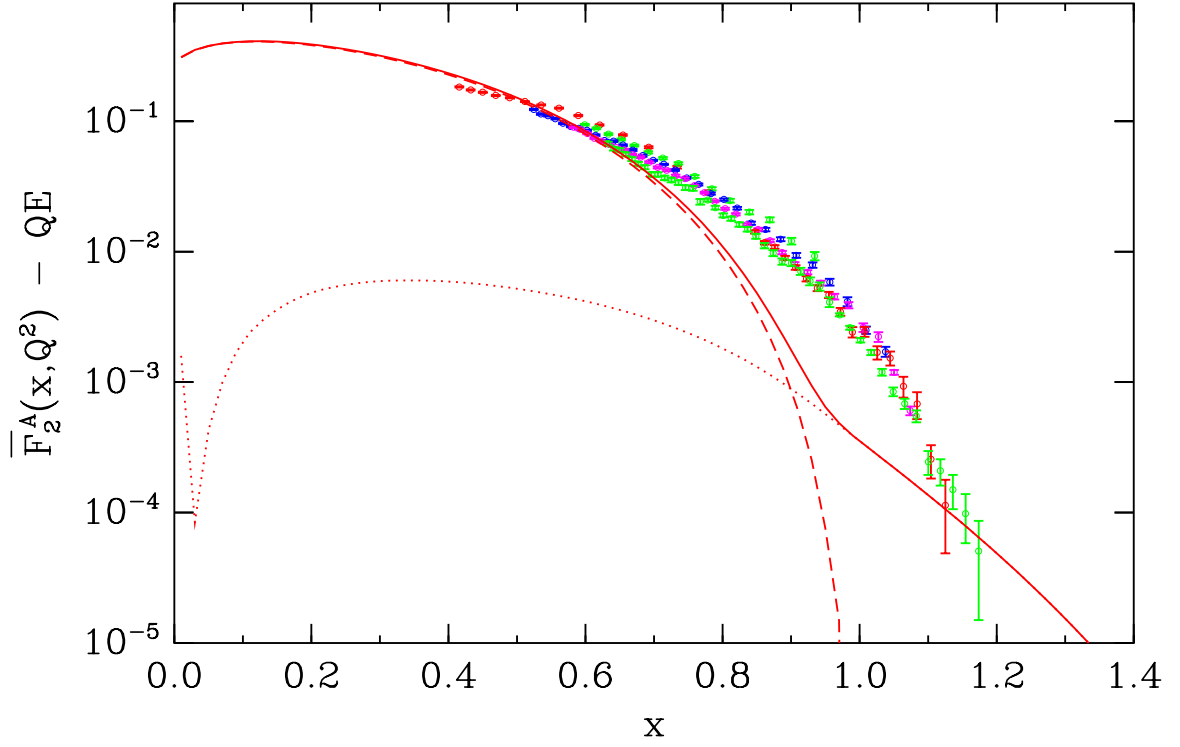
Figure 5.8: The inelastic contribution to $\bar{F}_2(x, Q^2)$ and a calculation of the parton recombination modification (dotted) for $Q_0^2 = 1$ GeV^2. The dashed line indicates the free nucleon structure function.

arbitrary, and the inverse power of Q^2 in the calculation (see equation 2.28) suppresses the modification for larger choices of Q_0^2. While these results do not verify initial state parton recombination, they also do not exclude recombination as a possible contributing mechanism to the structure at $x > 1$. It would be interesting to test the radiative recombination additions to the evolution equations against the residual Q^2 dependence of these data.
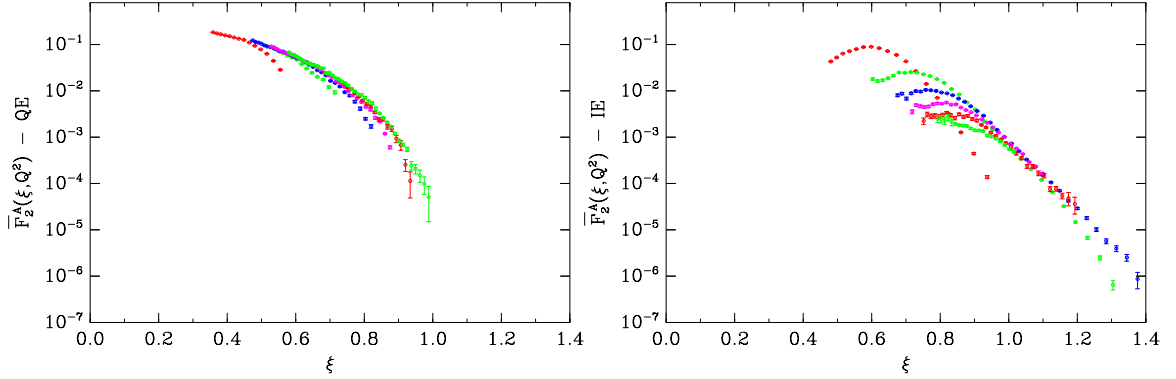
Figure 5.9: The inelastic (left) and quasielastic (right) contributions to $\bar{F}_2(\xi, Q^2)$.

Nachtmann scaling

The panels on the right in Figure 5.7 show the dependence of the structure function per nucleon $\bar{F}_2^A$ on the Nachtmann variable ξ defined by equation (2.27). The Nachtmann variable absorbs a far greater amount of the Q^2 dependence of $\bar{F}_2^A$ than does the Bjorken variable, even in the quasielastic region; this scaling behavior was first pointed out [99] in the data from SLAC experiment NE3. Unlike the improvement to Bjorken scaling, the scaling in ξ is somewhat degraded when the quasielastic contribution is removed from $\bar{F}_2^A$, as indicated for the ^{12}C data in the left panel of Figure 5.9. The right panel shows that the scaling is also spoiled when the inelastic contribution is removed. Evidently, the inelastic and quasielastic contributions cooperate to produce ξ scaling.

This behavior calls to mind the Drell-Yan-West [100, 101] relationship which connects the Q^2 dependence of the free proton Dirac elastic form factor with the shape of F_2^p near $x = 1$ in the Bjorken limit. For the dipole $1/Q^4$ behavior, this relation-

ship predicts $F_2^p \sim (1-x)^3$; in fact, a fit to the form $(1-\xi)^p$ for the data from the resonance region returns $p = 3.0$ within errors for each of ^{12}C, ^{56}Fe, and ^{197}Au. That this behavior appears in ξ rather than x perhaps indicates that ξ is the appropriate variable to study parton model predictions at finite kinematics; as discussed in Chapter 2, such an interpretation follows from the free field lightcone derivation of the parton model and is bolstered by the role that ξ plays in isolating twist-two contributions to the operator product expansion [51].

Chapter 6

Conclusion

The inclusive nuclear cross sections measured in Experiment E89-008 at TJNAF verify and extend over a wider kinematic range the trends observed in previous measurements. The quasielastic function $F(y, |\mathbf{q}|)$ continues scale from above with increasing $|\mathbf{q}|$ on the low energy loss wing of the quasielastic peak out to $y \approx -0.4$ GeV/c. The structure function F_2^A exhibits the same kind of scaling behavior in the Nachtmann variable ξ as was previously observed in the NE3 data measured at SLAC. This scaling seems to require the cooperation of both the quasielastic and inelastic component of the inclusive response. The inelastic contribution to F_2^A shows approximate scaling in the Bjorken variable x, but these measurements do not extend far enough into the $x > 1$ region to make any conclusive comparisons with the parton recombination predictions.

As a whole, the inclusive measurements in the quasielastic region support the

qualitative picture of quasifree scattering from nucleons in motion within the nucleus. At the quasielastic peak, the results are consistent with independent particle (shell model) momentum distributions, and the strength of the response on the wings is consistent with the expectation that correlations should populate the high momentum components of the nuclear wavefunction. However, it is difficult to draw precise conclusions about nuclear dynamics from the inclusive data. Even the best calculations currently available for comparison [93] also must be considered more qualitative than quantitative. There are a variety of theoretical complications, including the lack of detailed spectral function calculations for finite nuclei and the treatment of final state interactions. It is not even clear that the nonrelativistic formalism of nuclear many body theory should be reliable very far beyond the quasielastic peak. Furthermore, the necessity of introducing offshell nucleon form factors is also indicative of unresolved inconsistencies embedded in the theoretical approach.

Independent of the theoretical difficulties, the quasielastic component of the inclusive response is simply too integrated to expose any deep insight into the nuclear dynamics; instead, exclusive measurements will be far more productive for exposing the dynamics responsible for the quasielastic response. The outstanding capability of TJNAF to perform such experiments will permit a thorough examination of the missing energy continuum using not only $(e, e'N)$ reactions, but also $(e, e'NN)$ reactions to specifically pick out the contribution from nucleons interacting at short range.

The Q^2 dependence of the inelastic channels is the most compelling motivation for

pursuing inclusive studies as higher beam energies become available at TJNAF. Just like the original deep inelastic studies, the dependence over a large range of Q^2 might provide direct insight into the interactions at the quark level of nuclear structure. Only with the improved understanding that both inclusive and exclusive studies undoubtedly will bring might it become possible to definitively identify effects beyond the range of traditional nuclear dynamics and the quasifree reaction mechanism.

Appendix A

Data Tables

The following set of tables list the measured cross sections for the 15, 23, 30, 37, 45, and 55 degree central angle settings of the HMS. The errors reported here are the statistical uncertainties added in quadrature to the systematic uncertainties arising from the charge measurement and the $e^{\pm}$ background correction, but do not include an overall 3% systematic uncertainty from target thickness and radiative corrections. These tables exclude data with errors exceeding 50%.

Cross sections for $\theta_c = 15°$

E' [GeV]	p	^{12}C σ [10^p nb/sr/GeV]	$\Delta\sigma$	p	^{56}Fe σ [10^p nb/sr/GeV]	$\Delta\sigma$	p	^{197}Au σ [10^p nb/sr/GeV]	$\Delta\sigma$
2.9892	3	2.4224	0.0235	4	1.1105	0.0287	4	3.7109	0.0748
3.0193	3	2.3664	0.0231	4	1.0549	0.0278	4	3.8859	0.0767
3.0496	3	2.3441	0.0229	4	1.1140	0.0287	4	3.6907	0.0749
3.0803	3	2.2967	0.0225	4	1.0323	0.0276	4	3.7191	0.0747
3.1112	3	2.2922	0.0225	4	1.1134	0.0285	4	3.7493	0.0749
3.1425	3	2.2455	0.0221	4	1.0245	0.0273	4	3.4692	0.0718
3.1741	3	2.2354	0.0220	4	1.0405	0.0274	4	3.4009	0.0711
3.2060	3	2.2510	0.0222	4	1.0508	0.0276	4	3.4787	0.0718
3.2382	3	2.1667	0.0216	4	1.0500	0.0274	4	3.6052	0.0732
3.2707	3	2.0811	0.0210	3	9.6453	0.2611	4	3.1543	0.0687
3.3036	3	2.0658	0.0209	3	9.6046	0.2595	4	3.2325	0.0694
3.3368	3	2.0803	0.0209	3	9.6393	0.2608	4	3.2679	0.0700
3.3703	3	2.0473	0.0207	3	9.4980	0.2583	4	3.1751	0.0693
3.4042	3	2.0534	0.0208	3	9.5688	0.2593	4	3.1910	0.0701
3.4384	3	2.1591	0.0216	3	9.5845	0.2617	4	3.1180	0.0698
3.4730	3	2.1889	0.0219	3	9.0456	0.2555	4	2.9973	0.0689
3.5079	3	2.1145	0.0198	3	8.7115	0.0703	4	2.7627	0.0242
3.5431	3	1.9214	0.0183	3	7.9537	0.0657	4	2.4920	0.0226
3.5787	3	1.7064	0.0166	3	7.0541	0.0601	4	2.1976	0.0208
3.6147	3	1.3327	0.0136	3	5.7815	0.0519	4	1.7871	0.0183
3.6510	2	8.9908	0.1016	3	4.1344	0.0408	4	1.2793	0.0150
3.6877	2	5.2527	0.0702	3	2.5774	0.0297	3	8.2623	0.1175
3.7248	2	2.9346	0.0492	3	1.4727	0.0210	3	4.7403	0.0876
3.7622	2	1.4972	0.0333	2	7.6190	0.1438	3	2.5095	0.0630
3.8000	1	6.8658	0.2175	2	3.7427	0.0977	3	1.2169	0.0445
3.8382	1	2.8392	0.1365	2	1.7160	0.0656	2	6.0564	0.3055
3.8768	1	1.0863	0.0869	1	7.0533	0.4123	2	2.3883	0.1971
3.9158	0	3.5585	0.4947	1	2.7745	0.2501	1	7.5021	1.0660
3.9551	-1	7.0938	2.2577	0	5.8612	1.1135			

Table A.1: Cross sections for $\theta_c = 15°$

Cross sections for $\theta_c = 23°$

E' [GeV]	p	^{12}C σ [10^p nb/sr/GeV]	$\Delta\sigma$	p	^{56}Fe σ [10^p nb/sr/GeV]	$\Delta\sigma$	p	^{197}Au σ [10^p nb/sr/GeV]	$\Delta\sigma$
2.5728	2	1.7753	0.0254	2	8.2492	0.1169	3	2.6797	0.0373
2.5987	2	1.7065	0.0247	2	7.6626	0.1109	3	2.5424	0.0360
2.6248	2	1.5878	0.0236	2	7.2577	0.1067	3	2.3963	0.0344
2.6512	2	1.4929	0.0228	2	6.6541	0.1000	3	2.1864	0.0326
2.6778	2	1.4030	0.0220	2	6.3192	0.0966	3	2.1130	0.0316
2.7048	2	1.3141	0.0210	2	6.0457	0.0935	3	1.9523	0.0303
2.7319	2	1.2616	0.0206	2	5.7590	0.0904	3	1.8801	0.0295
2.7594	2	1.2344	0.0203	2	5.3009	0.0859	3	1.7555	0.0282
2.7871	2	1.1015	0.0191	2	5.1222	0.0835	3	1.6158	0.0269
2.8151	2	1.0178	0.0183	2	4.5917	0.0779	3	1.5291	0.0260
2.8434	1	9.6201	0.1762	2	4.3582	0.0752	3	1.4696	0.0253
2.8720	1	9.2616	0.1727	2	4.3494	0.0748	3	1.3432	0.0241
2.9009	1	9.2273	0.1740	2	4.0402	0.0715	3	1.2969	0.0236
2.9300	1	8.3853	0.1643	2	3.6193	0.0672	3	1.1216	0.0218
2.9595	1	7.9908	0.1617	2	3.4337	0.0651	3	1.0476	0.0209
2.9892	1	7.3545	0.0825	2	3.0614	0.0278	2	9.7081	0.1339
3.0193	1	6.5532	0.0849	2	2.7108	0.0325	2	8.5360	0.1577
3.0496	1	5.8539	0.0779	2	2.3142	0.0295	2	7.4438	0.1434
3.0803	1	5.0234	0.0698	2	2.0208	0.0273	2	6.3174	0.1286
3.1112	1	4.1992	0.0616	2	1.7462	0.0251	2	5.3983	0.1167
3.1425	1	3.1655	0.0513	2	1.3732	0.0221	2	4.1273	0.0991
3.1741	1	2.4741	0.0435	2	1.0368	0.0190	2	3.3051	0.0862
3.2060	1	1.7174	0.0355	1	7.7533	0.1631	2	2.4014	0.0733
3.2382	1	1.2535	0.0290	1	5.2037	0.1344	2	1.6770	0.0601
3.2707	0	7.3660	0.2190	1	3.6807	0.1114	2	1.1769	0.0493
3.3036	0	5.1195	0.1793	1	2.3407	0.0889	1	8.4871	0.4122
3.3368	0	3.3073	0.1405	1	1.5813	0.0731	1	4.7138	0.3159
3.3703	0	2.0527	0.0317	0	9.9602	0.1687	1	3.3584	0.0960
3.4042	0	1.3362	0.0250	0	6.7016	0.1348	1	2.1772	0.0761
3.4384	-1	8.4167	0.1969	0	4.1382	0.1057	1	1.5242	0.0617
3.4730	-1	5.2167	0.1522	0	2.8177	0.0853	0	9.1119	0.4874
3.5079	-1	3.0208	0.0730	0	1.5558	0.0328	0	5.6298	0.4119
3.5431	-1	1.6069	0.0525	-1	9.3626	0.2511	0	3.5153	0.3138

3.5787	-2	7.8862	0.3808	-1	5.1797	0.1872	0	1.5787	0.2225
3.6147	-2	3.9147	0.2675	-1	2.4069	0.1297	0	1.0967	0.1723
3.6510	-2	1.5679	0.1635	-1	1.1066	0.0888	-1	4.5029	1.1141
3.6877	-3	4.5278	1.0158	-2	5.4091	0.6203			
3.7248	-3	2.0191	0.5894	-2	1.0620	0.3357			

Table A.2: Cross sections for $\theta_c = 23°$

Cross sections for $\theta_c = 30°$

E' [GeV]	p	^{12}C σ [10^p nb/sr/GeV]	$\Delta\sigma$	p	^{56}Fe σ [10^p nb/sr/GeV]	$\Delta\sigma$	p	^{197}Au σ [10^p nb/sr/GeV]	$\Delta\sigma$
1.9252	1	6.4466	0.0851	2	2.9162	0.0354	2	8.8002	0.1273
1.9445	1	5.9744	0.0808	2	2.8711	0.0349	2	8.5824	0.1248
1.9641	1	5.8233	0.0792	2	2.8019	0.0343	2	8.4333	0.1240
1.9838	1	5.5596	0.0765	2	2.5739	0.0325	2	7.7755	0.1177
2.0037	1	5.1572	0.0727	2	2.4593	0.0316	2	7.3720	0.1139
2.0239	1	4.9095	0.0705	2	2.2735	0.0301	2	7.0571	0.1105
2.0442	1	4.7799	0.0692	2	2.2180	0.0295	2	7.0145	0.1103
2.0648	1	4.6442	0.0675	2	2.0951	0.0234	2	6.4738	0.1054
2.0855	1	4.3067	0.0642	2	2.0424	0.0229	2	6.2169	0.1023
2.1065	1	3.9596	0.0611	2	1.8923	0.0219	2	5.7912	0.0982
2.1276	1	3.9544	0.0607	2	1.8584	0.0214	2	5.4877	0.0945
2.1490	1	3.7369	0.0584	2	1.7144	0.0205	2	5.1742	0.0913
2.1706	1	3.4886	0.0561	2	1.6358	0.0199	2	4.9498	0.0887
2.1924	1	3.2116	0.0532	2	1.5213	0.0190	2	4.6609	0.0857
2.2145	1	3.0244	0.0323	2	1.4271	0.0124	2	4.3183	0.0530
2.2367	1	2.8877	0.0314	2	1.3367	0.0119	2	4.1567	0.0515
2.2592	1	2.6908	0.0386	2	1.2114	0.0137	2	3.7398	0.0638
2.2819	1	2.4435	0.0366	2	1.1348	0.0131	2	3.4772	0.0609
2.3048	1	2.2760	0.0350	2	1.0329	0.0124	2	3.1271	0.0571
2.3280	1	2.0566	0.0330	1	9.4221	0.1176	2	2.8043	0.0542
2.3514	1	1.9572	0.0321	1	9.0023	0.1142	2	2.6543	0.0525
2.3750	1	1.8108	0.0307	1	8.0534	0.1072	2	2.5254	0.0504
2.3989	1	1.5669	0.0283	1	7.3814	0.1198	2	2.2790	0.0479
2.4230	1	1.5118	0.0276	1	6.7789	0.1137	2	2.0604	0.0455
2.4474	1	1.4132	0.0265	1	6.4190	0.1102	2	1.8919	0.0433
2.4720	1	1.2556	0.0250	1	5.5040	0.1012	2	1.7339	0.0415
2.4968	1	1.1848	0.0241	1	5.1704	0.0975	2	1.5713	0.0390
2.5219	1	1.0652	0.0227	1	4.6499	0.0924	2	1.3855	0.0364
2.5472	0	9.5368	0.2160	1	4.1874	0.0873	2	1.2680	0.0353
2.5728	0	8.3189	0.1077	1	3.8394	0.0263	2	1.1148	0.0205
2.5987	0	7.5181	0.1010	1	3.3002	0.0237	1	9.2742	0.1863
2.6248	0	6.5851	0.0938	1	2.9067	0.0217	1	8.2749	0.1753
2.6512	0	5.4321	0.0847	1	2.4576	0.0194	1	7.0421	0.1605

2.6778	0	4.5319	0.0764	1	2.0199	0.0172	1	5.7012	0.1452
2.7048	0	3.6069	0.0684	1	1.6485	0.0152	1	4.6584	0.1307
2.7319	0	2.8480	0.0600	1	1.3416	0.0135	1	3.8630	0.1203
2.7594	0	2.2657	0.0540	1	1.0558	0.0117	1	2.9870	0.1061
2.7871	0	1.6301	0.0450	0	7.9975	0.1001	1	2.3598	0.0934
2.8151	0	1.1493	0.0384	0	5.8487	0.0848	1	1.6627	0.0793
2.8434	-1	8.2928	0.1098	0	4.0607	0.0658	1	1.1613	0.0399
2.8720	-1	6.0653	0.0924	0	3.0308	0.0559	0	8.3480	0.3408
2.9009	-1	4.2132	0.0766	0	2.1642	0.0468	0	6.1543	0.2858
2.9300	-1	2.8390	0.0628	0	1.5062	0.0387	0	4.3953	0.2367
2.9595	-1	1.9837	0.0521	0	1.1196	0.0330	0	3.3933	0.2076
2.9892	-1	1.3611	0.0317	-1	7.7558	0.2025	0	2.1212	0.1723
3.0193	-2	9.7065	0.2946	-1	5.5529	0.2372	0	1.3204	0.1664
3.0496	-2	6.5740	0.2370	-1	3.6651	0.1953	0	1.1539	0.1463
3.0803	-2	4.0671	0.1920	-1	2.4304	0.1588	-1	7.0774	1.1736
3.1112	-2	2.8728	0.1598	-1	1.7862	0.1323	-1	4.5132	0.9833
3.1425	-2	1.8314	0.1332	-1	1.0743	0.1040	-1	3.5855	0.8902
3.1741	-2	1.0705	0.0995	-2	7.6662	0.8997	-1	1.9540	0.7522
3.2060	-3	6.2225	0.7557	-2	4.1995	0.6324			
3.2382	-3	4.4774	0.6405	-2	2.9628	0.5507			
3.2707	-3	2.9740	0.4940	-2	1.8332	0.4445			
3.3036	-3	1.0693	0.4138	-2	1.0158	0.3483			

Table A.3: Cross sections for $\theta_c = 30°$

Cross sections for $\theta_c = 37°$

E' [GeV]	p	^{12}C σ [10^p nb/sr/GeV]	$\Delta\sigma$	p	^{56}Fe σ [10^p nb/sr/GeV]	$\Delta\sigma$	p	^{197}Au σ [10^p nb/sr/GeV]	$\Delta\sigma$
1.6242	1	2.0773	0.0291	1	9.0011	0.1297	2	2.9633	0.0443
1.6405	1	1.9979	0.0282	1	8.3829	0.1241	2	2.7423	0.0420
1.6570	1	1.8681	0.0271	1	8.1100	0.1214	2	2.5247	0.0399
1.6737	1	1.7240	0.0257	1	7.7902	0.1190	2	2.3890	0.0383
1.6905	1	1.6348	0.0249	1	7.1488	0.1127	2	2.2890	0.0372
1.7075	1	1.5514	0.0240	1	6.6008	0.1080	2	2.1970	0.0362
1.7246	1	1.4739	0.0232	1	6.5031	0.1062	2	2.0403	0.0347
1.7420	1	1.4276	0.0227	1	6.1394	0.1031	2	1.9266	0.0335
1.7595	1	1.3139	0.0215	1	5.4768	0.0965	2	1.7821	0.0320
1.7772	1	1.2666	0.0211	1	5.3301	0.0955	2	1.7222	0.0313
1.7950	1	1.1682	0.0200	1	5.2519	0.0940	2	1.5970	0.0300
1.8131	1	1.0780	0.0193	1	4.8480	0.0904	2	1.5569	0.0295
1.8313	1	1.0374	0.0187	1	4.4042	0.0855	2	1.4768	0.0288
1.8497	0	9.5358	0.1785	1	4.2325	0.0842	2	1.3323	0.0272
1.8683	0	9.2080	0.1745	1	4.0007	0.0821	2	1.2384	0.0259
1.8870	0	8.3152	0.1113	1	3.4929	0.0467	2	1.0963	0.0171
1.9060	0	7.5537	0.1049	1	3.1543	0.0441	1	9.8064	0.1608
1.9252	0	6.7214	0.0986	1	2.8931	0.0415	1	8.9047	0.1523
1.9445	0	6.1094	0.0923	1	2.6470	0.0395	1	8.4303	0.1469
1.9641	0	5.7504	0.0892	1	2.4327	0.0376	1	7.6663	0.1394
1.9838	0	5.0662	0.0831	1	2.0846	0.0347	1	6.6334	0.1292
2.0037	0	4.8519	0.0802	1	2.0257	0.0341	1	6.1768	0.1237
2.0239	0	4.2914	0.0752	1	1.8542	0.0324	1	5.5918	0.1165
2.0442	0	3.7969	0.0705	1	1.6170	0.0303	1	5.0682	0.1106
2.0648	0	3.4072	0.0667	1	1.4777	0.0288	1	4.4949	0.1045
2.0855	0	3.1757	0.0634	1	1.3580	0.0275	1	4.0801	0.0991
2.1065	0	2.8960	0.0603	1	1.2852	0.0268	1	3.7613	0.0954
2.1276	0	2.5962	0.0567	1	1.1012	0.0248	1	3.3999	0.0901
2.1490	0	2.4212	0.0541	0	9.6648	0.2329	1	3.1011	0.0854
2.1706	0	2.0667	0.0505	0	8.5823	0.2185	1	2.7350	0.0803
2.1924	0	1.9136	0.0483	0	7.4535	0.2058	1	2.4041	0.0757
2.2145	0	1.5770	0.0134	0	6.4480	0.1121	1	1.9882	0.0293
2.2367	0	1.3366	0.0121	0	5.5011	0.1013	1	1.7242	0.0270

continued from the previous page

2.2592	0	1.1484	0.0111	0	4.7024	0.0911	1	1.4304	0.0247
2.2819	-1	9.5222	0.0992	0	3.9417	0.0813	1	1.1684	0.0223
2.3048	-1	7.6688	0.0881	0	3.1433	0.0711	1	1.0116	0.0206
2.3280	-1	6.3024	0.0788	0	2.6560	0.0640	0	8.4158	0.1875
2.3514	-1	5.0136	0.0692	0	2.2132	0.0572	0	6.5767	0.1660
2.3750	-1	3.8514	0.0601	0	1.7675	0.0499	0	5.4932	0.1512
2.3989	-1	3.0388	0.0528	0	1.2468	0.0416	0	4.2927	0.1335
2.4230	-1	2.1970	0.0446	0	1.1248	0.0385	0	2.9605	0.1122
2.4474	-1	1.7468	0.0393	-1	7.5374	0.3163	0	2.5014	0.1033
2.4720	-1	1.3345	0.0339	-1	6.0831	0.2811	0	1.8394	0.0881
2.4968	-2	9.0534	0.2791	-1	4.4772	0.2420	0	1.3648	0.0779
2.5219	-2	7.3105	0.2510	-1	3.0412	0.1933	0	1.0997	0.0681
2.5472	-2	5.2266	0.2096	-1	2.4746	0.1789	-1	8.7097	0.6222
2.5728				-1	1.8806	0.1467			
2.5987				-1	1.4240	0.1275			
2.6248				-2	7.5653	1.0279			
2.6512				-2	7.4883	0.9307			
2.6778				-2	4.2554	0.7815			
2.7048				-2	2.3618	0.5229			
2.7319				-2	2.1047	0.5517			
2.7594				-2	1.1463	0.3977			

Table A.4: Cross sections for $\theta_c = 37°$

Cross sections for $\theta_c = 45°$

E' [GeV]	p	^{12}C σ [10^p nb/sr/GeV]	$\Delta\sigma$	p	^{56}Fe σ [10^p nb/sr/GeV]	$\Delta\sigma$	p	^{197}Au σ [10^p nb/sr/GeV]	$\Delta\sigma$
1.6242	0	1.9497	0.0450	0	8.1291	0.2608	1	2.2359	0.0545
1.6405	0	1.6896	0.0413	0	7.4737	0.2461	1	2.1433	0.0530
1.6570	0	1.6097	0.0399	0	6.6385	0.2324	1	1.9504	0.0505
1.6737	0	1.4079	0.0367	0	6.1726	0.2214	1	1.8257	0.0484
1.6905	0	1.2580	0.0348	0	5.2406	0.2037	1	1.5447	0.0450
1.7075	0	1.1096	0.0328	0	4.6774	0.1928	1	1.3147	0.0411
1.7246	0	1.0052	0.0311	0	4.1623	0.1796	1	1.2287	0.0392
1.7420	-1	9.3692	0.2944	0	3.2810	0.1626	1	1.1200	0.0373
1.7595	-1	7.9599	0.2746	0	3.4998	0.1615	0	9.7574	0.3509
1.7772	-1	6.6838	0.2512	0	2.9645	0.1535	0	8.6386	0.3269
1.7950	-1	6.5829	0.2416	0	2.4543	0.1381	0	8.1648	0.3182
1.8131	-1	5.5737	0.2258	0	2.3933	0.1371	0	6.8591	0.2912
1.8313	-1	5.2051	0.2163	0	1.8261	0.1161	0	6.1586	0.2755
1.8497	-1	4.2963	0.1945	0	1.7563	0.1143	0	5.0499	0.2472
1.8683	-1	3.7558	0.1836	0	1.6594	0.1101	0	4.6739	0.2377
1.8870	-1	2.9818	0.0849	0	1.2544	0.0275	0	3.7002	0.1498
1.9060	-1	2.5110	0.0755	0	1.0311	0.0251	0	2.8882	0.1330
1.9252	-1	1.9288	0.0666	-1	8.8982	0.2298	0	2.7263	0.1259
1.9445	-1	1.5915	0.0604	-1	6.9661	0.2037	0	1.9691	0.1103
1.9641	-1	1.2724	0.0549	-1	6.1646	0.1901	0	1.5379	0.0988
1.9838	-1	1.0613	0.0494	-1	4.6687	0.1663	0	1.3957	0.0922
2.0037	-2	8.7174	0.4355	-1	3.4084	0.1440	0	1.1590	0.0812
2.0239	-2	6.2646	0.3798	-1	2.7804	0.1266	-1	8.4989	0.7061
2.0442	-2	4.9565	0.3323	-1	2.2246	0.1141	-1	5.3447	0.6171
2.0648	-2	3.3577	0.2831	-1	1.6655	0.1006	-1	4.3756	0.5501
2.0855	-2	3.2618	0.2654	-1	1.2369	0.0851	-1	3.6315	0.4509
2.1065	-2	2.3370	0.2372	-1	1.1496	0.0787	-1	3.0372	0.4164
2.1276	-2	2.0411	0.2021	-2	8.0389	0.6428	-1	3.0372	0.3884
2.1490	-2	1.1046	0.1140	-2	5.5201	0.3772	-1	2.2064	0.3685
2.1706	-2	1.0820	0.1097	-2	4.1951	0.3173	-1	2.2870	0.3663
2.1924	-3	7.6393	0.9555	-2	3.9363	0.3020	-2	7.2023	2.8399
2.2145	-3	6.7036	1.9434	-2	2.4659	0.3250			
2.2367	-3	5.0196	1.8311	-2	1.9091	0.2818			

2.2592		-2	1.4339	0.2425	
2.2819		-3	9.0789	2.0872	
2.3048		-3	8.6817	1.7807	
2.3280		-3	7.1332	1.5233	
2.3514		-3	4.3556	1.3617	

Table A.5: Cross sections for $\theta_c = 45°$

Cross sections for $\theta_c = 55°$

E' [GeV]	p	^{12}C σ [10^p nb/sr/GeV]	$\Delta\sigma$	p	^{56}Fe σ [10^p nb/sr/GeV]	$\Delta\sigma$	p	^{197}Au σ [10^p nb/sr/GeV]	$\Delta\sigma$
1.0356	0	4.1224	0.1210	1	1.8265	0.0410	1	5.3644	0.2025
1.0460	0	3.7287	0.1152	1	1.6835	0.0394	1	5.0966	0.1962
1.0566	0	3.6427	0.1134	1	1.5070	0.0368	1	4.6079	0.1879
1.0672	0	3.3664	0.1078	1	1.4978	0.0367	1	4.1314	0.1772
1.0779	0	3.0823	0.1032	1	1.3025	0.0337	1	4.1255	0.1732
1.0887	0	2.8332	0.0989	1	1.1754	0.0318	1	3.7526	0.1661
1.0997	0	2.6661	0.0949	1	1.1487	0.0313	1	3.5883	0.1613
1.1107	0	2.3487	0.0890	1	1.1152	0.0310	1	3.2192	0.1510
1.1219	0	2.3451	0.0897	0	9.6546	0.2837	1	3.2860	0.1499
1.1332	0	2.2040	0.0847	0	9.4365	0.2816	1	2.9926	0.1461
1.1446	0	2.1246	0.0834	0	8.9434	0.2724	1	2.8613	0.1435
1.1561	0	2.0314	0.0811	0	7.8599	0.2559	1	2.7634	0.1390
1.1677	0	1.8622	0.0765	0	7.7056	0.2540	1	2.5745	0.1352
1.1794	0	1.8425	0.0765	0	7.4061	0.2461	1	2.5244	0.1333
1.1913	0	1.4695	0.0695	0	7.0949	0.2411	1	2.0792	0.1187
1.2032	0	1.5122	0.0375	0	5.9025	0.1437	1	1.7955	0.0592
1.2153	0	1.3399	0.0412	0	5.3189	0.1707	1	1.6439	0.0633
1.2275	0	1.1817	0.0386	0	4.9902	0.1629	1	1.4209	0.0587
1.2399	0	1.1256	0.0375	0	4.4405	0.1501	1	1.3307	0.0553
1.2523	0	1.0292	0.0353	0	4.1011	0.1434	1	1.2708	0.0531
1.2649	-1	9.5805	0.3404	0	3.9429	0.1393	1	1.1006	0.0508
1.2776	-1	8.6407	0.3248	0	3.5839	0.1323	1	1.0878	0.0502
1.2905	-1	7.5314	0.3008	0	3.1085	0.1212	0	9.2932	0.4497
1.3034	-1	6.7770	0.2876	0	2.6403	0.1109	0	8.4034	0.4318
1.3165	-1	6.0456	0.2679	0	2.1888	0.1001	0	7.5163	0.4036
1.3298	-1	5.9379	0.2572	0	2.1554	0.0970	0	6.9937	0.3882
1.3431	-1	5.3139	0.2466	0	2.0290	0.0946	0	6.4531	0.3736
1.3566	-1	4.6708	0.2320	0	1.8720	0.0906	0	5.9978	0.3586
1.3703	-1	4.3663	0.2218	0	1.6543	0.0831	0	5.3399	0.3420
1.3840	-1	3.6212	0.1999	0	1.4515	0.0797	0	4.9675	0.3147
1.3980	-1	3.1248	0.0501	0	1.2435	0.0296	0	4.1315	0.1568
1.4120	-1	2.7188	0.0496	0	1.0869	0.0340	0	3.8179	0.2113
1.4262	-1	2.3911	0.0465	-1	9.1117	0.3090	0	3.0664	0.1924

1.4405	-1	2.1167	0.0433	-1	8.2891	0.2909	0	2.6102	0.1793
1.4550	-1	1.7838	0.0394	-1	7.4193	0.2737	0	2.4362	0.1672
1.4696	-1	1.5274	0.0363	-1	6.7918	0.2589	0	1.8765	0.1483
1.4844	-1	1.3669	0.0344	-1	5.6802	0.2400	0	1.8062	0.1430
1.4993	-1	1.2150	0.0323	-1	5.0997	0.2230	0	1.3024	0.1241
1.5144	-2	9.6281	0.2844	-1	4.3249	0.2060	0	1.2357	0.1246
1.5296	-2	8.5532	0.2663	-1	3.5893	0.1868	0	1.1720	0.1203
1.5450	-2	7.3330	0.2456	-1	3.2638	0.1756	-1	9.2841	1.0018
1.5605	-2	6.1502	0.2237	-1	2.4908	0.1558	-1	8.9697	0.9887
1.5762	-2	5.0107	0.1988	-1	2.2265	0.1483	-1	6.9352	0.9422
1.5920	-2	4.0701	0.1785	-1	1.9310	0.1369	-1	6.8825	0.8583
1.6080	-2	3.4041	0.1610	-1	1.4117	0.1138	-1	4.3278	0.7268
1.6242				-1	1.1168	0.0882			
1.6405				-2	8.8913	0.7842			
1.6570				-2	6.7953	0.6805			
1.6737				-2	6.8375	0.6700			
1.6905				-2	4.8841	0.5632			
1.7075				-2	4.8220	0.5460			
1.7246				-2	2.4221	0.3923			
1.7420				-2	2.9237	0.4280			
1.7595				-2	1.2833	0.3138			
1.7772				-2	1.7052	0.3189			
1.7950				-3	9.3905	2.2295			
1.8131				-2	1.1424	0.2433			
1.8313				-3	4.4445	1.5416			
1.8497				-3	5.2684	1.7466			

Table A.6: Cross sections for $\theta_c = 55°$

Appendix B

Laboratory History

The colorful history leading to the birth of TJNAF stretches back to the 1950's when Robert Hofstadter of Stanford University pioneered the use of electron scattering to study nuclear structure. During the 1960's, the Stanford Linear Accelerator Center (SLAC) inheirited and expanded upon these early efforts. After more than a decade of success, which included the discovery of quarks and the emergence of QCD, the research program at SLAC and at other laboratories, spurred on by the rise of the Standard Model, pushed toward ever higher energies. The perspective gained by the late 1970's revealed that a large domain of unresolved and overlooked questions about the relationship of the quark and gluon degrees of freedom to the more traditional baryon and meson descriptions of hadronic matter invited a return to lower energies. Thus the scientific foundation for what would become TJNAF had formed.

The official call for a continuous wave (CW) 2 GeV electron accelerator arrived in

1980 from the Nuclear Science Advisory Committee (NSAC), a panel commissioned by the Department of Energy (DOE) and the National Science Foundation (NSF) [102]. In parallel with the national trends that led to the NSAC recommendation, University of Virginia physicists Jim McCarthy, Blaine Norum, and Richard York conceived a design for just such a machine a year earlier [103]. They envisaged a conventional linear accelerator feeding a pulse stretcher ring (PSR). The high current short linac pulse stored in the PSR would be slowly extracted at much lower current for delivery to the experimental halls. Consequently, each linac pulse would stretch in time to completely fill the interval between pulses, thereby producing a continuous beam.

In May of 1980, Jim McCarthy organized the Southeastern Universities Research Association (SURA) to build support for the fledgling accelerator project. Shortly thereafter the project had a name, and SURA submitted to DOE and NSF a proposal for the construction of the National Electron Accelerator Laboratory (NEAL).

The next several years proved tumultuous [104, 105]. First, a debate erupted over the appropriate energy for such a facility. This led to the addition of a single pass recirculator to double the energy to 4 GeV. The redesigned NEAL then found competition in December of 1982 from four new proposals, including the Hexatron from Argonne National Laboratory. Finally, in 1983, the NSAC selected the SURA proposal; the political fight with Argonne, however, would last the remainder of the year.

NEAL became the Continuous Electron Beam Accelerator Facility (CEBAF) in

July of 1983. CEBAF soon ran into more troubled waters when the December 1983 NSAC report emphasized need for a relativistic heavy ion collider. Such a facility would, in time, materialize as RHIC, but Congress did not appreciate the mixed signals. This controversy [106, 107] finally resolved in late 1984, but the residue impeded the flow of funds and delayed the start of construction.

In December of 1985 DOE accepted a proposal that radically changed the CE-BAF design. Instead of a linac/PSR, the new design used superconducting radio frequency (SRF) cavities for CW electron acceleration. Conventional copper cavities would consume many megawatts of power, if they did not melt first, when operated in CW mode. This confines conventional linacs to pulsed mode operation, as in the original CEBAF design. SRF technology removes much of the power loss, and therefore permits CW operation. Even adding the power consumed delivering cryogens to the cavities, the balance comes out in favor of SRF. The new design also posessed greater flexibility, providing a straightforward upgrade path to higher energies, and the multipass recirculation made available multiple beam energies for use in the experimental halls. Furthermore, the SRF design promised a higher quality beam with smaller energy spread and smaller emittance.

The project enjoyed steady progress over the course of the next decade. Construction began at the Newport News, Virginia site in 1987. July 1988 brought a minor design change, from four to five recirculation passes. The injector came online in 1991; fabrication and processing of the rest of the SRF cavities and cryomodules

continued through 1993. In June of 1994, the Central Helium Liquifier (CHL) was fully operational, providing cryogens to the injector and both linacs. One month later, CEBAF delivered one pass 845 MeV beam to Hall C. Only ten more months were needed to acheive the five pass 4.045 GeV CW goal.

CEBAF became the Thomas Jefferson National Accelerator Facility (TJNAF) in May of 1996 at a site dedication ceremony. At a total cost of more than $600 million, the facility was largely complete and the experimental program was well underway.

Appendix C

Solid target beam heating

The following contains excerpts from two technical papers [108, 109] written by this author to examine the problem of beam heating in the solid targets. The simplest calculation assumes that both the target and raster have circular geometry. In a more sophisticated calculation, the Green's function method is applied to understand both the effect of the rectangular target geometry and the effect of the lissajous raster pattern generated by the sinusoidally driven horizontal and vertical raster magnets. The Green's function method, in fact, may be applied to any raster distribution.

The results confirm the expectation that the thermally anchored side nearest to the raster has the most control over the heat flow out of the target. Clearly, the target is coolest if all four sides are held at a fixed temperature, however there is little detrimental effect when the two sides farthest from the raster are insulated. In contrast, when the two closest sides are insulated, the target temperature increase can

be significant. A similar result is that the target remains cooler for the statistically wider lissajous raster pattern than for a uniform raster distribution.

Comparison of the rectangular and circular target results show that, provided the length and width do not differ greatly, the rectangular target problem can be replaced by an effective circular target problem having the same target and raster areas. This approximation is useful not only because it is computational simple, but also because the effect of temperature dependence of the thermal conductivity of the target can be evaluated exactly.

C.1   Definitions and assumptions

Throughout this discussion, κ denotes thermal conductivity, and ρ denotes density. For circular geometry, the target radius is R_0 and the raster radius is R. For rectangular geometry, the widths of the target and raster are $2a$ and $2A$, respectively, and the heights are $2b$ and $2B$.

A few assumptions are necessary to perform the calculations. Cooling by radiative heat loss is neglected; explicit calculation indicates that this is indeed a good assumption. Since the target chamber vacuum prevents convective heat loss, all of the heat generated in the target flows out the thermally anchored sides and into the target ladder. These sides of the target are therefore maintained at the (fixed) temperature of the target ladder. All calculations assume the entire system has achieved thermal

equilibrium.

The goal is to determine the temperature distribution over the surface of the target. The starting point is the relationship $\dot{\mathbf{Q}} = -\kappa \nabla T$ between the heat flow $\dot{\mathbf{Q}}$ and the temperature gradient. The heat source in this problem is the power delivered by the flow of electrons I/e depositing the minimum ionization energy $\rho \tau \cdot dE/dx$. Since the beam power is distributed uniformly throughout the target thickness τ, beam heating is a two-dimensional problem. The distribution of the beam power across the surface of the target is given by the raster distribution $\wp$ which is normalized such that the surface integral $\int \wp(x,y)\, dx\, dy \equiv 1$. Because the heat source determines the divergence of the heat flow:

$$\nabla \cdot \dot{\mathbf{Q}} = -\nabla \cdot (\kappa \nabla T) = \rho \frac{dE}{dx} \frac{I}{e}\, \wp \tag{C.1}$$

The appropriate boundary conditions describing the thermal conditions on the sides of the target accompany this differential equation to complete the definition of the beam heating problem.

C.2   Circular geometry

For a circular target and uniform raster pattern, the solution to the differential equation is particularly simple. Using polar coordinates and symmetry, the problem is

reduced to a one-dimensional differential equation:

$$\frac{1}{r}\frac{d}{dr}\left(r\kappa\frac{dT}{dr}\right) = -\rho\frac{dE}{dx}\frac{I}{e}\frac{\Theta(R-r)}{\pi R^2} \tag{C.2}$$

where the normalized step function has been inserted for the raster pattern $\wp$. Integrating twice yields:

$$\int_{T(r)}^{T(0)} \kappa\, dT = \rho\frac{dE}{dx}\frac{I}{e}\cdot\frac{1}{4\pi}\begin{cases} (r/R)^2 & r < R \\ \\ 1 + 2\ln(r/R) & r \geq R \end{cases} \tag{C.3}$$

This expression gives the temperature distribution across the surface of the target. Evaluating at the target radius $r = R_0$ where the target ladder maintains the fixed temperature $T(R_0) \equiv T_E$, the center target temperature $T(0)$ is the solution to:

$$\int_{T_E}^{T(0)} \kappa\, dT = \rho\frac{dE}{dx}\frac{I}{e}\cdot\frac{1}{4\pi}\left[1 + 2\ln(R_0/R)\right] \tag{C.4}$$

This expression is left in integral form to account for the possible temperature dependence of the thermal conductivity. Figure 3.5 indicates the importance of this effect for iron targets. The left panel shows the temperature dependence of κ; integrating the quadratic parameterization according to equation (C.4) produces a cubic equation for the center target temperature. The right panel shows the resulting nonlinear dependence of the center target temperature with increasing beam current.

C.3   Rectangular geometry

To examine the effects of the rectangular target geometry, the various choices of thermally anchoring the sides of the target, and the lissajous raster pattern, the Green's function method is used to compute exact solutions to the beam heating problem for rectangular targets. For this problem, the thermal conductivity is assumed to be temperature independent.

The Green's function method requires first solving a related problem possesing the same boundary conditions but with a point source of heat:

$$\nabla^2 G(\vec{x}, \vec{x}') = -\delta(\vec{x} - \vec{x}') \tag{C.5}$$

The original problem with the heat source distributed according to the raster distribution $\wp(\vec{x})$ is then solved by the convolution integral:

$$T(\vec{x}) = \rho \frac{dE}{dx} \frac{I}{e\kappa} \int G(\vec{x}, \vec{x}') \wp(\vec{x}') \, d^2x' \tag{C.6}$$

The point source solution $G(\vec{x}, \vec{x}')$ is known as the Green's function for this problem. The Green's function method has the advantage that it can be applied for *any* raster pattern.

To solve for the Green's function, one more abstraction is necessary. Consider the

complete set of functions defined by solutions to the eigenvalue problem:

$$\nabla^2 f_i = -\lambda^2 f_i \tag{C.7}$$

where the i represents a set of indices uniquely labelling the solutions. Using orthonormality and the definition (C.5) of the Green's function, it is straightforward to show that the Green's function may be expanded as:

$$G(\vec{x}, \vec{x}') = \sum_i \frac{f_i^\dagger(\vec{x}')f_i(\vec{x})}{\lambda^2} \tag{C.8}$$

According to this recipe, once the eigenvalue problem for rectangular geometry is solved an expression for the appropriate Green's function can be constructed. The convolution integral (C.6) of the Green's function with the extended source then solves the original differential equation for the temperature distribution.

The standard approach to the eigenvalue problem proceeds by separation of variables. In rectangular coordinates, the functions f take the form $f(x,y) = X(x)Y(y)$. The eigenvalue equation (C.7) therefore reduces to:

$$\frac{X''}{X} + \lambda^2 = -\frac{Y''}{Y} \equiv \kappa^2$$

where κ is a constant not to be confused with the thermal conductivity. Accordingly,

there are now two separate equations:

$$
\begin{aligned}
X'' + k^2 X &= 0 \\
Y'' + \kappa^2 Y &= 0
\end{aligned}
\tag{C.9}
$$

where $k^2 = \lambda^2 - \kappa^2$. Each of these equations has trivial harmonic solutions which are determined explicitly by the boundary conditions of the problem.

There are, in general, two types of boundary conditions: the Dirichlet condition (D) is present along any edge of the target held at a fixed temperature; and the von Neumann condition (N) occurs when the heat flow or, equivalently, the normal derivative of the temperature is specified along an edge. Both conditions may be present, depending upon target design. Most target designs keep either two or, ideally, all four edges at a fixed temperature $T_E \equiv 0$, and therefore have at most two edges insulated so that either $\partial T/\partial x = 0$ or $\partial T/\partial y = 0$. As a matter of notation, it is convenient to introduce the labels DD, ND, and DN to specify the set of boundary conditions under consideration. The first letter indicates the conditions on the vertical edges of the target, and the second letter indicates the conditions on the horizontal edges. Although some other combinations of target boundary conditions are possible, such as three D sides and one N side, the mathematical procedure is only marginally different from that presented here.

The symmetry of having the same boundary conditions on parallel sides of a

target simplifies the solutions to (C.9) in two ways. First, the wave vectors satisfy $k_m a = m\pi/2$ and $\kappa_n b = n\pi/2$, where m and n index the solutions. Second, harmonic solutions for parallel Dirichlet conditions are sines (cosines) when the solution index is even (odd); similarly, for parallel von Neumann conditions, the solutions are sines (cosines) when the index is odd (even). As an explicit example, consider ND conditions. Then the full form of the normalized eigenfunctions $X_m(x)$ and $Y_n(y)$ are:

$$X_m(x) = \frac{1}{\sqrt{a}} \begin{cases} \sin\frac{m\pi}{2a}x & m \text{ odd} \\[2mm] \cos\frac{m\pi}{2a}x & m \neq 0, \text{ even} \\[2mm] \frac{1}{\sqrt{2}} & m = 0 \end{cases} \tag{C.10}$$

$$Y_n(y) = \frac{1}{\sqrt{b}} \begin{cases} \cos\frac{n\pi}{2b}y & n \text{ odd} \\[2mm] \sin\frac{n\pi}{2b}y & n \text{ even} \end{cases} \tag{C.11}$$

Notice the exception for $m = 0$ which appears for von Neumann conditions. Using the symbol cs to indicate either a cosine or sine, general expressions for the normalized solutions X and Y for DD, ND, or DN boundary conditions become:

$$X_m(x) = \frac{\text{cs}(k_m x)}{\sqrt{a}} \quad \text{and} \quad Y_n(y) = \frac{\text{cs}(\kappa_n y)}{\sqrt{b}} \tag{C.12}$$

and, therefore, the Green's function takes the form:

$$G(\vec{x}, \vec{x}') = \sum_{m,n}^{\infty} \frac{\mathrm{cs}(k_m x')\mathrm{cs}(\kappa_n y')}{ab[k_m^2 + \kappa_n^2]}\mathrm{cs}(k_m x)\mathrm{cs}(\kappa_n y) \qquad (\mathrm{C}.13)$$

The convolution integral (C.6) can now be performed for particular choices of the raster pattern.

First, consider a completely uniform, rectangular raster pattern. Such a pattern is represented as:

$$\wp(x, y) = \begin{cases} 1/4AB & \text{for } |x| \le A, |y| \le B \\[2mm] 0 & \text{otherwise} \end{cases}$$

This is an even parity function, i.e. $\wp(-\vec{x}) = \wp(\vec{x})$, so all of the odd parity eigenfunctions contributing to the Green's function will drop out upon integration. For the three cases DD, ND, and DN, this means the eigenfunctions with sines will integrate to zero. The generalized temperature distribution becomes:

$$T(x, y) = \rho \frac{dE}{dx} \frac{I}{e\kappa} \sum_{m,n}^{\infty} \frac{\sin k_m A \sin \kappa_n B}{ABabk_m \kappa_n [k_m^2 + \kappa_n^2]} \cos k_m x \cos \kappa_n y \qquad (\mathrm{C}.14)$$

and, evaluating at $x = 0$ and $y = 0$, the expression:

$$T(0,0) = \rho \frac{dE}{dx} \frac{I}{e\kappa} \sum_{m,n}^{\infty} \frac{\sin k_m A \sin \kappa_n B}{ABabk_m \kappa_n [k_m^2 + \kappa_n^2]} \qquad (\mathrm{C}.15)$$

gives the temperature at the center of the target, which is also the maximum target temperature. From the parity of the raster distribution, as discussed above, the m and n in the summations are both odd for DD conditions, even and odd for ND, and odd and even for DN in order to select the even parity eigenfunctions.

The exception for von Neumann conditions when the index is zero (C.11) must be kept in mind. For clarity, therefore, the result for ND conditions is listed explicitly:

$$T_{ND}(0,0) = \rho \frac{dE}{dx} \frac{I}{e\kappa} \left[\sum_{n=0}^{\infty} \frac{\sin \kappa_n B}{2Bab\kappa_n^3} + \sum_{m=1,n=0}^{\infty} \frac{\sin k_m A \sin \kappa_n B}{ABabk_m\kappa_n[k_m^2 + \kappa_n^2]} \right] \qquad (C.16)$$

where $k_m = 2m\pi/2a$ and $\kappa_n = (2n+1)\pi/2b$ in the summations to choose the even parity eigenfunctions for ND conditions.

The Green's function solution is most useful for raster patterns that are more complicated than the previous example. Since the raster magnets in Hall C are driven sinusoidally, the beam spends a large amount of time on the perimeter of the rastered area. This raster distribution has the following form:

$$\wp(x,y) = \begin{cases} \left(\frac{1}{\pi}\right)^2 (A^2 - x^2)^{-1/2}(B^2 - y^2)^{-1/2} & \text{for } |x| \leq A, |y| \leq B \\ 0 & \text{otherwise} \end{cases} \qquad (C.17)$$

To perform the convolution integral, the following identity is useful:

$$\int_{-\tau}^{\tau} \frac{\cos \omega t}{\sqrt{\tau^2 - t^2}} \, dt = \pi J_0(\omega \tau)$$

where J_0 is the zeroth order Bessel function. The temperature distribution therefore takes the general form:

$$T(x,y) = \rho \frac{dE}{dx} \frac{I}{e\kappa} \sum_{m,n}^{\infty} \frac{J_0(k_m A) J_0(\kappa_n B)}{ab[k_m^2 + \kappa_n^2]} \cos k_m x \cos \kappa_n y \qquad \text{(C.18)}$$

where, as before, m and n are odd or even according to the boundary conditions, and the special case for von Neumann conditions at zero index must be handled properly.

Bibliography

[1] J. J. Kelly, in *Advances in Nuclear Physics*, edited by J. W. Negele and E. W. Vogt (Plenum Press, New York, 1996), Vol. 23.

[2] S. Frullani and J. Mougey, in *Advances in Nuclear Physics*, edited by J. W. Negele and E. W. Vogt (Plenum Press, New York, 1984), Vol. 14.

[3] R. W. Lourie, in *Intersections between Particle and Nuclear Physics*, edited by G. M. Bunce (AIP, New York, 1988), p. 103.

[4] D. B. Day *et al.*, Annu. Rev. Nucl. Part. Sci. **40**, 357 (1990).

[5] R. G. Roberts, *The Structure of the Proton* (Cambridge University Press, Cambridge, 1990).

[6] R. L. Jaffe, in *Relativistic Dynamics and Quark-Nuclear Physics*, edited by M. B. Johnson (1986), p. 537.

[7] A. Buras, Rev. Mod. Phys. **52**, 199 (1980).

[8] R. R. Whitney *et al.*, Phys. Rev. C **9**, 2230 (1974).

[9] E. J. Moniz, Phys. Rev. **184**, 1154 (1969).

[10] R. Rosenfelder, Ann. Phys. **128**, 188 (1980).

[11] D. Day *et al.*, Phys. Rev. Lett. **43**, 1143 (1979).

[12] I. Sick, D. Day, and J. S. McCarthy, Phys. Rev. Lett. **45**, 871 (1980).

[13] W. P. Schutz *et al.*, Phys. Rev. Lett. **38**, 259 (1977).

[14] R. G. Arnold *et al.*, Phys. Rev. Lett. **61**, 806 (1988).

[15] R. M. Sealock *et al.*, Phys. Rev. Lett. **62**, 1350 (1989).

[16] D. Day *et al.*, Phys. Rev. Lett. **59**, 427 (1987).

[17] C. Marchand *et al.*, Phys. Rev. Lett. **60**, 1703 (1988).

[18] R. Altemus *et al.*, Phys. Rev. Lett. **44**, 965 (1980).

[19] P. Barreau *et al.*, Nucl. Phys. **A402**, 515 (1983).

[20] Z. E. Meziani *et al.*, Phys. Rev. Lett. **52**, 2130 (1984).

[21] Z. E. Meziani *et al.*, Phys. Rev. Lett. **54**, 1233 (1985).

[22] M. Deady *et al.*, Phys. Rev. C **33**, 1897 (1986).

[23] L. Weinstein *et al.*, Phys. Rev. Lett. **64**, 1646 (1990).

[24] P. E. Ulmer *et al.*, Phys. Rev. Lett. **59**, 2259 (1987).

[25] S. Stein *et al.*, Phys. Rev. D **12**, 1884 (1975).

[26] J. D. Bjorken, Phys. Rev. **179**, 1547 (1969).

[27] R. P. Feynman, Phys. Rev. Lett. **23**, 1415 (1969).

[28] L. W. Whitlow *et al.*, Phys. Lett. B **282**, 475 (1992).

[29] A. C. Benvenuti *et al.*, Phys. Lett. B **223**, 485 (1989).

[30] M. Arneodo *et al.*, Phys. Lett. B **364**, 107 (1995).

[31] S. Aid *et al.*, Nucl. Phys. **B470**, 3 (1996).

[32] H. L. Lai *et al.*, Phys. Rev. D **55**, 1280 (1997).

[33] J. J. Aubert *et al.*, Phys. Lett. **123B**, 275 (1982).

[34] F. E. Close, R. G. Roberts, and G. G. Ross, Phys. Lett. **129B**, 346 (1983).

[35] J. Gomez *et al.*, Phys. Rev. D **49**, 4348 (1994).

[36] E89008 Collaboration, Phys. Rev. Lett. **82**, 2056 (1999).

[37] P. Ring and P. Schuck, *The Nuclear Many-Body Problem* (Springer-Verlag, New York, 1980).

[38] J. D. Walecka, *Theoretical Nuclear and Subnuclear Physics* (Oxford University Press, New York, 1995).

[39] A. Fetter and J. Walecka, *Quantum Theory of Many-Particle Systems* (McGraw-Hill, New York, 1971).

[40] C. C. degli Atti and S. Simula, Phys. Rev. C **53**, 1689 (1996).

[41] R. L. Jaffe, in *Pointlike Structures Inside and Outside Hadrons, 1979 Erice School*, edited by A. Zichichi (Plenum Press, New York, 1982), p. 99.

[42] J. Carlson *et al.*, Phys. Rev. D **27**, 233 (1983).

[43] S. Galster *et al.*, Nucl. Phys. **B32**, 221 (1971).

[44] J. J. Sakurai, Ann. Phys. **11**, 1 (1960).

[45] S. J. Brodsky and G. Farrar, Phys. Rev. Lett. **31**, 1153 (1973).

[46] M. Gari and W. Krümpelmann, Z. Phys. **A322**, 689 (1985).

[47] J. V. Noble, Phys. Rev. Lett. **46**, 412 (1981).

[48] T. de Forest, Nucl. Phys. **A392**, 232 (1983).

[49] A. Bodek, Phys. Rev. D **20**, 1471 (1979).

[50] T. Cheng and L. Li, *Gauge Theory of Elementary Particles* (Oxford University Press, 1992).

[51] O. Nachtmann, Nucl. Phys. **B63**, 237 (1973).

[52] F. E. Close, J. Qiu, and R. G. Roberts, Phys. Rev. D **40**, 2820 (1989).

[53] J. Qiu, Nucl. Phys. **B291**, 746 (1987).

[54] G. B. West, Phys. Rep. **18**, 263 (1975).

[55] E. Pace and G. Salme, Phys. Lett. B **110**, 411 (1982).

[56] C. C. degli Atti *et al.*, Phys. Rev. C **39**, 259 (1989).

[57] *CEBAF Design Report*, CEBAF, Newport News, VA, 1986.

[58] C. W. Leemann, in *CEBAF 1992 Summer Workshop*, AIP (AIP, New York, NY, 1992), No. 269, p. 11.

[59] R. Legg, in *European Particle Accelerator Conference* (EPAC, Geneva, 1996).

[60] C. Yan, Technical Report No. CEBAF-R-93-001, CEBAF (unpublished).

[61] C. Yan *et al.*, *User's Manual of Hall C Target Raster System*, CEBAF, 1996.

[62] C. Yan *et al.*, Nucl. Instrum. Meth. **A365**, 261 (1995).

[63] W. Barry, Nucl. Instrum. Meth. **A301**, 407 (1991).

[64] K. B. Unser, in *1991 Accelerator Instrumentation Workshop*, AIP (AIP, New York, NY, 1992), No. 252, p. 266.

[65] K. B. Unser, Atomkernenergie-Kerntechnik **47**, 48 (1985).

[66] *Thermal Conductivity: Metallic Elements and Alloys*, Vol. 11 of *Thermophysical Properties of Matter*, edited by Y. S. Touloukian (Plenum, New York, NY, 1975).

[67] K. Gustafsson (unpublished).

[68] B. P. Terburg (unpublished).

[69] S. R. Lassiter *et al.*, IEEE Trans. on Appl. Superconductivity (1996).

[70] D. Dutta, *HMS Dipole Field Measurements* (unpublished).

[71] C. Yan *et al.*, Technical Report No. CEBAF-R-92-002, CEBAF (unpublished).

[72] *Conceptual Design Report Basic Experimental Equipment*, SURA/CEBAF, Newport News, VA, 1990.

[73] M. Berz, *COSY INFINITY Version 7 User's Guide and Reference Manual*, Michigan State University Cyclotron Laboratory, 1996.

[74] M. Berz, Nucl. Instrum. Meth. **A298**, 473 (1990).

[75] D. Abbott *et al.*, in *CEBAF 1992 Summer Workshop*, AIP (AIP, New York, NY, 1992), No. 269, p. 495.

[76] W. R. Leo, *Techniques for Nuclear and Particle Physics Experiments* (Springer-Verlag, New York, NY, 1992).

[77] P. J. Carlson, Nucl. Instrum. Meth. **158**, 403 (1979).

[78] G. Lenzen *et al.*, Nucl. Instrum. Meth. **A343**, 268 (1994).

[79] E. L. Garwin *et al.*, Nucl. Instrum. Meth. **107**, 365 (1973).

[80] A. O. Gasparian *et al.*, in *CEBAF 1992 Summer Workshop*, AIP (AIP, New York, NY, 1992), No. 269, p. 501.

[81] D. E. Groom, Eur. Phys. J. **C3**, 144 (1998).

[82] D. J. Abbott *et al.*, *The CODA System and its Performance in the First Online Experiments at CEBAF* (unpublished).

[83] *The CEBAF Trigger Supervisor User's Manual.*

[84] *CODA: CEBAF On-line Data Acquisition User's Manual, version 1.4*, 1995.

[85] D. Dutta, *The Hall C Matrix Element Optimization Package* (unpublished).

[86] D. Dutta, *Beam energy determination using kinematic methods* (unpublished).

[87] D. F. Geesaman, Tracking in the SOS Spectrometer.

[88] Y.-S. Tsai, Technical Report No. SLAC-PUB-848, SLAC (unpublished).

[89] L. W. Mo and Y. S. Tsai, Rev. Mod. Phys. **41**, 205 (1969).

[90] Y.-S. Tsai, Rev. Mod. Phys. **46**, 815 (1974).

[91] Y.-S. Tsai, Rev. Mod. Phys. **49**, 421 (1977).

[92] S. Stein *et al.*, Phys. Rev. D **12**, 1884 (1975).

[93] O. Benhar *et al.*, Phys. Rev. C **44**, 2328 (1991).

[94] P. Baran *et al.*, Phys. Rev. Lett. **61**, 400 (1988).

[95] Z. E. Meziani *et al.*, Phys. Rev. Lett. **69**, 41 (1992).

[96] C. C. degli Atti and G. B. West, Phys. Lett. B **458**, 447 (1999).

[97] L. L. Frankfurt *et al.*, Phys. Rev. C **48**, 2451 (1993).

[98] L. W. Whitlow *et al.*, Phys. Lett. B **250**, 193 (1990).

[99] B. W. Filippone *et al.*, Phys. Rev. C **45**, 1582 (1992).

[100] S. D. Drell and T. Yan, Phys. Rev. Lett. **24**, 181 (1970).

[101] G. B. West, Phys. Rev. Lett. **24**, 1206 (1970).

[102] B. M. Schwarzschild, Physics Today 20 (1980).

[103] in *Future Possibilities for Electron Accelerators*, University of Virginia (University of Virginia, Charlottesville, VA, 1979).

[104] B. M. Schwarzschild, Physics Today 19 (1982).

[105] I. Goodwin, Physics Today 57 (1983).

[106] I. Goodwin, Physics Today 55 (1984).

[107] I. Goodwin, Physics Today 59 (1984).

[108] C. D. Cothran, *Solid Target Heating* (unpublished).

[109] C. D. Cothran, *Solid Target Heating: Green's Function Solutions* (unpublished).